[AMERICAN JOURNAL OF SCIENCE, VOL. 300, APRIL, 2000, P. 289–343]

QUANTITATIVE ZN SPECIATION IN SMELTER-CONTAMINATED SOILS BY EXAFS SPECTROSCOPY

ALAIN MANCEAU, BRUNO LANSON, MICHEL L. SCHLEGEL, JEAN CLAUDE HARGÉ, MARTINE MUSSO, LAURENT EYBERT-BÉRARD, JEAN-LOUIS HAZEMANN, DANIEL CHATEIGNER*, and GÉRALDINE M. LAMBLE**

Environmental Geochemistry Group, LGIT-IRIGM, University Joseph Fourier and CNRS, BP 53, 38041 Grenoble cedex 9, France.

ABSTRACT. More than a century of non-ferrous metallurgical activities have had a severe impact on the natural environment leading, in most heavily contaminated sites, to a complete loss of the vegetation cover (that is, desert-like areas) or to the selection of metal-hyperaccumulator plant species. Identifying the chemical forms of toxic metals is of vital importance for a realistic assessment of the chemical risk posed by their presence in soils and selecting effective remediation technologies. In this study, X-ray diffraction (XRD), X-ray texture goniometry, and powder and polarized extended X-ray absorption fine structure (EXAFS, P-EXAFS) have been used to investigate quantitatively the speciation of Zn in soils contaminated by three smelters from northern France and Belgium, and coupled synchrotron-based micro-X-ray radiation fluorescence (μSXRF) and micro-EXAFS (μEXAFS) were also used for one of these soils. Of these techniques, the application of P-EXAFS and μEXAFS to molecular environmental science was unprecedented, and we show that their complementarity greatly improves the sensitivity of powder EXAFS to identify the nature of metal-containing minerals in soils. Franklinite ($ZnFe_2O_4$), willemite (Zn_2SiO_4), hemimorphite ($Zn_4Si_2O_7(OH)_2 \cdot H_2O$), and Zn-containing magnetite ($[Fe,Zn]Fe_2O_4$) were identified in dense soil fractions by XRD and powder EXAFS. These primary minerals originate from atmospheric fallout of Zn dusts emitted during the pyrometallurgical smelting process, and they act as the main source of Zn in contaminated soils. In all soil samples, Zn released in solution during the weathering of these high-temperature minerals is taken up partly by phyllosilicates and, to a lesser extent, by Mn and Fe (oxyhydr) oxides. Zn-containing phyllosilicates were identified by comparing powder EXAFS spectra to a library of model compounds and from the noteworthy angular dependence of EXAFS spectra collected on self-supporting films of clay soil fractions. Analysis of higher correlations in EXAFS spectra suggests that the local structure around Zn in phyllosilicates is trioctahedral. The phyllomanganate Zn-sorbed birnessite and Zn-containing Fe grains having a δFeOOH-like local structure were unambiguously identified by μSXRF–μEXAFS. In birnessite Zn is sorbed in the interlayer space above/below vacant sites and can be either 4-fold or 6-fold coordinated depending, presumably, on the anionic stacking of birnessite layers. Based on this micro-mineralogical investigation, a satisfactory fit of the three identified Zn species (that is, phyllosilicate, Mn, and Fe (oxyhydr)oxides) to experimental powder EXAFS spectra of all clay soil fractions was obtained. The significance, origin, and stability of Zn-phyllosilicates are discussed. Specifically, we show that the formation of Zn-containing phyllosilicates is consistent with calculated thermodynamic solubilities. For the range of measured Zn^{2+} (~10 ppm), $Si(OH)_4$ (10-20 ppm), and H^+ ($5.6 < pH < 7.5$) concentrations, soil solutions are supersaturated ($pH > 6$) or near saturation ($pH < 6$) with respect to the trioctahedral Zn phyllosilicate, Zn-kerolite. Finally, the plausibility of the formation of (Zn,Al) hydrotalcite-like species contemplated by Julliot (1999) is critically assessed.

* LPEC, Université du Maine-Le Mans, av. O. Messiaen, BP535 72085 Le Mans cedex, France.
** Advanced Light Source, Lawrence Berkeley National Laboratory, University of California, Berkeley, California 94720.

SYMBOLS

XRD = X-ray diffraction
EXAFS = extended X-ray absorption fine structure
P-EXAFS = polarized extended X-ray absorption fine structure
XANES = X-ray absorption near edge structure
SXRF = synchrotron-based X-ray radiation fluorescence
FWHM = full width at half maximum
d = density in g/cm^3
ϕ = size fraction of a soil sample
θ = Bragg angle in X-ray diffraction
ρ = tilt angle in texture goniometry
ρ_1 = ρ value for a pole density of 1 m.r.d.
m.r.d. = multiples of a random distribution. Unit used to express the texture (or pole density) normalized to powder at 1 m.r.d.
P_{max} = maximum orientation density of c* axes of clay particles in self-supporting films. Expressed in m.r.d.
P_{min} = minimum orientation density of c* axes of clay particles in self-supporting films. Expressed in m.r.d.
χ = EXAFS function
k = modulus of the wavevector in EXAFS spectroscopy
σ = Debye-Waller term in EXAFS spectroscopy. Account for the atomic disorder
S_0^2 = amplitude reduction factor in EXAFS spectroscopy. Account for multi-electronic processes
α = angle between the electric field vector of the synchrotron beam (ϵ) and the surface of the self-supporting film (that is the experimental angle)
β = angle between the vector connecting an atomic pair and the c* axis of a clay layer
S = sum of the fractions of individual EXAFS components
R_p = best-fit criterion used to adjust model and sample EXAFS spectra
K_{ZnKer} = solubility product of Zn-kerolite (ZnKer300)
MN1 to MN6 = samples from Mortagne du Nord (France)
E1 and E2 = samples from Evin-Malmaison (France)
M1 and M2 = samples from Maatheide (Belgium)
ZnKer300 = Zn-containing kerolite $Si_4Zn_3O_{10}(OH)_2 \cdot nH_2O$
ZnKer240 = Zn-containing kerolite $Si_4(Mg_{0.6}Zn_{2.4})O_{10}(OH)_2 \cdot nH_2O$
ZnKer190 = Zn-containing kerolite $Si_4(Mg_{1.1}Zn_{1.9})O_{10}(OH)_2 \cdot nH_2O$
ZnKer88 = Zn-containing kerolite $Si_4(Mg_{2.12}Zn_{0.88})O_{10}(OH)_2 \cdot nH_2O$
ZnKer75 = Zn-containing kerolite $Si_4(Mg_{2.25}Zn_{0.75})O_{10}(OH)_2 \cdot nH_2O$
ZnKer73 = Zn-containing kerolite $Si_4(Mg_{2.27}Zn_{0.73})O_{10}(OH)_2 \cdot nH_2O$
ZnKer60 = Zn-containing kerolite $Si_4(Mg_{2.4}Zn_{0.6})O_{10}(OH)_2 \cdot nH_2O$
ZnKer3 = Zn-containing kerolite $Si_4(Mg_{2.97}Zn_{0.03})O_{10}(OH)_2 \cdot nH_2O$
ZnFh22 = Zn-sorbed ferrihydrite, 22 percent surface coverage
ZnFh17 = Zn-sorbed ferrihydrite, 17 percent surface coverage
ZnFh8 = Zn-sorbed ferrihydrite, 8 percent surface coverage
ZnGt60 = Zn-sorbed goethite, 60 percent surface coverage
ZnGt30 = Zn-sorbed goethite, 30 percent surface coverage
ZnGt = Zn-substituted goethite $\alpha(Fe_{0.97}Zn_{0.03})OOH$.
ZnBi1 = Zn-sorbed birnessite, Zn/Mn = 0.008
ZnBi2 = Zn-sorbed birnessite, Zn/Mn = 0.069
ZnBi3 = Zn-sorbed birnessite, Zn/Mn = 0.126
ZnHec = Zn-sorbed hectorite

INTRODUCTION

In any industrial region of all continents, soils are polluted, especially with trace elements (Salomons, Förstner, and Mader, 1995). Due to the early industrialization of European countries in the end of the XIXth century, soils of Europe have been exposed to great amounts of metallic pollution. Several hundred sites severely contaminated by metals have been identified in France in a recent survey by the French Ministry of Environment (1996), and non-ferrous zinc and lead smelters count among the most polluting mineral processing industries. More than 80 percent of the current primary zinc production capacity in the world is now based on the less polluting Roast-Leach-Electrowinning (RLE) process (Wickham, 1990), which is a wet chemical or hydrometallurgical process. This process replaced the former pyrometallurgical Imperial Smelting Process (ISP), which is known to produce considerable amounts of dusts and fumes rich in zinc and lead. A realistic evaluation of the potential health risks posed by contaminated soils and food relies on the accurate determination of the speciation of the heavy metals, whose toxicity and mobility depend, not only on concentration, but also critically on chemical form(s).

The term speciation refers to the electronic structure (oxidation state, nature of chemical bonds) and binding forms of an element at the molecular-level. Four major binding mechanisms can be distinguished for metal accumulation: (1) precipitation of discrete metal compounds (for example, metal salt or oxide), (2) complexation with organic matter, (3) adsorptive bonding on fine grained particles (for example on oxides, silicates . . .), and (4) incorporation in soil minerals through coprecipitation or lattice diffusion (McBride, 1994). Due to the large possible number of heavy metal species in soils, identifying at least the major species is already a challenging task. Techniques used to this end can be categorized in two groups: selective extraction methods and physical techniques. Extraction methods were developed with the assumption that it is possible to fractionate the different pools of heavy metals by using multiple extraction steps with chemical reagents of various strengths, reaction times, temperature, and pH conditions. Extensive extraction methods have appeared in the literature (Tessier, Campbell, and Bisson, 1979; Pickering, 1981; Lake, Kirk, and Lester, 1984; Förstner, 1993; Davidson and others, 1994; Quevauviller and others, 1994; Krishnamurti and others, 1995; McGrath, 1996; to name a few) and were critically reviewed (Bermond, 1992; Whalley and Grant, 1994; Das and others, 1995; Raksasataya, Langdon, and Kim, 1996; Sheppard and Stephenson, 1997; to name a few). In chemical extractions, species are operationally grouped into five fractions: exchangeable, carbonate, Fe-Mn oxide, organic, and residual fractions. Various criticisms have been leveled at sequential methods because these operationally-defined species do not necessarily reflect the exact nature of the heavy metal-containing entities. Errors essentially arise from the lack of extractant selectivity (that is, inaccuracy in releasing metal from specific geochemical phases), metal readsorption processes, the extractant volume to sample mass ratio, and sample handling. The inability to validate the procedure itself also appears to be a major drawback of sequential extraction techniques. Despite these problems, Tessier and Campbell (1991) argued that sequential extraction provides a pragmatic approach for discerning heavy metal speciation in contaminated soils and sediments.

Another approach for the determination of heavy metal species and their quantitative distribution among soil components involves the use of X-ray based physical techniques such as X-ray diffraction, fluorescence, and absorption spectroscopy. Among these, EXAFS (extended X-ray absorption fine structure) spectroscopy has been used to some extent to identify heavy metal species in soils (Cotter-Howells and others, 1994; Manceau and others, 1996; Föster and others, 1997; Kemner and others, 1997; O'Day, Carroll, and Waychunas, 1998; Kim, Rytuba, and Brown, 1999; Morin and others, 1999; Ostergren and others, 1999). This structural technique has the necessary elemental

specificity, short-range order sensitivity, and unrivalled detection limit, presently equal to ~100 mg kg^{-1} for most heavy metals on third generation synchrotron radiation sources such as the European synchrotron radiation facility (ESRF) at Grenoble, to interrogate directly elemental occurrences in soils. However, EXAFS has a low sensitivity (1) to minor species, and (2) to metal-containing phyllosilicates. These limitations are serious drawbacks to identify the nature of secondary Zn-bearing phases, which form during the leaching of heavy metals from contaminant minerals. In this study, these two significant obstacles were circumvented for the first time: (1) by coupling bulk EXAFS to in-situ synchrotron-based micro-X-ray radiation fluorescence (μSXRF) and μEXAFS measurements, and (2) by polarized EXAFS (P-EXAFS).

1. The EXAFS signal is a weighted average from the contributions of all metal species present in the sample. Manceau and others (1996) showed that major species could be individually retrieved from a linear least-squares fitting procedure to known mixtures of Zn model compounds. This simple and rapid approach is generally preferable to the traditional multi-shell EXAFS fitting technique, which is inadequate for investigating multiphase systems because it rapidly results in misjudging the number of fitting structural parameters. However, there are several limitations to identifying metal species by spectral combinations. First, the unknown sample can be identified only as a composite of spectra in the database. Thus, we are limited to components present in the database, and this requires the generation of large spectral libraries of model compounds against which EXAFS spectra of natural soil samples can be compared. Second, only major phases are detected easily. The detection limit for minor species is indefinite, as it depends on the quality of EXAFS spectra and on the structure and chemical composition of all species present in the sample. Third, there is the usual risk of allowing too many EXAFS components in the spectral fit. The information content of EXAFS data being band-width limited, linear decompositions with more than 4 individual components is generally not justified, especially when minor components are below the stated detection limit (as in Kim, Rytuba, and Brown, 1999). Fourth, metal species containing high X-ray scatterers (that is, high Z elements) and present in substantial amount are preferentially detected over low density species. This situation can be met in soils whenever a metal is bound to minerals and organics (Morin and others, 1999). For instance, let us consider a phase mixture (P) consisting of 80 percent ZnO + 20 percent Zn acetate dihydrate, and let us assume a 6 percent error in the determination of the amount of ZnO during the linear combination. The residual EXAFS signal not fitted by the ZnO model equals R = P-(0.85 × ZnO) and, consequently, the EXAFS spectrum of the unknown second species equals U = R/0.15. Figure 1 clearly shows that this U spectrum is much different from Zn acetate dihydrate. Thus, a 6 percent error in the quantification of ZnO suffices to mask the presence of 20 percent of a low X-ray scattering organic species.

The most promising way to distinguish individual species in heterogeneous systems is to use spatially resolved structural techniques such as μXAFS (X-ray absorption fine structure) coupled to μSXRF. In situ determinations of the oxidation state of metal species in natural systems were obtained recently by μXANES (X-ray absorption near edge structure) (Bajt, Sutton, and Delaney, 1994; Bertsch and others, 1994; Hunter and others, 1997; Tokunaga and others, 1997; Acron, Mirtic, and Kodre, 1998; Dyar and others, 1998; Nakai and others, 1998; Yun and others, 1998; Duff and others, 1999a; Kemner and others, 1999). With the advent of third generation light sources, the brightest spectrometers now have the potential to measure with good statistics the extended energy region (EXAFS) located beyond main absorption edges (XANES) of X-ray absorption spectra, which is generally necessary to get meaningful structural information on multiphase systems (MacDowell and others, 1997; MacDowell and others, 1998; Duff and others, 1999b; Held and others, 1999; Newville and others, 1999). In this study we have obtained the first in-situ measurement of the speciation of a metal

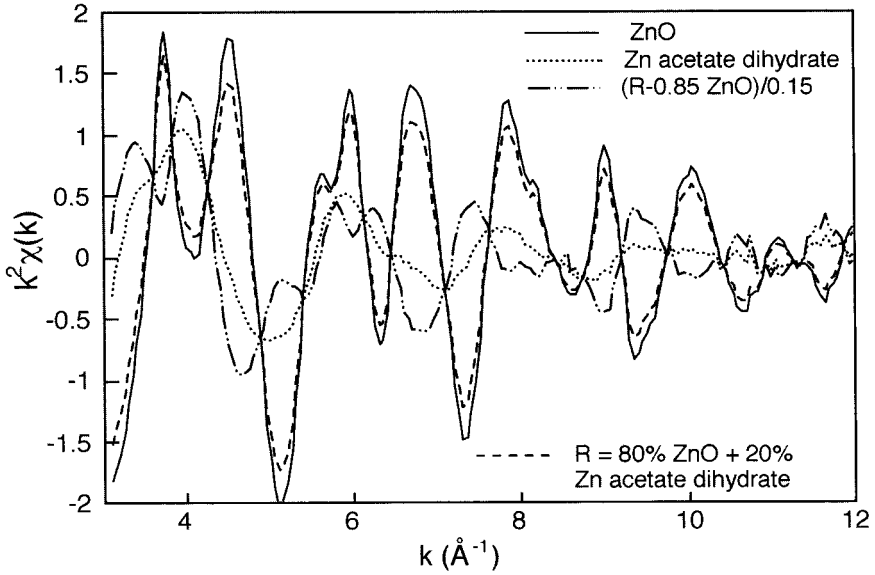

Fig. 1. Zn K-edge EXAFS of ZnO, Zn acetate dihydrate, a hypothetical compound R consisting of 80 percent Zn O + 20 percent Zn acetate dihydrate, and the difference spectrum (R-0.85 ZnO)/0.15.

(Zn) at the micron-scale in unperturbed soil materials. Fe (oxyhydr)oxides- and Mn oxides-bound Zn minor species were directly identified by this technique, thereby justifying their incorporation in linear spectral decompositions of bulk EXAFS spectra to reference compounds.

2. Phyllosilicates, such as smectites, are major constituents of soils and sediments. They have unique physico-chemical properties, including high cation exchange capacity (up to ~1 meq g^{-1}), elevated specific surface area (up to ~700 m^2 g^{-1}), and swelling behavior, which make them extremely reactive toward sorption processes and, therefore, good sinks for trace elements. Owing to the typically sub-micron size of phyllosilicates, metal-containing phyllosilicates can be enriched by size fractionation, thereby facilitating their identification. This task remains however particularly difficult because the "clay fraction" of soils, defined operationally as the <2 μm fraction, still contains a high proportion of physically mixed, and surface-coated, ancillary minerals such as Fe and Mn oxides. Phyllosilicates from soils are essentially aluminosilicates, so that the EXAFS signal scattered by their constituent "light" elements (Si, Al, Mg) can be largely hidden by the intense scattering of Fe and Mn atoms in Zn-containing (Fe,Mn)-oxides. In an effort to improve the sensitivity of EXAFS to the detection of metal-bearing phyllosilicates in soils, polarized EXAFS measurements on self-supporting clay films were undertaken, following the recent application of this method to reference fine-grained layered minerals (Manceau, Schlegel, and others, 1999). In an oriented sample, the signal from a given atom is largest when its radius vector lies along the direction of the X-ray polarization vector (Lee and Pendry, 1975; Heald and Stern, 1977; Stern and Heald, 1983). It follows that P-EXAFS measurements provide orientation dependent structural information, and can be typically used to probe the local structure of layer silicates between two different directional limits, parallel and perpendicular to the (001) basal plane, by varying the angle between the electric field vector and the surface of a self-supporting clay film. Apart from its utilization for site determinations in classical single crystal studies and occasional use in anisotropic materials problems, P-EXAFS was

first employed to study the crystal structure of fine-grained phyllosilicates by Manceau and others (1998; Manceau, Schlegel, and others 1999) and recently extended to examine phyllosilicate surface reactivity (Schlegel and others, 1999). These were simple clay systems but we show here that the complement of this technique, with texture goniometry, and the preparation of highly oriented films from the clay fraction of soil materials provide a direct means for assessing the presence of metal-phyllosilicates in natural systems.

In this study, the speciation of Zn in soils of three severely smelter-impacted areas from northern France and Belgium has been investigated quantitatively. The characteristics of the three sites will be described first. Following the experimental section, the forms of zinc in each sites will be examined successively. The main conclusion is that Zn, released during the weathering of primary minerals issued from the smelting process, is taken up predominantly by phyllosilicates and, to a lesser extent, by Mn and Fe (oxyhydr)oxides. In the last section, the crystal chemical nature and thermodynamic stability of neoformed Zn-containing phyllosilicates are discussed. Finally, based on these structural and thermodynamical results, the plausibility of the formation of (Zn,Al) hydrotalcite-like species reported by Julliot (1999) will be evaluated, and his interpretation of EXAFS spectra reassessed.

SITE DESCRIPTION

The first site is located in the southern outskirts of the town Mortagne du Nord (Nord-Pas de Calais, France) and corresponds to an ancient ISP-based Zn and Pb refining complex (fig. 2A). The Zn-smelter was in operation from 1906 until 1963, while the Pb unit operated from 1923 to 1928 (Cambier, 1998). In the pyrometallurgical process, the roasting of ZnS and PbS ores yields a gas phase which contains SO_2 at a concentration suitable as a feedstock for H_2SO_4 production. For this purpose a sulfuric acid plant was used from 1923 to 1968 to convert the roast off-gases from the Zn plant. The Zn-smelter was the third largest smelter in the world during the first half of the XXth century and has emitted considerable amounts of Zn into the atmosphere. The emission of gaseous and dusty metals caused their accumulation in neighboring soils. In a grassland, situated several hundreds meters away from the emission center, a 5 to 8 cm thick layer of dust containing ~1 to 2 wt percent Zn and ~1 wt percent Pb can still be observed after digging out the superficial layer of inert material used to bury harmful slag materials (fig. 2B). Figure 2B shows that Zn and Pb are, however, taken up by roots of the two metal-tolerant plant cultivars, Cardaminopsis halleri and Armeria Maritima halleri. Given the importance of this pollution a field laboratory has been set up by the French Ministry of Environment to study the form and fate of heavy metals (Zn, Pb, As, Cd) on and off the former plant site so as to design effective remediation strategies.

The second site is located in the vicinity of the Pb-Zn smelter near the urbanized area of Evin-Malmaison and Noyelles-Gaudault, about 4 km from the Zn smelter of Auby (Nord-Pas de Calais, France). The first plant still uses a pyrometallurgical process, but regulatory standards were met by installing off-gas filters in 1970, which led to a reduction of dust emission from several tons day^{-1} to ~300 kg day^{-1} (~30 kg day^{-1} Pb and ~3 kg day^{-1} Zn) (Sarcia and Talbot, 1984; Sobanska, 1999; Sobanska and others, 1999). Zn and Pb levels currently exceed several hundred mg/kg in a 40 km^2 area and reach several thousand mg/kg a few hundreds meters from the smelter in the plowed layer (0-25 cm) of agricultural fields used for livestock breeding activities (Sarcia and Talbot, 1984; Godin, Feinberg, and Ducauze, 1985; Sobanska, 1999; Charlatchka and Cambier, 1999). The present pollution is essentially inherited from past activities when emission controls were completely lacking, but maximum blood lead concentration in children still reach levels encountered in inner cities of many countries. A recent survey in 1996 to 1997 by A. Leroyer and others (personal communication) showed that 6.5

A.

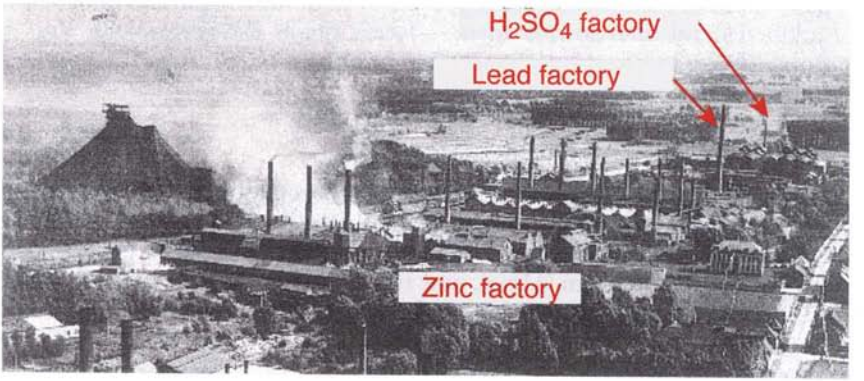

B.

Fig. 2(A) Aerial view of the industrial complex of Mortagne du Nord in 1950 showing the Zn- and Pb-smelters and the sulfuric acid plant. Note the Zn,Pb waste material tailing left over from mineral processing operation on the left and the important emission of fumes (containing heavy metal vapors) and dusts from chimneys (After Thiry and Van Oort, 1999). (B) Field photograph of the slag horizon (dark layer, sample MN1), which can be observed today in grassland and wooded soils nearby the former plant. This polluted layer has been buried by inert material, but Zn and Pb are taken up to the surface by roots of metal-tolerant plant cultivars. The white flower is Cardaminopsis halleri.

percent (13 individuals among 200) of examined children aged 8 to 11 yr living in the polluted area had a blood lead level exceeding 100 µg l^{-1} as compared to 1.0 percent (2 individuals among 200) in the reference population. The lead level in the former subsample ranged from 1.6 to 165 µg l^{-1}. Adverse effects of lead on the intellectual performances and behavior of children are well known (Liebau, 1985; Needleman and Gatsonis, 1990; Fergusson, 1990; Ernhart, 1992), but large uncertainties persist on the harmful level because there is apparently no threshold. Dietrich and others (1993) estimated that lifetime blood lead concentrations above 200 µg l^{-1} were associated with IQ deficits on the order of 7 points when compared to children with mean concentrations less than or equal to 100 µg l^{-1}. In the area studied, the impact of Pb pollution on the young population seems relatively limited.

The third site is located near the city of Maatheide in northeastern Belgium. A Zn smelter using a pyrometallurgical process operated from 1904 to 1974 and had a severe impact on the local environment. The total Zn content in the surrounding acid sandy soil gradually decreases away from the former plant from about 20 to 2 g kg^{-1} at 500 m distance. Due to the very high concentration of different non-ferrous metals in the soil,

the vegetation cover disappeared completely over 135 ha. In 1990, 3 ha of this "desert-like" area were successfully revegetized by immobilizing in situ toxic metals with mineral additives and then sowing metal tolerant plants (Vangronsveld, Van Assche, and Clijsters, 1995).

EXPERIMENTAL

Sample Description

The first soil near Mortagne du Nord is located on the border of the grassland (fig. 2B) at ~200 m northeast from the former plant. Samples were collected in the dark silt level of the topsoil (MN1) and from four different depths below MN1: 8 to 12 cm (MN2), 40 to 50 cm (MN3), 60 to 70 cm (MN4), and 100 to 110 cm (MN5) (table 1). All samples were air-dried and then sieved at 2 mm and 100 μm. The dense fraction ($d > 2.9$) was separated from the silt fraction ($\phi < 100$ μm) by settling in Na polytungstate ($Na_6(H_2W_{12}O_{40})H_2O$) solution. Then the clay fraction was separated by sedimenting the residual silt and $d < 2.9$ fraction. The proportion of Zn in the clay and silt fractions was calculated from elemental analyses and from the percentage of each fraction as obtained

TABLE 1

General description and mineralogy of soil samples

Locality	Sample	Depth (cm)	Description	Fraction studied by EXAFS	Mineralogy (XRD)
Mortagne de Nord, France	MN1	~20*	Slag layer	$d > 2.9$, $\phi < 100$ μm	Quartz, albite, microcline, willemite, franklinite, magnesio-ferrite, magnesio-riebeckite, illite-smectite mixed layer, illite, kaolinite, pyrite.†
	MN2	8–12$	Sandy horizon	$\phi < 2$ μm	Quartz, albite, microcline, rutile,§ anatase,§ zircon,§ clinozoisite,§ vesuvianite,§ illite-smectite mixed layer, illite, kaolinite, chlorite,† willemite,§·† franklinite.§·†
	MN3	40–50$	Sandy horizon	$\phi < 2$ μm	Quartz, albite, microcline, rutile,§ anatase,§ zircon,§ clinozoisite,§ vesuvianite,§ illite-smectite mixed layer, illite, kaolinite, willemite,§·† franklinite.§·†
	MN4	60–70$	Sandy horizon	$\phi < 2$ μm	Quartz, albite, microcline, illite-smectite mixed layer, illite, kaolinite
	MN5	100–110$	Sandy horizon	$\phi < 2$ μm	Quartz, albite, microcline, illite-smectite mixed layer, illite, kaolinite
	MN6	0–30	Agricultural soil, tilled horizon	$\phi < 100$ μm, $\phi < 2$ μm, $\phi < 0.1$ μm	Quartz, albite, microcline, illite-smectite mixed layer, illite, kaolinite, chlorite
Evin-Malmaison, France	E1	0–30	Agricultural soil, tilled horizon	<50 μm	
	E2	0–30	Agricultural soil, tilled horizon	<2 μm	
Maatheide, Belgium	M1	0–20	Sandy soil	<2 mm	
	M2	0–20	Sandy soil	<40 μm	

* Below the ground.
$ Below MN1.
§ Detected only in the dense fraction ($d > 2.9$).
† Trace amounts.

by laser particle-size analysis. The second sampling site near Mortagne du Nord (sample MN6) corresponds to the tilled horizon of an agricultural field at 1 km east-northeast from the former plant. The <100, <2, and <0.1 μm fractions were obtained by sieving (<100 μm), sedimentation ($\phi < 2$ μm), and ultracentrifugation ($\phi < 0.1$ μm). Samples El ($\phi < 50$ μm) and E2 ($\phi < 2$ μm) come from the tilled horizon of an agricultural soil at Evin-Malmaison located 1 km from the Pb-Zn smelter. The soil has a clay-silty texture and can be classified as a Luvisol (Mench and others, 1994; Charlatchka and Cambier, 1999). The speciation of Pb in E2 was studied previously (Manceau and others, 1996). Sample M was collected in the 0 to 20 cm layer a few hundreds meters north from the former smelter of Maatheide.

Methods

Coarse ($\phi < 2$ mm), silt ($\phi < 100$ μm), and clay ($\phi < 2$ μm) fractions were calcined at 450°C, then digested in concentrated $HF/HClO_4$, and diluted in HCl solution to a suitable concentration for chemical analysis. Zn, Fe, and Mn were determined by inductively coupled plasma atomic emission spectroscopy (ICP-AES), and Pb was determined by atomic absorption spectroscopy. Mineralogical analyses were performed by XRD using a Siemens D5000 powder diffractometer equipped with a Kevex Si(Li) solid state detector and Cu Kα radiation (40 kV, 40 mA). Intensities were measured over the 3° to 80° 2θ Cu Kα (29-1.2 Å) Bragg angle at a 0.04° 2θ interval using a 4 s counting time per step. Ca-exchanged clay fractions were prepared as oriented slides and recorded in the air-dried and ethylene-glycol saturated states from 3° to 35° 2θ Cu Kα (29-2.55 Å) at a 0.02° 2θ interval using a 4 s counting time per step. Self-supporting films for P-EXAFS measurements were prepared from Na saturated (1M $NaNO_3$) clay fractions. The orientation distribution of the basal planes of illite-smectite and kaolinite platelets within self-supporting films for MN3, MN6, and E2 were determined by quantitative texture analysis (goniometry) by using a curved position sensitive (INEL CPS 120) detector, which allows acquisition of the whole diffraction pattern over $\Delta 2\theta = 120°$ for every tilt (ρ) angle of the sample. The angle ρ describes the tilt of the film plane with respect to the X-ray incident plane. A monochromatized 1 mm^2 beam (Cu Kα) was collimated on the flat sample in the asymmetric reflection mode (7×7 mrad of divergence). The (001) pole figures of illite-smectite and kaolinite were measured using $\Delta\rho = 5°$ increments for angular ranges of $0 \leq \rho \leq 85°$ (counting time: 1800 s per step). Because self-supporting clay films have a [001]* fiber texture, the distribution of lattice normals can be simply obtained from the 2θ numerical integration of $I(\rho,\theta)$ over the θ angle of the diffracted peak with background subtraction (ρ scan). The procedure to normalize integrated net intensities into distribution densities has been detailed elsewhere (Manceau, Lanson and others, 2000).

Powder and polarized EXAFS spectra were collected at ambient temperature on line BM32 at ESRF in Grenoble, France. A multi-element Ge solid-state detector was used to record Zn K-edge fluorescence-yield EXAFS spectra. Counting times were adjusted to obtain at least 10^6 good counts per energy step at energies above the Zn K edge. Powder EXAFS spectra were recorded at the magic angle to get rid of the possible preferential orientation of clay platelets in powdered samples (Manceau and others, 1990). Polarized measurements were performed by mounting the film samples onto an x,y-goniometer sample positioner. In-plane and out-of-plane P-EXAFS spectra were measured successively by orienting the plane of the self-supporting film respectively parallel or perpendicular (grazing incidence) to the electric field vector (Manceau, Schlegel, and others, 1999).

μSRXF maps and μEXAFS spectra were measured on the 10.3.2. station at the Advanced Light Source (ALS) (MacDowell and others, 1997; Padmore and others, 1997). For μSRXF maps, 30 μm-thick soil thin sections embedded in epoxy were rastered in 3 to 6 μm steps through the 2 μm sized focused monochromatic X-ray beam. The

selected Kα fluorescence was integrated typically for 1 sec per point corresponding to a total data collection time of approx 8 h. A typical energy dispersive X-ray (EDX) fluorescence spectrum integrated during a map measurement is shown in figure 3. The total signal is greatly dominated by the Fe ($\sim 4\ 10^6$ counts) and Mn ($\sim 8\ 10^6$ counts) fluorescence-yield of the soil matrix, the Zn signal making only $\sim 3\ 10^5$ counts. In EXAFS spectroscopy typically 10^6 good counts are desired to get an acceptable precision of 10^{-3} on the measurement of the absorption coefficient. In spite of this limitation, due to the present flux limitation on this station ($\sim 10^8$ ph s^{-1} μm^{-2}), Zn-EXAFS spectra with an acceptable signal/noise ratio were successfully obtained by averaging 8 to 10 spectral sweeps of ~ 1 hr each thanks to the high stability of the X-ray source and spectrometer optics. EXAFS spectra ($\chi(k)$) were derived from raw absorption spectra by modeling the post-edge atomic absorption background with a two-range spline and normalizing the amplitude to the absorption jump ($\Delta\mu$). The kinetic energy (E_k) of the photoelectron was converted to wavevector (k) values by systematically taking the origin ($E_k = 0$) at $\Delta\mu/2$. Radial structure functions (RSFs) were obtained by Fourier transforming k-weighted $\chi(k)$ spectra using a Kaiser window (Manceau and Combes, 1988).

The speciation of Zn was determined by linear combination of known compounds in a least-squares fitting of unknown EXAFS spectra (Manceau and others, 1996; Kim, Rytuba, and Brown, 1999; Morin and others, 1999; Ostergren and others, 1999). The residual R_p, where $R_p = \Sigma(k^3\chi_{exp} - k^3\chi_{model})^2$, was used as the "best-fit" criterion, a lower R_p representing a better match between the fitted model spectra and the sample spectrum. The fractional contribution of each reference spectrum to the fit is directly proportional to the percentage of Zn present in that form in the soil material. In case of multiple species, the precision on individual contributions is difficult to evaluate precisely because it depends on many factors. These are the signal/noise ratio of EXAFS spectra, the width of the fitting k-range, the presence in the database of all unknown species which significantly contribute to the total EXAFS signal, the structural similarity between known and unknown compounds, and the mixing of organic and inorganic species because organic compounds generally yield a weak EXAFS signal which can be

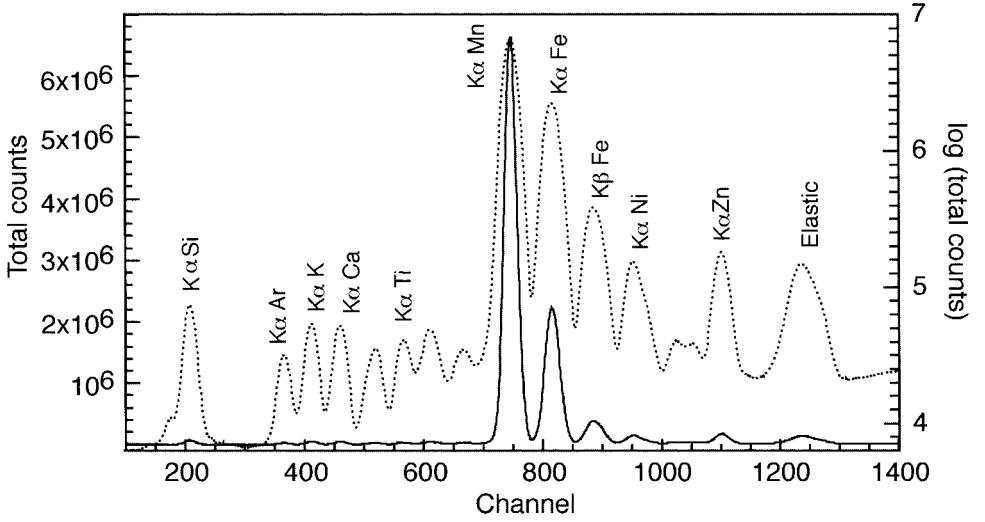

Fig. 3. Energy dispersive X-ray (EDX) spectrum recorded at 10 keV and integrated during the 8 h of acquisition time of elemental maps presented in figure 18B. The total signal is heavily dominated by the Fe and Mn fluorescence-yield of the soil matrix, the Zn signal making only $\sim 2\ 10^5$ counts.

masked by the more intense signal from inorganic compounds. In the present study, Zn is uniquely in mineral forms so that the detection limit of minor species and the precision of individual components is believed to be ~10 to 15 percent. Individual components should ideally sum to S = 100 ± 15 percent, but sometimes good fits are obtained with S values as low as 60 to 70 percent. The difference from 100 percent can be overlooked by scaling the sum of components to 100 percent (Kim, Rytuba, and Brown, 1999), but this arbitrary normalization is physically incorrect when this difference is higher than the stated precision, and its structural origin should be sought. The two most likely explanations are a difference of local order or coordinative environment in unknown and known compounds, and the omission or misidentification of a metal species in the least-squares fitting of $k^3\chi$ functions.

Model Compounds

A large database of pure Zn minerals was generated to compare model compounds against soil samples. In addition various Zn-substituted and Zn-sorbed references relevant to soil minerals were synthesized (fig. 4). All sorption experiments were conducted in a saturated atmosphere of argon gas, at a constant temperature of 25 ± 0.1°C, and, unless explicitly stated, in a 0.1 mol l^{-1} $NaNO_3$ electrolyte background. A series of Zn-containing kerolites (ZnKer) of formulae $(Si_4(Mg_{3-x}Zn_x)O_{10}(OH)_2 \cdot nH_2O)$ with x comprised between 0.03 and 3.0 was synthesized according to the procedure described by Decarreau (1985). Zn-sorbed hectorite was prepared by addition of a $Zn(NO_3)_2$ aliquot (40 µM g^{-1}) to a suspension of hectorite ($Na_{0.35}Mg_{2.65}Li_{0.35}Si_4O_{10}(OH)_2$) at high ionic strength (0.3 mol l^{-1} $NaNO_3$) to prevent Zn sorption on clay exchange sites and focus Zn sorption onto edge sites. After 5 days of sorption reaction at a constant pH of 6.5, Zn-sorbed hectorite was filtered, washed with a few milliliters of bidistilled water, and a self-supporting film was prepared. This protocol is the same as that described in details by Schlegel and others (1999) for the preparation of Co-sorbed hectorite. Three Zn-sorbed birnessites with Zn/Mn molar ratio of 0.008 (ZnBi1) 0.069 (ZnBi2), and 0.126 (ZnBi3) were prepared by addition of a $Zn(NO_3)_2$ solution to a hexagonal birnessite suspension pre-equilibrated at pH 4 (Silvester, Manceau, and Drits, 1997). ZnBi1 and ZnBi3 were prepared as powder, and ZnBi2 as a self-supporting film. An $\alpha(Fe_{0.97}Zn_{0.03})OOH$ goethite (ZnGt) was synthesized by aging for 2 months at 70°C and pH 13.5 a freshly precipitated Zn-doped ferrihydrite. At the end of the aging time, the doped goethite was washed with oxalate to remove remaining amorphous Fe coatings (Cornell and Schwertmann, 1996), filtered, rinsed, and dried. Zn was also sorbed on goethite at surface site coverage of 30 percent (ZnGt30) and 60 percent (ZnGt60), and on ferrihydrite at surface site coverage of 8 percent (pH 7.3, ZnFh8), 17 percent (pH 6, ZnFh17), and 22 percent (pH 7.3, ZnFh22). Suspensions containing the ferric solid phases were spiked at pH 4 with the desired amount of $Zn(NO_3)_2$ and then slowly titrated up to pH 7 (ZnGt) or 6.0 to 7.3 (ZnFh). Zn-sorbed goethite and ferrihydrite samples were then allowed to age at the target pH for 1h, filtered, and air-dried. In all sorption experiments, solute Zn remained always undersaturated with respect to known oxides and hydroxides precipitates (Baes and Mesmer, 1976).

RESULTS

Speciation of Zn in the soils from Mortagne du Nord

Chemical and mineralogical characterization.–Results from chemical analyses indicate that Zn, Pb, Fe, and Mn are more concentrated in the <2 µm than in the <100 µm and <2 mm fractions at all depths in the soil profile (table 2). The weight Pb concentration in the <100 µm fraction decreases from MN1 to MN5 by a factor of ~350 (4.596 g kg^{-1} versus 13 mg kg^{-1}) while the Zn concentration decreases by a factor of only ~40 (15.01 g kg^{-1} versus 353 mg kg^{-1}) (fig. 5A). Therefore, the regional geochemical background for

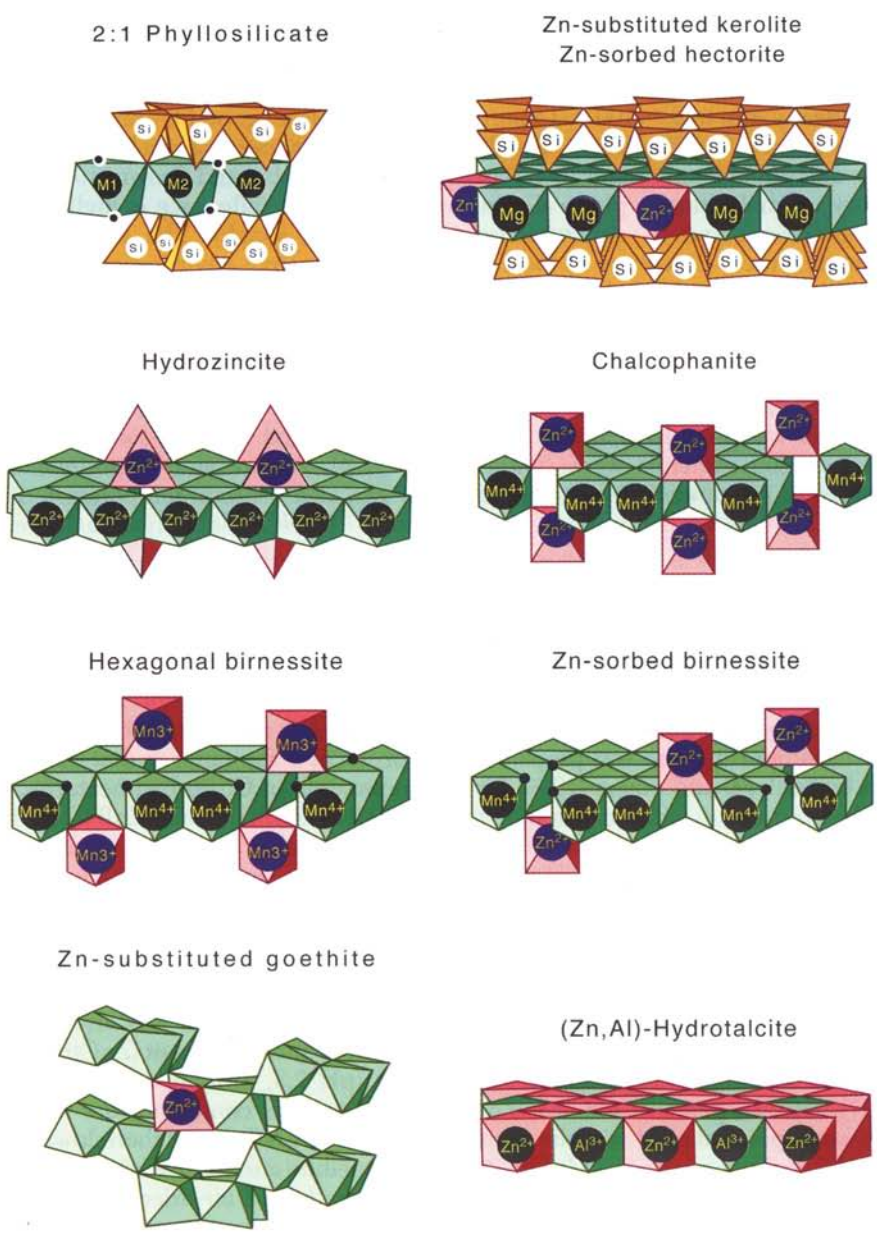

Fig. 4. Idealized structures for 2:1 phyllosilicate, Zn-substituted kerolite ($Si_4(Mg_{3-x}Zn_x)O_{10}(OH)_2 \cdot nH_2O$), Zn-sorbed hectorite ($Na_{0.35}Mg_{2.65}Li_{0.35}Si_4O_{10}(OH)_2$), hydrozincite ($Zn_5(OH)_6(CO_3)_2$), chalcophanite ($ZnMn_3O_7 \cdot 3H_2O$), hexagonal birnessite, Zn-sorbed hexagonal birnessite at high surface coverage (ZnBi2 and ZnBi3), Zn-substituted goethite ($\alpha FeOOH$), and (Zn,Al)-hydrotalcite ($Zn_3Al(OH)_8(CO_3)_{0.5}$). M1 denotes trans OH sites, M2, cis OH sites. Exchangeable cations are not represented. After Silvester and others (1997), Wadsley (1955), Post and Appleman (1988), Ghose (1964), and Brindley and Brown (1980).

Pb (10-20 mg/kg) is almost reached at 40 cm depth (MN3), whereas the Zn background level is still ~10 times exceeded (20-50 mg kg^{-1}; Baize, 1997; Cambier, 1998) at 100 cm depth (MN5). Since the Pb plant shut down before the Zn plant (1928 versus 1963), this remarkable difference of profile concentration between Zn and Pb reflects the well-

known contrast of their mobilities in the environment. Figure 5B shows that the weight fraction of <2 μm particles remains almost constant with depth, whereas the weight fraction of Zn in this clay fraction progressively increases, from 8 percent in the top 10 cm to 72 percent at 60 to 70 cm depth. Thus Zn is almost exclusively concentrated in the

TABLE 2

Chemical analyses of soil samples from Mortagne du Nord (mg kg^{-1}).

	MN1			MN2			MN3			MN4			MN5		
	<2mm	<100μm	<2μm	<2mm	<100μm	<2μm	<2mm	<100μm	<2μm	<2mm	<100μm	<2μm	<2mm	<100μm	<2μm
Zn	19500	15010	26400	nd	1405	3140	338	453	1321	nd	442	2511	331	353	nd
Pb	8876	4596	17770	nd	73	485	27	17	117	nd	15	171	15	13	nd
Fe	31700	28600	51600	nd	12000	47300	11600	16100	68500	nd	20400	72400	19400	23900	nd
Mn	1683	991	2156	nd	403	1323	347	517	2093	nd	307	1040	151	217	nd

nd: not determined.

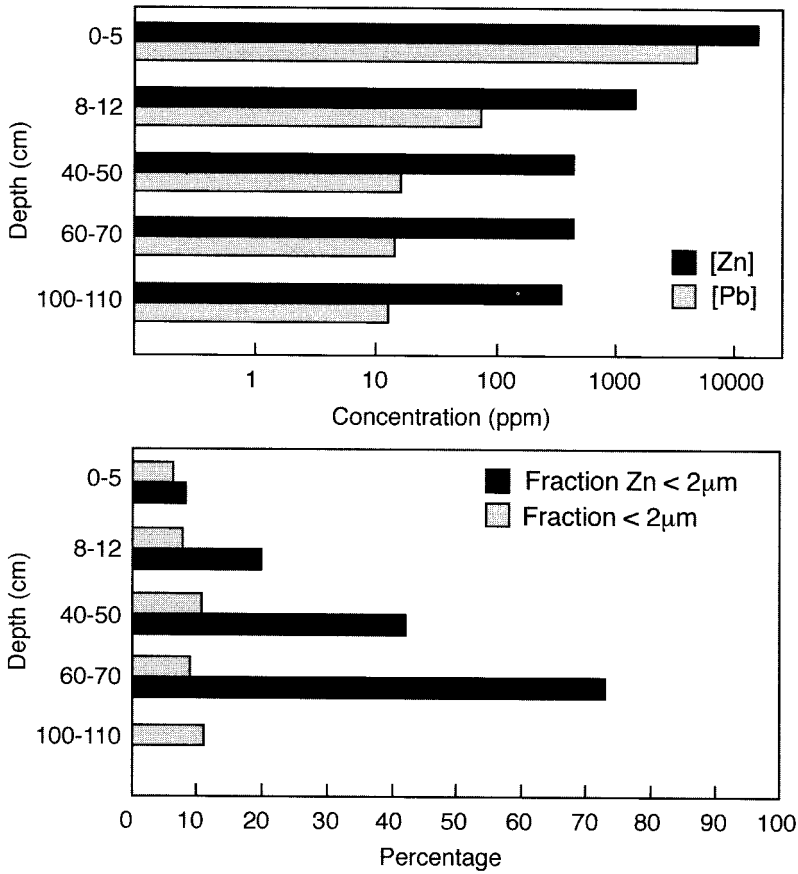

Fig. 5(A) Profile concentration of Zn and Pb in the silt fraction (<100 μm) of the soil from Mortagne du Nord (samples MN1-MN5). (B) Relative distribution of Zn in the clay fraction (<2 μm) and percentage of the clay fraction in the <2 mm soil fraction. Zn is increasingly concentrated in the clay fraction with depth.

finest fraction in deep horizons, and the knowledge of the crystal chemistry of Zn should shed direct light on the reason for this high geochemical partitioning.

If one excludes the dense and clay fractions, quartz was by far the most abundant mineral systematically detected by XRD in all samples together with some albite and microcline (table 1). Willemite (Zn_2SiO_4) and franklinite ($ZnFe_2O_4$) are the two Zn-bearing primary minerals detected in the slag horizon (MN1) (fig. 6A). Small amounts of these two phases were also detected in the dense fractions of MN2, and trace amounts in MN3. The slag horizon and dense fractions also contain magnesioferrite ($MgFe_2O_4$). This mineral is easily differentiated from franklinite at high Bragg angles (see arrows in fig. 6A) because the unit cell of the magnesium spinel is $7\ 10^{-3}$ smaller than that of the Zn isomorph (a = 8.375 versus 8.441 Å). Willemite, franklinite, and magnesioferrite are issued from grilling and furnace units of the former Zn foundry. Their presence at 40 to 50 cm depth (MN3) indicates a gravitational leaching of fine particles facilitated by the high microporosity of this sandy soil. Physical migration was also confirmed by the optical microscopy observation in deep horizons of small carbon particles used to burn the Zn, Pb ore. Illite, randomly interstratified illite-smectite mixed-layers, and kaolinite were systematically detected by XRD in all clay fractions (fig. 6B). The proportion of chlorite was significant only in MN6. No microcrystalline Fe and Mn oxide minerals were identified.

Speciation of Zn in the slag horizon by powder EXAFS.–An EXAFS spectrum of the dense fraction ($d > 2.9$) of MN1 is presented in figure 7A together with those of franklinite and willemite. The soil spectrum is clearly intermediate between the two references, and its shape and frequency were reproduced by assuming a phase mixture consisting of 41 percent willemite and 28 percent franklinite (fig. 7B, $R_p = 108$). The spectral match between model and experimental spectra is correct since all EXAFS structures and their relative intensities are adequately reproduced. However, the fact that the two components sum to only $S \approx 70$ percent suggests the presence of an additional minor phase. A three component linear fit of the soil spectrum to the model compound database was thus attempted but was unsuccessful. Satisfying simulations were instead obtained by adding to the database EXAFS spectra of the clay fraction in deep horizons. Figure 7C shows the $d > 2.9$ spectrum and the digitally combined spectrum of 40 percent willemite, 25 percent franklinite, and 18 percent MN3 <2 μm. R_p decreased from 108 to 78 by adding this third component, and the three spectra summed to S = 83 percent. This EXAFS analysis confirms the presence of franklinite and willemite in the dense fraction as detected by XRD, but, in addition, it indicates that these two minerals represent the two prominent Zn species (~65 percent), and it provides permissive evidence for Zn association to the clay fraction.

The silt fraction ($\phi < 100$ μm) of MN1 has an EXAFS spectrum intermediate between the dense (MN1 $d > 2.9$) and clay (MN3 < 2 μm) fractions (fig. 8A). The percentage of each Zn species, as estimated from linear combinations, is 17 percent willemite, 12 percent franklinite, and 61 percent clay fraction ($R_p = 82$, fig. 8B). The likeness of the model and soil spectra presented in figure 8B and the fact that individual components sum up to ~90 percent lead to a high confidence level in this structural interpretation.

Three Zn-bearing components were identified in the slag horizon by the combination of XRD and EXAFS: franklinite, willemite, and a Zn-containing clay fraction. The

Fig. 6. Powder X-ray diffraction patterns for (A) the dense fraction ($d > 2.9$) of the slag horizon at Mortagne du Nord (MN1), (B) the clay fraction (<2 μm) of the 40 to 50 cm horizon (MN3) (black: air dried; red: after ethylene glycol solvation), and (C) the <40 μm fraction of Maatheide (M2). B: albite, C: calcite, Fd: feldspar, F: franklinite, H: hemimorphite, Ht: hematite, I: illite, J: jarosite, K: kaolinite, M: magnesioferrite, Ma: magnetite, Mr: magnesioriebeckite, Q: quartz, W: willemite, R0: random illite-smectite mixed-layering.

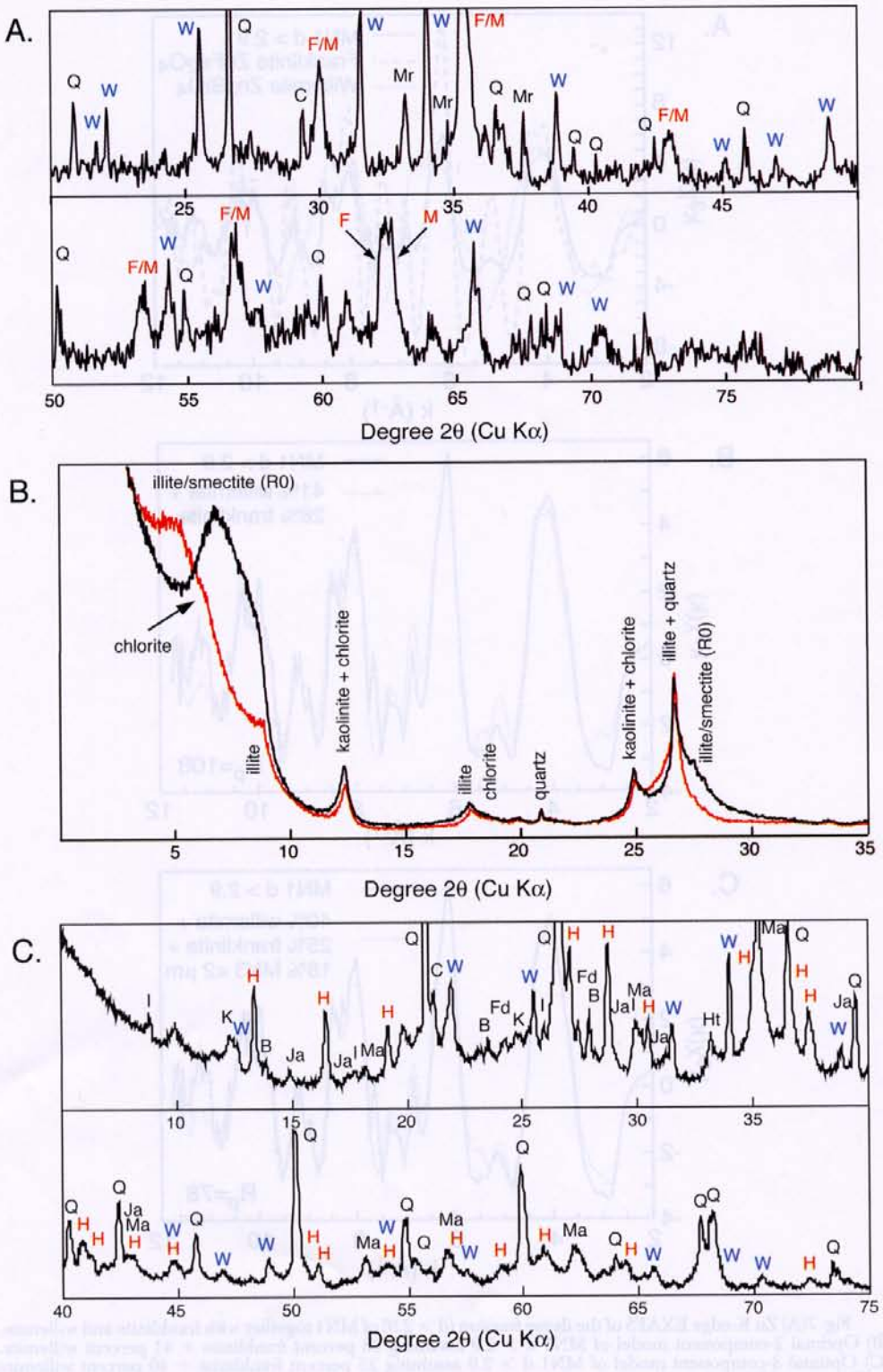
A.
Q
W
F/M
C
Mr
F
M
25
30
35
40
45
50
55
60
65
70
75
Degree 2θ (Cu Kα)
B.
illite/smectite (R0)
chlorite
illite
kaolinite + chlorite
quartz
illite + quartz
5
10
15
20
25
30
35
Degree 2θ (Cu Kα)
C.
I
K
H
B
Ja
Ma
Fd
Ht
10
15
20
25
30
35
40
45
50
55
60
65
70
75
Degree 2θ (Cu Kα)

Figure 6

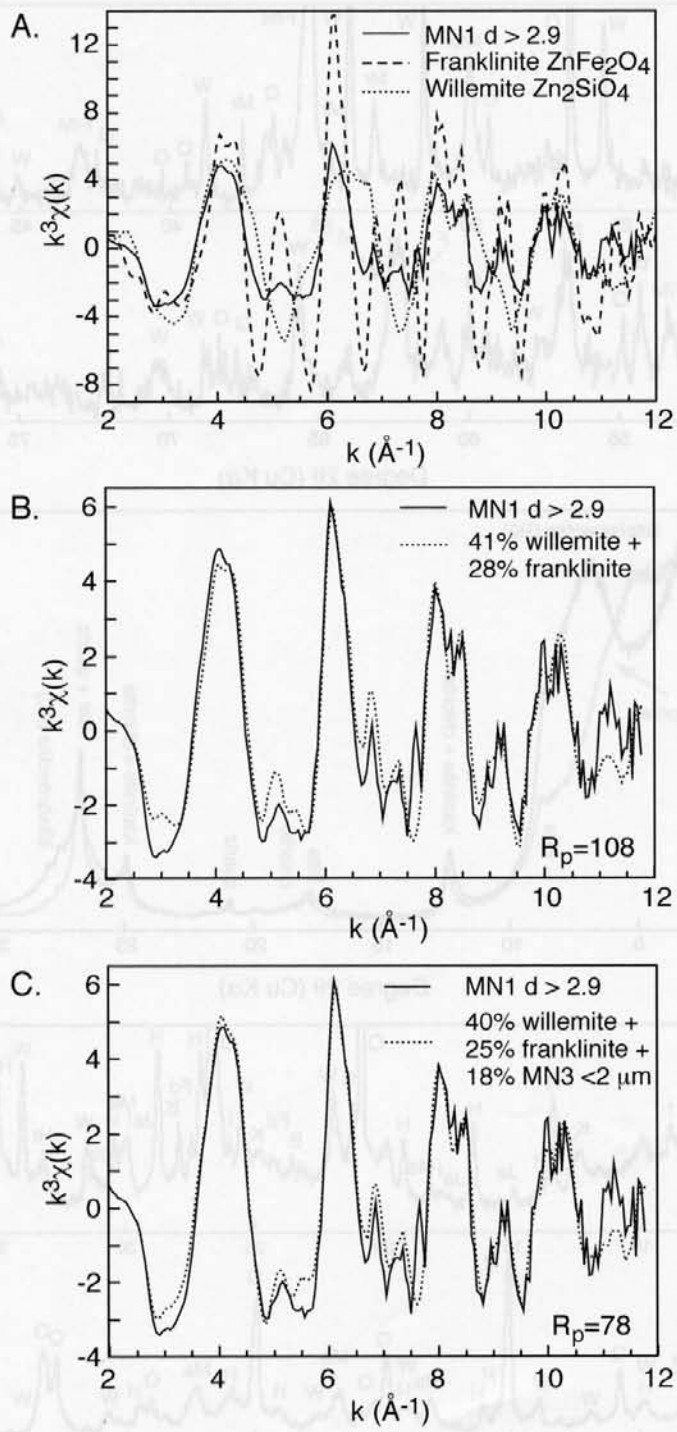

Fig. 7(A) Zn K-edge EXAFS of the dense fraction (d > 2.9) of MN1 together with franklinite and willemite. (B) Optimal 2-component model of MN1 d > 2.9 assuming 28 percent franklinite + 41 percent willemite. (C) Optimal 3-component model of MN1 d > 2.9 assuming 25 percent franklinite + 40 percent willemite + 18 percent MN3 <2 μm fraction.

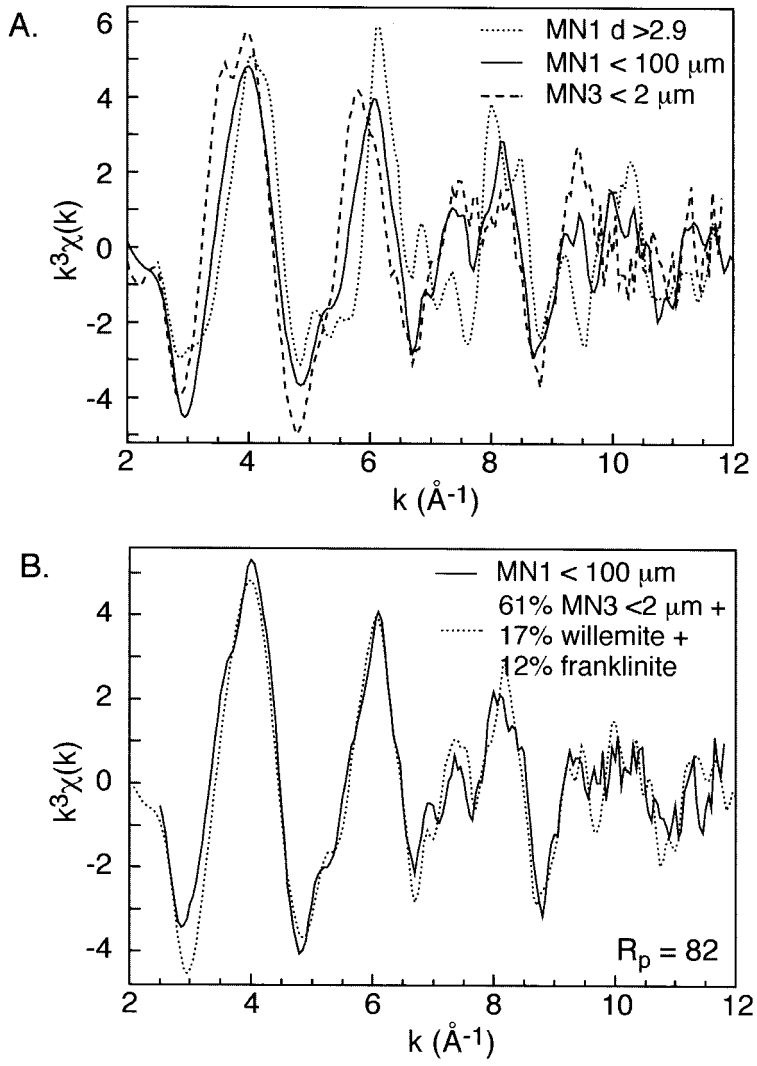

Fig. 8(A) Zn K-edge EXAFS of the dense (d > 2.9) and silt (<100 μm) fraction of MN1 and of the clay fraction (<2 μm) of MN3. (B) Optimal 3-component model of MN1 < 100 μm: 61 percent MN3 < 2 μm + 17 percent willemite + 12 percent franklinite.

clay fraction is obviously multiphase and may therefore contain several Zn-bearing minerals. It will be shown below by μSXRF and μEXAFS that it is indeed the case. The percentage of Zn in the <2 μm fraction can be calculated from its percentage in the <100 μm fraction as evaluated by EXAFS (~61 percent) and from the percentage of this silt fraction in the coarse <2 mm fraction (70 percent) as determined by sieving. This calculation yields $0.61 \times 0.70 = 43$ percent relative to 8 percent estimated previously from the combination of chemical and particle size distribution analyses (fig. 5B). This noticeable discrepancy could arise from an incomplete extraction of the <2 μm fraction from the <100 μm fraction. Sobanska (1999) showed that Zn- and Pb-bearing slag materials contain silty aggregates in which various minerals (quartz, dark minerals . . .) are cemented in an argillic matrix. These aggregates may have been imperfectly

separated during the size fractionation procedure, thus leading to an underestimation of the Zn pool in the extracted <2 μm fraction. But this explanation hardly accounts alone for the whole Zn pool discrepancy obtained by the two independent calculations, because the <100 μm fraction was mechanically agitated for two days and then sonicated before extracting the clay fraction. The proportion of the clay fraction extracted by this procedure was in all likelihood greater than 8 percent/43 percent = 18 percent. In addition, aggregates identified by Sobanska (1999) were larger than 100 μm, and, therefore, the silt fraction is expected to contain relatively few of these cemented heterogeneous grains. A more likely alternative explanation for this discrepancy is proposed as follows: Based on the EXAFS measurements, 61 percent of Zn in the silt fraction of MN1 has a similar chemical form as in the clay fraction from MN3, but the particle size of this 61 percent Zn pool is unknown. EXAFS being a local structural probe does not provide the distinction between Zn associated with the phyllosilicates from the Zn physically associated to coarse particles but having a phyllosilicate-like local atomic environment. For instance, willemite is an anhydrous silicate, and its weathering possibly results in the formation of a Zn-rich phyllosilicate-like surface layer, which therefore could not be separated from willemite core grains. Also, Manceau, Schlegel, Nagy, and Charlet (1999) showed that Co sorption on quartz resulted in the formation of secondary clay coatings on quartz grains. This surface-induced precipitation mechanism can be readily extended to zinc since Zn-phyllosilicates have a lower Gibbs free energy of formation than Co-clays (Decarreau, 1985). In conclusion, although an incomplete extraction of the clay fraction during the size fractionation cannot be completely discounted, the presence of Zn phyllosilicate-like coatings on primary minerals (willemite, quartz) seems a more realistic explanation for the relatively low amount of Zn physically extracted in the clay fraction of MN1 (fig. 5B).

Speciation of Zn in deep and tilled horizons by powder EXAFS.–The combination of chemical, particle size (fig. 5B), and XRD analyses indicated that Zn is taken up by the clay fraction in deep horizons, and that franklinite and willemite have a very low abundance being detected only in the small d > 2.9 coarse fraction. Thus identifying the nature of Zn-bearing phases in clay fractions is a key issue for understanding how Zn is immobilized in contaminated soils. EXAFS spectra of the clay fractions are essentially identical in MN2, MN3, and MN4, which means that Zn species are very similar in soil horizons (fig. 9). These spectra also strongly resemble those of the various fractions for the agricultural field (MN6, fig. 10). In figure 10 EXAFS spectra of the <100, <2, and <0.1 μm fractions are overlain, indicating that Zn has essentially the same chemical form(s) in the two sampling sites, which are representative of contaminated grasslands and agricultural fields present in the vicinity of the former smelter. The presence of organically-bound Zn in MN6 was dismissed by comparing H_2O_2-treated and H_2O_2-untreated soil samples (data not shown).

A first attempt to determine the speciation of Zn is these soil samples was achieved by comparing model spectra in the database to MN3 < 2 μm. The best one-component spectral agreement was obtained with Zn-containing kerolite $Si_4(Mg_{2.25}Zn_{0.75})O_{10}(OH)_2 \cdot nH_2O$ (ZnKer75, R_p = 126, S = 91 percent) or Zn-sorbed hectorite (ZnHec at $\alpha = 35°$, R_p = 208, S = 98 percent, fig. 11). These two Zn-phyllosilicate species each provided a very good match in phase, accounting for almost all spectral features observed in the investigated k-range, but failed at reproducing correctly the wave envelope since kerolite and hectorite have a higher amplitude at 5.5 to 6 $Å^{-1}$ and 7.5 to 8 $Å^{-1}$, respectively (fig. 11A and B). No other reference was found to reproduce as well the phase and structure of the soil samples. The correctness of this approach relies upon the uniqueness of EXAFS spectra to distinct Zn coordination environments, and the spectral sensitivity can be assessed by comparing the MN3 < 2 μm spectrum to a selection of reference spectra in the library (fig. 11C-F). Zn-substituted goethite (R_p = 292, S = 87

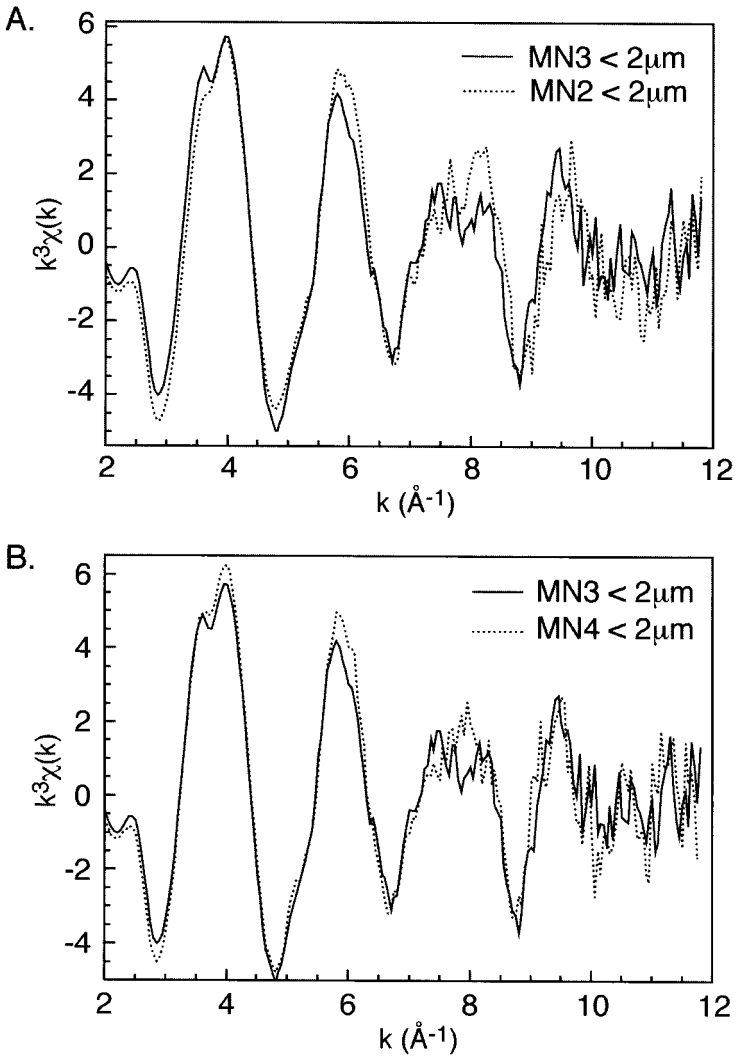

Fig. 9. Zn K-edge EXAFS of the clay fractions of MN2, MN3, and MN4.

percent), Zn-sorbed birnessite (R_p = 356, S = 68 percent), (Zn,Al)-hydrotalcite ($Zn_3Al(OH)_8(CO_3)_{0.5}$) (R_p = 260, S = 63 percent), and hydrozincite ($Zn_5(OH)_6(CO_3)_2$) (R_p = 342, S = 83 percent) clearly yield a poorer spectral match. Apart from the noticeable differences in wave frequency, all these reference spectra have a significantly higher amplitude which was accounted for in the one-component model least-squares fitting by decreasing the value of S, sometimes unrealistically as for birnessite (S = 68 percent) and (Zn,Al)-hydrotalcite (S = 63 percent). This one-component analysis leads to the conclusion that, if present at all, goethite, birnessite, (Zn,Al)-hydrotalcite, and hydrozincite Zn-species are not predominant. The strongest argument in favor of the predominance of a zinciferous phyllosilicate comes from P-EXAFS results presented in the next section.

The comparison of RSFs is also insightful. Figure 12A shows that the RSFs for MN3 < 2 μm and Zn-doped kerolite bear a strong resemblance, both of them possessing

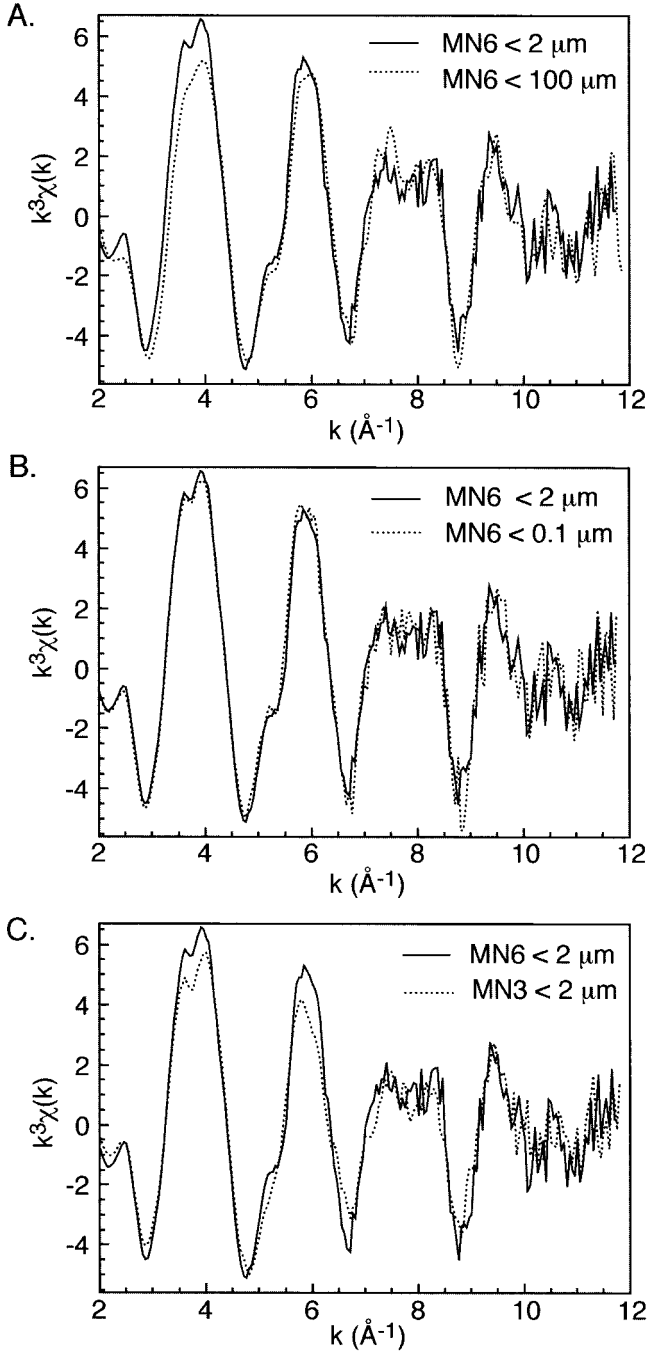

Fig. 10(A, B) Comparison of Zn K-edge EXAFS spectra for the various fractions of MN6. (C) Comparison of MN6 < 2 μm and MN3 < 2 μm.

a second (B) and fourth (D) atomic shell contribution at the same distance and with the same frequency as attested by the match of the imaginary parts in the Fourier transform. This likeness suggests that Zn atoms have, on average, the same atomic environment in the soil sample as in the phyllosilicate reference, that is, they are essentially surrounded by the same type of atoms at similar distances. In phyllosilicates, peak B corresponds to the overlapping contribution of the nearest octahedral shell (Oct_1 = Mg, Al, Fe, Zn) and tetrahedral shell (Tet_1 = Si, Al), and peak D originates from the next-nearest tetrahedral shell (Tet_2 = Si, Al) and from oxygen atoms of the basal plane (O_b, fig. 13A) (Manceau, Chateigner, and Gates, 1998). Manceau and others (1986) showed in a study on Ni-Mg kerolites that the amplitude of peak B is very sensitive to the relative number of Ni and Mg atoms in the second shell of Ni because waves backscattered by Ni and Mg are out-of-phase. The same holds true with Zn as illustrated in figure 12B and C which compare RSFs for the series of synthetic Zn-Mg kerolites with Zn/(Zn + Mg) varying from 1 to 0.01. Thus, the similarity in amplitude of peak B in the soil and ZnKer75 kerolite reference indicates that the second Zn shell contains "heavy" (Zn, Fe) and "light" (Al, Mg) atoms in a similar proportion as in ZnKer75 ([Zn + Fe]/Σcation $\approx$ 0.25). The hypothesis of a Zn-phyllosilicate species in soil samples is also supported by the presence of peak D (Tet_2 shell), because the Zn-Tet_2 contribution is obviously absent in nonsilicate layer structures such as hydrotalcite (fig. 12D) (Manceau, Schlegel, Nagy, and Charlet, 1999). Peak D has however a smaller amplitude in MN3 $<$ 2 µm (fig. 12A) suggesting that Zn could have on average less next-nearest $(Si, Al)_2$ neighbors in the soil than in the phyllosilicate reference. This inference is also consistent with the presence of an additional peak C in the RSF of the soil sample, which suggests the existence of additional Zn species. The nature of the other Zn species will be determined below from the µSXRF and µEXAFS results, following the presentation of texture goniometry and P-EXAFS results.

Speciation of Zn in deep and tilled horizons by texture goniometry and polarized EXAFS.– The experimental (001) pole figures of illite-smectite and kaolinite and the corresponding radial orientation distribution densities (ρ scans) for MN3 and MN6 are presented in figure 14A and B. Pole figures represent the distribution of lattice normals over the unit sphere and are displayed as a contour plot of decreasing orientation density from the center (ρ = 0°). In a randomized powder mount, where crystallites are distributed over all possible orientations, there is no variation in diffracted intensity with ρ after correction of the eventual defocusing. Figure 14 shows that orientation densities have instead a narrow distribution, with a maximum around ρ = 0. The rapid density decrease as the specimen ρ angle increases indicates that the majority of clay plates have their c* axis normal to the film plane (that is, ab planes parallel to the film plane). Examination of ρ scans shows that kaolinite has systematically a strong texture with a maximum of distribution density (P_{max}) equal to 14.0 m.r.d. in MN3 (FWHM = 23.1°) and 16.4 m.r.d. in MN6 (FWHM = 32.6°). Illite-smectite layers in MN3 are quite poorly aligned in the film plane (P_{max} = 5.2 m.r.d., FWHM = 39.9°), compared to other samples. For this sample, the minimum of the distribution density at high ρ angles (P_{min}) equals 0.7 instead of zero in MN6, which means that a random component is present. Apart from illite-smectite layers in MN3, textural analysis indicates that the dispersion of individual clay crystallite c* axes in films is relatively low (FWHM $<$ 35°) and comparable to that reported for smectite references (Manceau, Chateigner, and Gates, 1998; Manceau, Drits, and others, 2000; Manceau, Lanson, and others, 2000). In these studies we showed that (1) P-EXAFS spectra of self-supporting films from fine-grained clay standards could be treated as single phyllosilicate slabs if the dispersion from perfect alignment of particles in the film plane was lower than about ±15° (FWHM = 30°) and (2) that an important polarization dependence could still be observed when the dispersion amounted to ±22° (FWHM = 44°). Since phyllosilicates in soil films have a FWHM $<$40°, Zn

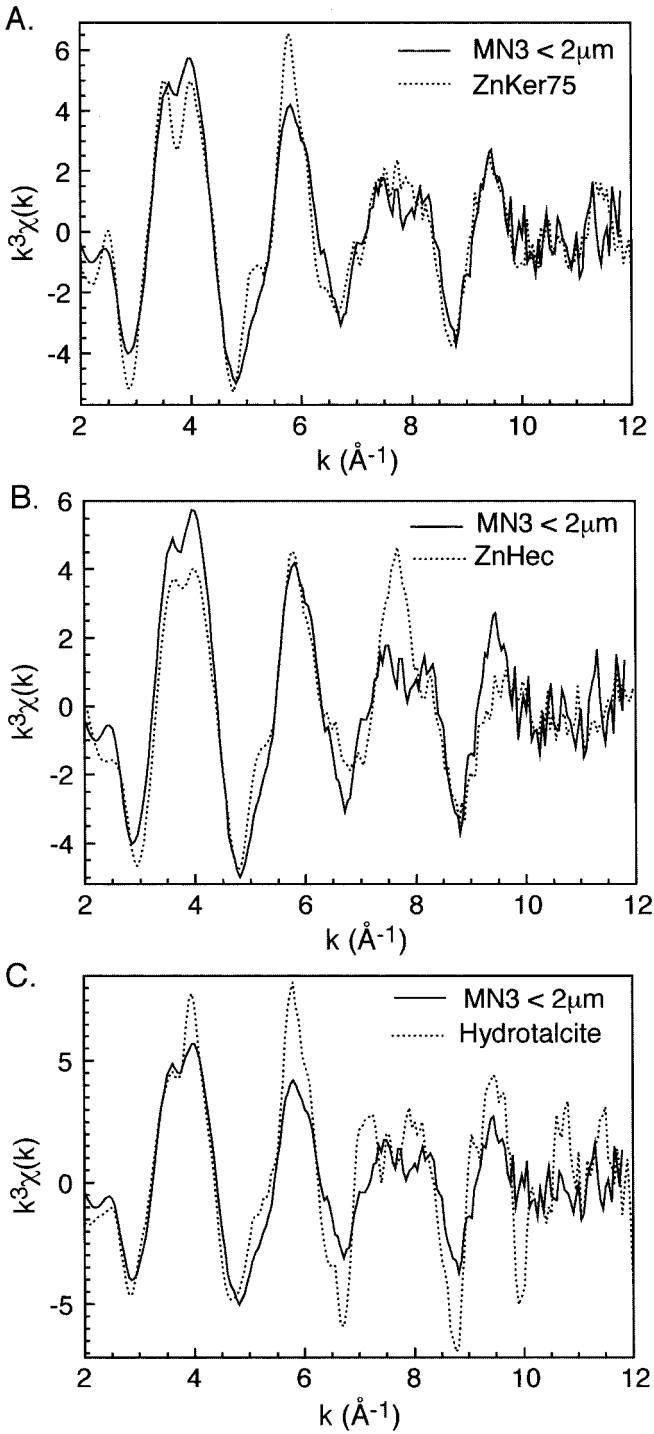

Fig. 11. Comparison of Zn K-edge EXAFS of MN3 < 2 μm to a selection of Zn references. Zn-substituted kerolite (ZnKer75, $Si_4(Mg_{2.25}Zn_{0.75})O_{10}(OH)_2 \cdot nH_2O$); Zn-sorbed hectorite ($Na_{0.35}Mg_{2.65}Li_{0.35}Si_4O_{10}(OH)_2$, powder spectrum, $\alpha = 35°$); hydrotalcite ($Zn_3Al(OH)_8(CO_3)_{0.5}$); hydrozincite ($Zn_5(OH)_6(CO_3)_2$); Zn-substituted goethite (ZnGt, $\alpha(Fe_{0.97}Zn_{0.03})OOH$); Zn-sorbed birnessite (ZnBi3, Zn/Mn = 0.126).

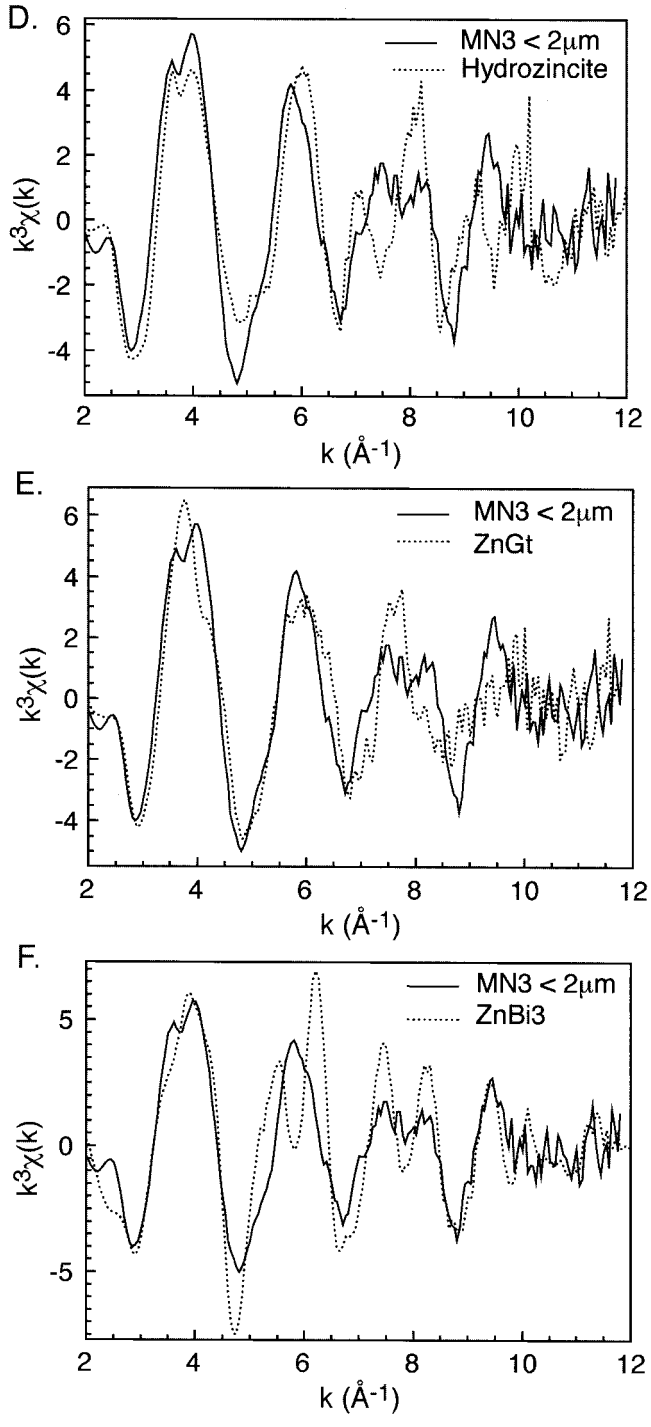

Fig. 11 (continued)

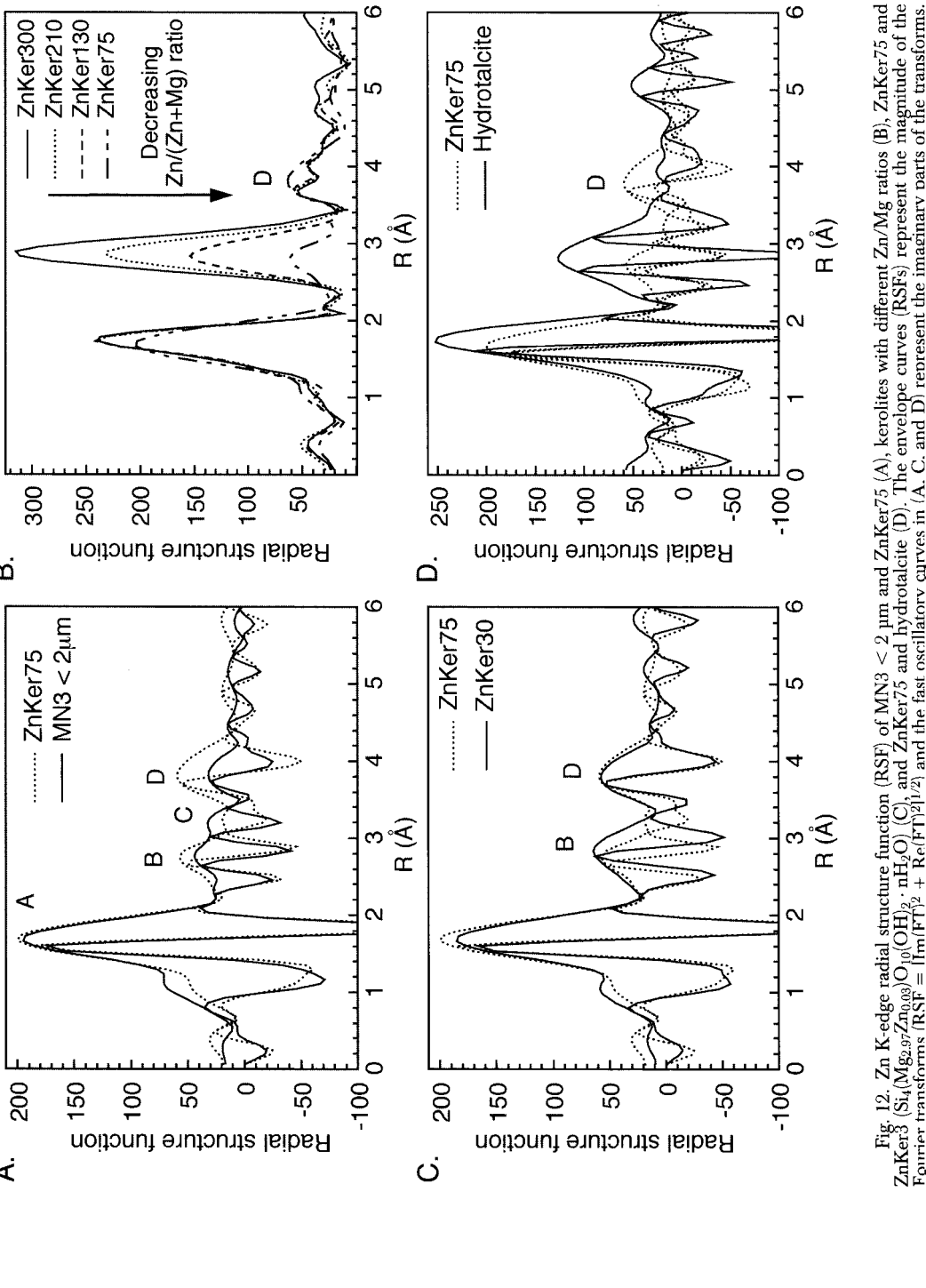

Fig. 12. Zn K-edge radial structure function (RSF) of MN3 < 2 μm and ZnKer75 (A), kerolites with different Zn/Mg ratios (B), ZnKer75 and ZnKer3 ($Si_4(Mg_{2.97}Zn_{0.03})O_{10}(OH)_2 \cdot nH_2O$) (C), and ZnKer75 and hydrotalcite (D). The envelope curves (RSFs) represent the magnitude of the Fourier transforms /RSF = $|Im(FT)^2 + Re(FT)^2|^{1/2}$ and the fast oscillatory curves in (A, C, and D) represent the imaginary parts of the transforms.

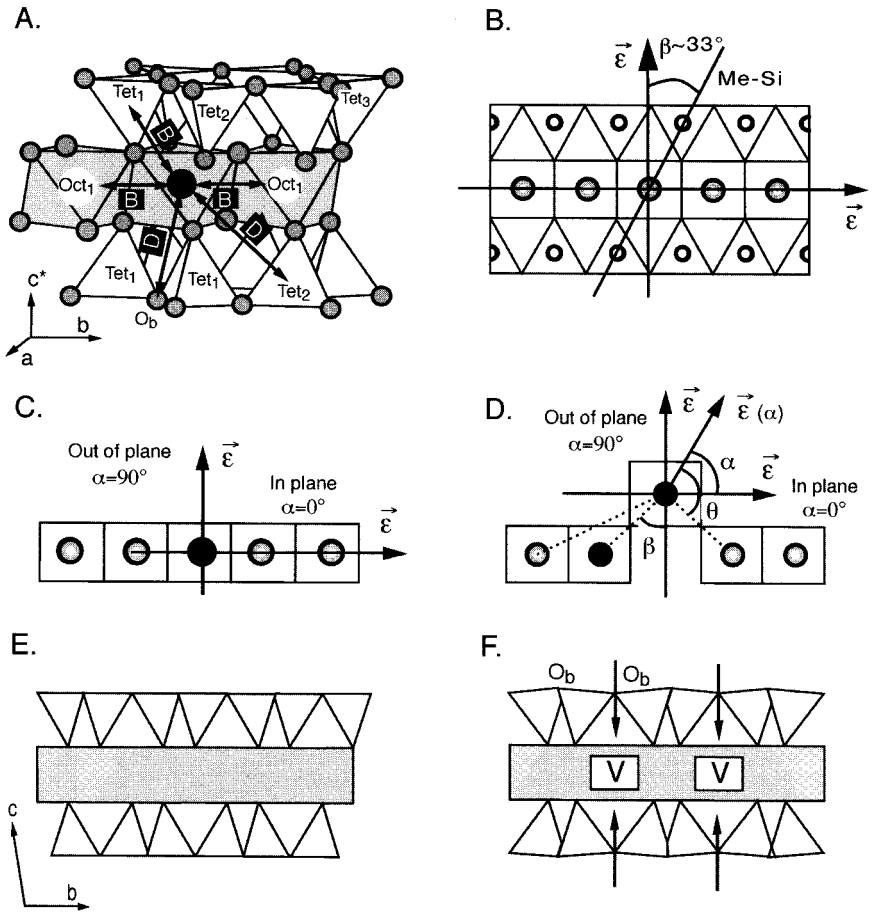

Fig. 13(A) Representation of the successive atomic shell contributions to EXAFS around Zn in the octahedral sheet of a 2:1 phyllosilicate. (B-D) Possible relative orientations of a phyllosilicate (B) and a phyllomanganate layer (C, D) to the electric field vector ϵ. α is the angle between the layer, and ϵ, β is the angle between the vector connecting the atomic pair of interest and the perpendicular to the layer, and θ is the angle between the vector connecting the atomic pair of interest and ϵ. Black atoms are X-ray absorbers (Zn) and gray atoms are X-ray backscatterers. (E, F) Schematic representation of the 2:1 phyllosilicate structure down [100]. Trioctahedral structures have a flat basal plane (E), whereas dioctahedral structures have a corrugated basal plane (F) due to the presence of octahedral vacant sites noted V.

P-EXAFS spectra should normally exhibit a marked angular dependence, if Zn is bound to phyllosilicates. However, it should be kept in mind that an absence of polarization dependence would not prove that Zn is not associated to phyllosilicates nor to any other fine-grained layered mineral, because the films can include some randomly oriented two-dimensional crystallites ($P_{min} > 0$) as in the case of clay coatings on quartz grains. Consequently, the observation of a dichroic EXAFS signal from highly oriented films of clayey soil materials is a diagnostic, but not the only, criterion for the existence of metal-containing phyllosilicates.

Polarized EXAFS spectra of MN3 and MN6 are shown in figure 15. Pronounced angular variations of EXAFS spectra as a function of experimental angle (α) are noted on the two first oscillations. This remarkable polarization dependence of EXAFS spectra demonstrates that the average local structure of Zn is anisotropic and also that the

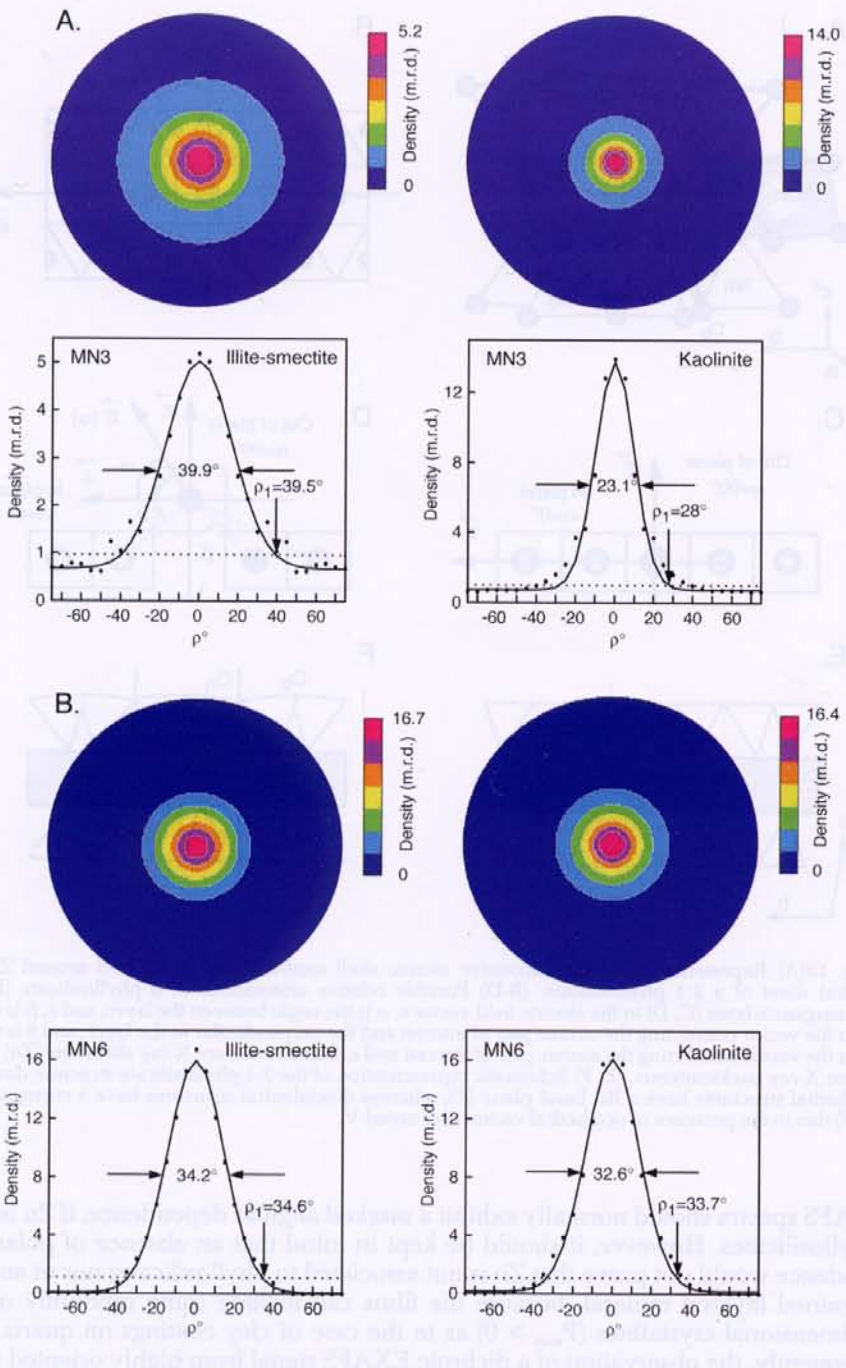

Fig. 14. X-ray diffraction (001) pole figures (displayed as a contour map) and corresponding radial orientation distribution densities (ρ scan) of the dispersion of illite-smectite (left) and kaolinite (right) platelets off the film plane for the three self-supporting films studied by P-EXAFS (A = MN3, B = MN6, C = E2). Pole figures were corrected for background, defocusing, volumetric and absorption variations, and then normalized to distribution densities. The strong maximum of density at the center of the (001) pole figures quantifies the [001]* fiber texture (ρ = 0°). Linear density scale and equal area projection are used for the pole figures. ρ scans are radial sections of pole figures. The 1 m.r.d. density level (perfectly random powder) is represented by a horizontal dotted line. Points: experimental normalized values, full lines: Gaussian fit.

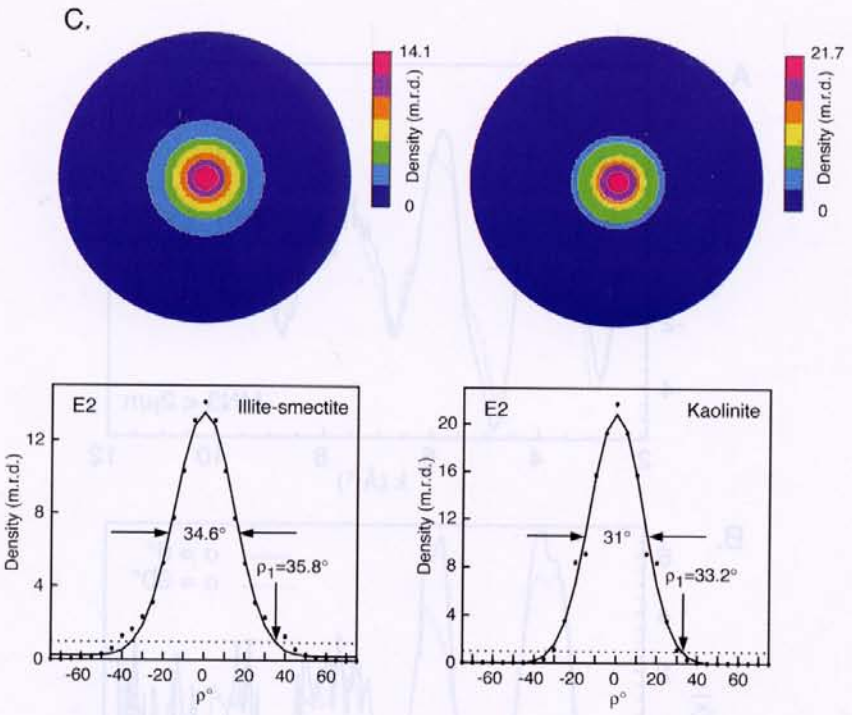

Fig. 14 (continued)

predominant Zn-bearing phase was oriented together with clay minerals during the film preparation. To identify this Zn species, P-EXAFS spectra for the most likely minerals were either measured or calculated by ab-initio methods when not available. Four references were considered: Zn-sorbed birnessite (ZnBi), hydrozincite, (Zn,Al)-hydrotalcite, and Zn-sorbed hectorite (fig. 4). Figure 16 shows that they all display a contrasted angular dependence due to the difference of structural environment of Zn in these compounds. In P-EXAFS measurements, the amplitude of the EXAFS contribution for each atomic pair depends on its angle with respect to the electric field vector ϵ (fig. 13B-D; table 3). This angular dependence for K edges can be written (Lee and Pendry, 1975; Stern and Heald; 1983, Teo, 1986):

$$\chi(k, \theta) = \sum_j \sum_{i=1}^{N_j} 3 \cos^2 (\theta_i^j) \chi_{iso}^j(k)$$

where the index j runs over all atomic shells around the absorbing atom, the index i runs over all N_j atoms of the jth shell, θ_i^j is the angle between the polarization vector ϵ and the vector r_i^j which connects the absorbing atom to the ith atom of the jth shell, and χ_{iso} is the EXAFS amplitude for the powder spectrum. This formula shows that, in an oriented sample, the signal from a given neighboring atom is enhanced by a factor of three when its radius vector lies along the direction of the X-ray polarization vector. For self-supporting films, the variation of the EXAFS amplitude $\chi_j(k, \theta)$ with the angle (α) between ϵ and the layer solely depends on the angle (β) between the vector connecting

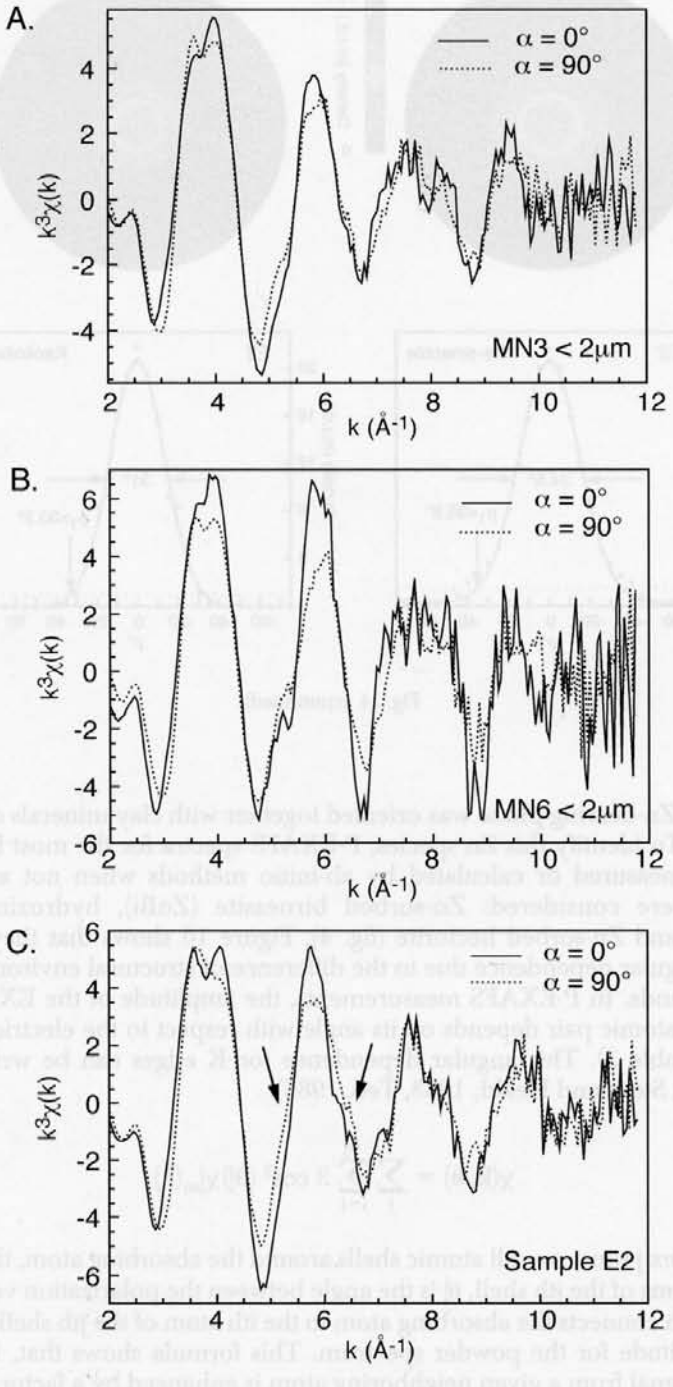

Fig. 15. In-plane (α = 0°) and out-of-plane (α = 90°) Zn K-edge P-EXAFS spectra of MN3 < 2 μm (A), MN6 < 2 μm (B), and E2 (C).

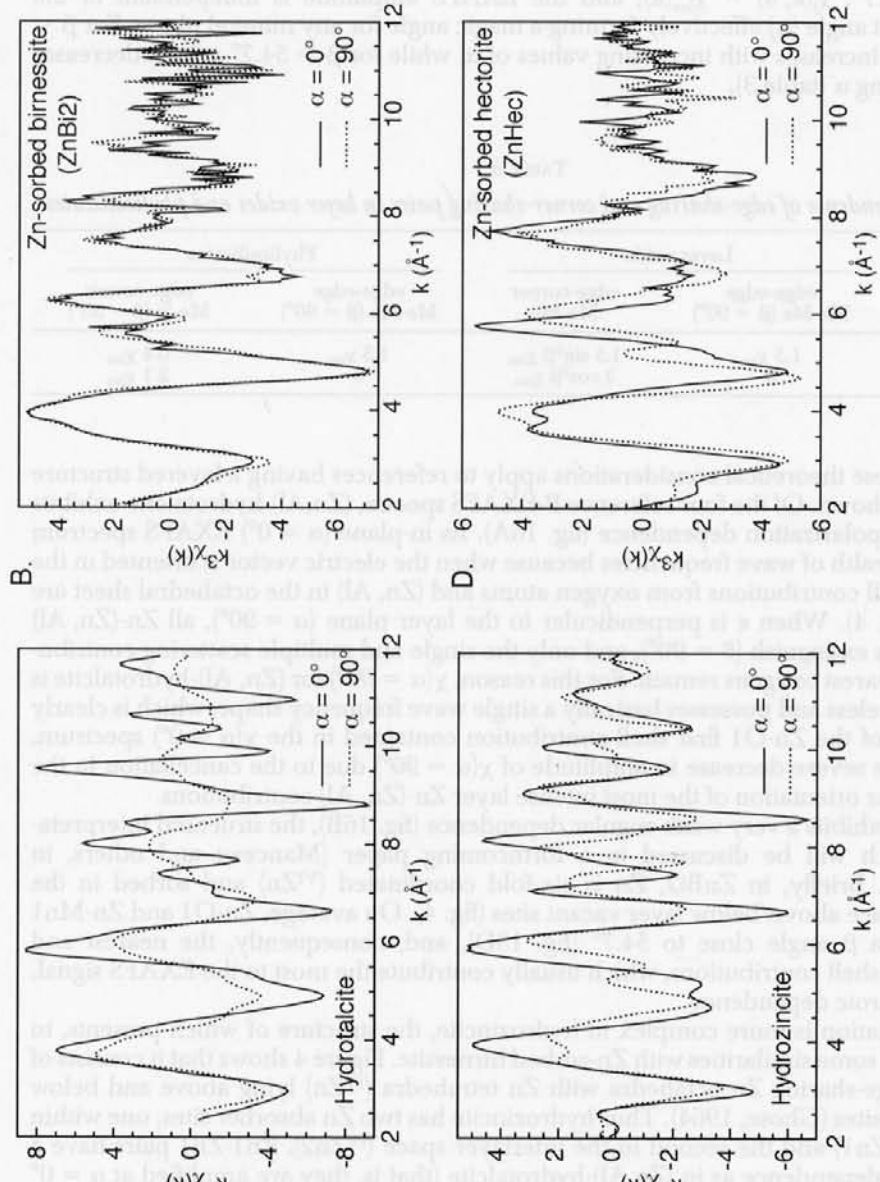

Fig. 16. In-plane ($\alpha = 0°$) and out-of-plane ($\alpha = 90°$) Zn K-edge P-EXAFS spectra. (A) Theoretical spectra for hydrotalcite ($Zn_3Al(OH)_8(CO_3)_{0.5}$) calculated using the ab initio single- and multiple-scattering code FEFF, version 7.02 (Rehr and others, 1991) using the following parameters: S_0^2 (amplitude reduction factor) = 0.85; σ(Zn-O_1) = 0.085 Å, σ(Zn-[Al, Zn]$_1$) = 0.09 Å, σ = 0.10 Å for longer distance single scattering paths (χ_2), and σ = 0.09 Å for multiple scattering paths ($\chi_{3,4}$). (B) Experimental spectra for Zn-sorbed birnessite (ZnBi2). (C) Theoretical spectra for hydrozincite ($Zn_5(OH)_6(CO_3)_2$) calculated with FEFF 7.02 and using S_0^2 = 0.85; σ(Zn-O_1) = 0.08 Å, σ(Zn-$Zn_{1,2}$) = 0.09 Å, σ = 0.10 Å for longer distance single scattering paths (χ_2), and σ = 0.11 Å for multiple scattering paths ($\chi_{3,4}$). (D) Experimental spectra for Zn-sorbed hectorite (ZnHec).

the atomic pair of interest (j) and the perpendicular to the layer (fig. 13B and D, Manceau, Chateigner, and Gates, 1998):

$$\chi_j(k, \theta) = 3[\cos^2 \beta \sin^2 \alpha + (\sin^2 \beta \cos^2 \alpha)/2]\chi^j_{iso}(k)$$

For $\beta = 54.7°$, $\chi_j(k, \theta) = \chi^j_{iso}(k)$, and the EXAFS amplitude is independent of the measurement angle (α) effectively forming a magic angle for any mineral phase. For $\beta < 54.7°$ $\chi_j(k, \theta)$ increases with increasing values of α, while for $\beta > 54.7°$ $\chi_j(k, \theta)$ decreases with increasing α (table 3).

TABLE 3

Angular dependence of edge-sharing and corner-sharing pairs in layer oxides and phyllosilicates

	Layer oxide		Phyllosilicates	
	edge-edge Me-Me ($\beta = 90°$)	edge-corner Me-Me	edge-edge Me-Me ($\beta = 90°$)	edge-corner Me-Si ($\beta \sim 33°$)
$\alpha = 0°$	$1.5\ \chi_{iso}$	$1.5 \sin^2\beta\ \chi_{iso}$	$1.5\ \chi_{iso}$	$0.4\ \chi_{iso}$
$\alpha = 90°$	0	$3 \cos^2\beta\ \chi_{iso}$	0	$2.1\ \chi_{iso}$

How these theoretical considerations apply to references having a layered structure will now be shown. Of the four reference P-EXAFS spectra, (Zn,Al)-hydrotalcite exhibits the simplest polarization dependence (fig. 16A). Its in-plane ($\alpha = 0°$) EXAFS spectrum contains a wealth of wave frequencies because when the electric vector is oriented in the layer plane all contributions from oxygen atoms and (Zn, Al) in the octahedral sheet are summed (fig. 4). When ϵ is perpendicular to the layer plane ($\alpha = 90°$), all Zn-(Zn, Al) contributions extinguish ($\theta = 90°$), and only the single and multiple scattering contributions from nearest oxygens remain. For this reason, $\chi(\alpha = 90°)$ for (Zn, Al)-hydrotalcite is almost featureless and possesses basically a single wave frequency shape, which is clearly reminiscent of the Zn-O1 first shell contribution contained in the $\chi(\alpha = 0°)$ spectrum. Note also the severe decrease in amplitude of $\chi(\alpha = 90°)$ due to the cancellation in the perpendicular orientation of the most intense layer Zn-(Zn, Al) contributions.

ZnBi2 exhibits a very weak angular dependence (fig. 16B), the structural interpretation of which will be discussed in a forthcoming paper (Manceau and others, in preparation). Briefly, in ZnBi2, Zn is six-fold coordinated (^{VI}Zn) and sorbed in the interlayer space above/below layer vacant sites (fig. 4). On average, Zn-O1 and Zn-Mn1 shells have a β angle close to 54.7° (fig. 13D), and, consequently, the nearest and next-nearest shell contributions, which usually contribute the most to the EXAFS signal, have no dichroic dependency.

The situation is more complex in hydrozincite, the structure of which presents, to some extent, some similarities with Zn-sorbed birnessite. Figure 4 shows that it consists of layers of edge-sharing Zn octahedra with Zn tetrahedra (^{IV}Zn) lying above and below layer vacant sites (Ghose, 1964). Thus hydrozincite has two Zn absorber sites, one within the layer (^{VI}Zn1) and the second in the interlayer space (^{IV}Zn2). Zn1-Zn1 pairs have a polarization dependence as in (Zn,Al)-hydrotalcite (that is, they are amplified at $\alpha = 0°$ and extinguished at $\alpha = 90°$). ^{IV}Zn2-^{VI}Zn1 pairs are detected at both $\alpha = 0°$ and 90° like ^{VI}Zn-Mn1 pairs in Zn-sorbed birnessite, but the ^{IV}Zn2-^{VI}Zn1 pair contribution is dichroic ($\beta \neq \sim 54.7°$), because interlayer Zn is obviously closer to the octahedral sheet in a 4-fold than in a 6-fold coordination ($\beta_{tet} > \beta_{oct}$). It results from these structural considerations that in hydrozincite $\chi(\alpha = 0°)$ contains predominantly Zn1-O1, Zn1-Zn1, Zn1-Zn2, Zn2-O1, Zn2-Zn1 contributions, whereas $\chi(\alpha = 90°)$ contains essentially Zn1-O1, Zn1-Zn2, Zn2-O1, Zn2-Zn1 contributions. The main difference between the two polarization angles is the cancellation of layer Zn1-Zn1 interactions in the perpendicular orientation.

The consequences on EXAFS spectra are a loss of amplitude at $\alpha = 90°$ and a strong anisotropy of the spectral shape and frequency (fig. 16C).

In Zn-sorbed hectorite, Zn octahedra are located at layer edges and share 1.6 ± 0.4 edges with surface $Mg(O, OH)_6$ octahedra from the octahedral sheet and 2.2 ± 0.5 corners with SiO_4 tetrahedra from the tetrahedral sheet (Schlegel and others, 1999) (fig. 4). The Zn-Mg and the Zn-Si pairs have a β angle of 90° and ~30°, respectively, which means that the first pair is amplified at $\alpha = 0°$ and extinguished at $\alpha = 90°$ while the second is lowered at $\alpha = 0°$ and amplified at $\alpha = 90°$ (fig. 13B; table 3). This strong angular dependence upon polarization is observed in figure 16D, which shows that $\chi(\alpha = 0°)$ and $\chi(\alpha = 90°)$ spectra have a much different structure but also a different phase because d(Zn-Mg) = 3.03 Å and d(Zn-Si) = 3.27 Å. Note that, in contrast to (Zn,Al)-hydrotalcite and hydrozincite spectra that have a lower amplitude at $\alpha = 90°$, hectorite has almost the same wave amplitude in the two orientations. This is due to the fact that the contribution from the octahedral sheet (~2 nearest Mg) in the in-plane orientation is similar to that of the tetrahedral sheet (~2 nearest Si) in the out-of-plane orientation.

The comparison of P-EXAFS spectra for reference compounds and soil samples now allows us to dismiss (Zn, Al)-hydrotalcite, hydrozincite, and birnessite as the major Zn-species, thus confirming the powder EXAFS results. Indeed, a careful inspection of spectra in figure 15 shows that (1) the shape of the two first oscillations changes with the measurement angle, (2) the wave phase of the third, and the fourth for MN6, oscillations slightly, but distinctly, vary with α, and (3) the amplitude of the EXAFS signal is not uniformly reduced with α over the whole k-range. Based on the previous discussion on P-EXAFS for reference compounds, all these observations are compelling evidence for Zn-phyllosilicate as the prominent phase responsible for the measured polarization dependence of soil EXAFS spectra.

μSXRF and μEXAFS.–Examination of soil thin sections by optical microscopy showed the same micromorphology and mineralogy in the different horizons. The representative plane-light photomicrograph presented in figure 17 shows an abundance of quartz occurring as large euhedral grains of various sizes (~400 to ~10 µm). In some locations quartz grains are aligned in veins suggestive of fluid precipitation in micropores. Quartz grains are embedded in a brown, Fe-rich, clay matrix containing an extensive micropore system within which dissolved Fe and Mn can diffuse and precipitate. For instance, a black spherical zone characteristic of higher Mn is shown in figure 17B. The energy dispersive X-ray spectrum plotted in figure 3 was obtained on this Mn-rich differentiated fabric with distinct external boundaries.

Characteristic Mn, Fe, Zn, and K/Si X-ray fluorescence maps for the clay matrix presented in figure 17A and the Mn-rich spherule in figure 17B are displayed in figure 18A and B, respectively. In these two maps, the highest Zn concentrations are encountered in Fe-rich grains, but Zn is also partly distributed with Fe in a larger area having a somewhat irregular shape and diffuse external boundaries in the soil clay matrix and with Mn in the manganiferous nodule. The presence of three prominent pools for Zn was confirmed by the plot of µSXRF intensities. The patterns of interelement relationships indicate no (fig. 19A) or very little (fig. 19B) correlation between Fe and Mn. In the first map Zn is strongly correlated to Fe, but two regions can be distinguished in the Fe-Zn diagram of figure 19A. Most points have a (Fe, Zn) normalized intensity which lies between (0, 0) and (0.004, 0.4) (arbitrary unit), whereas a few have higher values ranging between (0.004, 0.4) and (0.012, 1.0). The first group of points corresponds to the clay matrix and the second to Fe grains. Examination of figure 19B leads to similar conclusions: although the highest Zn concentrations are also encountered in Fe grains; this Zn pool accounts for a small fraction of total Zn. Most Zn is predominantly associated with Mn in the spherule.

The mineralogical nature of Fe and Mn constituents was identified by micro-EXAFS. Three Fe K-EXAFS spectra were recorded, one on a Fe grain in the map of

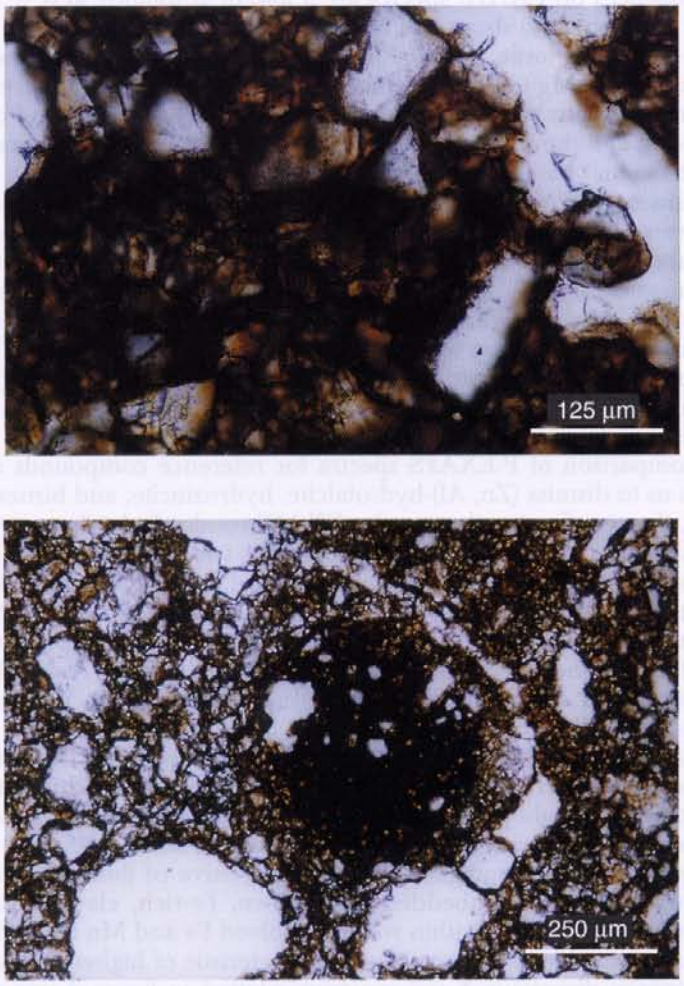

Fig. 17. Representative photomicrographs in transmission of soil thin sections from Mortagne du Nord. (A) Quartz grains and brown, Fe-rich, clay matrix (MN3). (B) Dark spherical fabric enriched in Mn (MN4).

figure 18B, a second on a Fe grain of figure 18A, and a third in the Fe matrix of figure 18A. These three spectra looked very similar (data not shown), and the comparison with model compounds revealed a close similarity with feroxyhite (δFeOOH) (fig. 20A). The Mn K-edge spectrum recorded in the manganiferous nodule closely resembled hexagonal birnessite (fig. 20B). A micro Zn-EXAFS spectrum was collected at the same location as the Mn measurement to determine the uptake mechanism of Zn by birnessite. The Zn-EXAFS spectrum bears strong resemblances with ZnBi1 and has a lower wave frequency than ZnBi2 and ZnBi3 reflecting a decrease of interatomic distances (fig. 20C and D). This noteworthy dissimilarity is also observed on the RSFs: Zn-O and Zn-Mn peaks are shifted to higher R values in ZnBi3, as are their corresponding imaginary parts (fig. 21).

The origin of the difference of Zn-O and Zn-Mn bond lengths in birnessite as a function of the surface coverage is examined now. In all ZnBi samples Zn is sorbed

above/below vacant sites of the phyllomanganate layer, but it is predominantly six-fold coordinated at high surface coverage (ZnBi2, ZnBi3, fig. 4) (Silvester, Manceau, and Drits, 1997), and four-fold coordinated at low surface coverage (ZnBi1, Manceau and others, in preparation). As for ^{IV}Zn2 in hydrozincite, interlayer ^{IV}Zn in birnessite is closer to the octahedral sheet than interlayer ^{VI}Zn leading to a reduction of the Zn-O and Zn-Mn distances. The change of Zn coordination with surface loading can be rationalized by considering the stacking mode of birnessite, which is monoclinic or rhombohedral in Zn-rich birnessites (such as ZnBi3) and predominantly hexagonal in Zn-poor birnessites (such as ZnBi1) (Lanson and others, in preparation). To examine this rationale, let us consider phyllomanganate structures in terms of close-packed models. The mutual arrangement of successive layers can be described by the usual close-packed notation A, B, and C, and a, b, c, in which capital letters stands for non-equivalent crystallographic O, OH, and H_2O sites, and lowercase letters for the positions of Zn. In this symbolic representation, the structure of low pH one-layer monoclinic birnessite and chalcophanite can be written symbolically as (Lanson and others, 2000) . . . AcBc' A'b'CbAb'C'a'BaC . . . , where prime notation stands for interlayer Zn and H_2O/OH positions (fig. 22A). Anions from successive layers are close packed (ABA'CAC'BC) so that interlayer cations in a', b', and c' positions are octahedrally coordinated. The distance between water molecules and nearest oxygen atoms from the adjacent layer ($^{VI}d(H_2O\text{-}O)_{Mono}$) can be calculated from the layer basal distance (d(001) = 7.07 Å), the b unit cell parameter (b = $a/\sqrt{3}$ = 2.85 Å), the layer thickness (2.00 Å), and the translation vector $+\vec{a}/3$ from a layer to the next (fig. 22a). This calculation yields ($^{VI}d(H_2O\text{-}O)_{Mono}$) = 3.13 Å, which is characteristic for hydrogen bonding distances (~2.6 to 3.1 Å). If Zn were tetrahedrally coordinated, the stacking mode would be $AcB^{c'C'}_{B'b'}CbA^{b'B'}_{A'a'}BaC$ . . . and $^{IV}d[(H_2O, OH)\text{-}O]_{Mono}$ = 2.05 Å taking d(^{IV}Zn-(O, H_2O) = 1.96 Å) (fig. 22b). The $^{IV}d[(H_2O, OH)\text{-}O]_{Mono}$ distance is irrealistically short. The same line of reasoning can be applied to hexagonal Zn-containing birnessite. In a one-layer . . . AcB AcB . . . hexagonal stack, interlayer cations above/below layer vacant sites can be either six-fold (. . . $AcB^{c'A'}_{B'b'}$,AcB. . .) (fig. 22B) or four-fold (. . . $AcB^{c'C'}_{C'c'}$AcB . . .) coordinated (fig. 22C and D). In the first case, water molecules in the interlayer (A' and B') form empty prisms with oxygen atoms of the adjacent layer (A'A and B'B stacking). In the second case, all successive anionic layers are close-packed. Simple geometrical calculations lead to $^{VI}d(H_2O\text{-}O)_{Hex}$ = 2.67 Å and $^{IV}d[(H_2O, OH)\text{-}O]_{Hex}$ = 2.63 Å. Therefore, the hexagonal structure allows the formation of hydrogen bonds whatever the Zn coordination. However, the reason why Zn is preferentially four-fold coordinated in ZnBi1 remains unclear. The gain in energy resulting from this coordination is likely related to interlayer forces because Zn^{2+} has no crystal field stabilization energy owing to its d^{10} electronic configuration and has therefore a flexible coordination chemistry in minerals (Douglas, McDaniel, and Alexander, 1994). Consequently, the stacking mode of phyllomanganate layers is thought to be a key factor in controlling the coordination of sorbed Zn, since Zn can only be six-coordinated in monoclinic and rhombohedral birnessite while it is preferentially four-coordinated in one-layer hexagonal birnessite.

This unprecedented micro-mineralogical investigation demonstrates the unique potential of coupled μSXRF and μEXAFS measurements to determine metal species directly on a very small spatial scale in chemically and structurally heterogeneous natural systems. We concluded that the soil from Mortagne du Nord contains a mixture of Zn-bearing phases, among which Zn-sorbed birnessite and Zn-containing Fe (oxyhydr)oxide (feroxyhite-like) grains were unambiguously identified. Apart from these grains, Zn is quite uniformly present with Fe in the soft mass of the clay matrix. But the determination of this third Zn species by μEXAFS was hampered by the present detection limit of the spectrometer. In an effort to evaluate statistically this micro-mineralogical study and to be more conclusive on the nature of the unidentified third Zn species, seven maps were

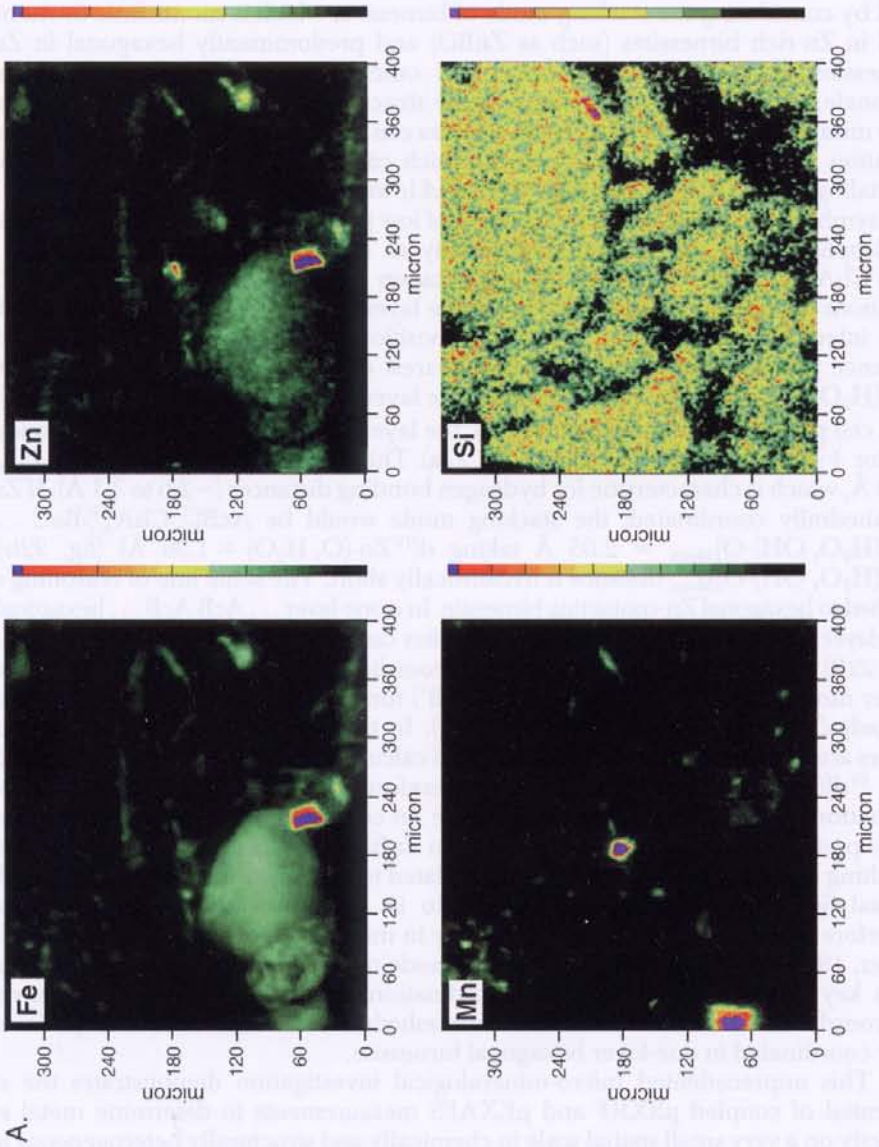
A.
Fe
Zn
Mn
Si
micron
0
60
120
180
240
300
360
400

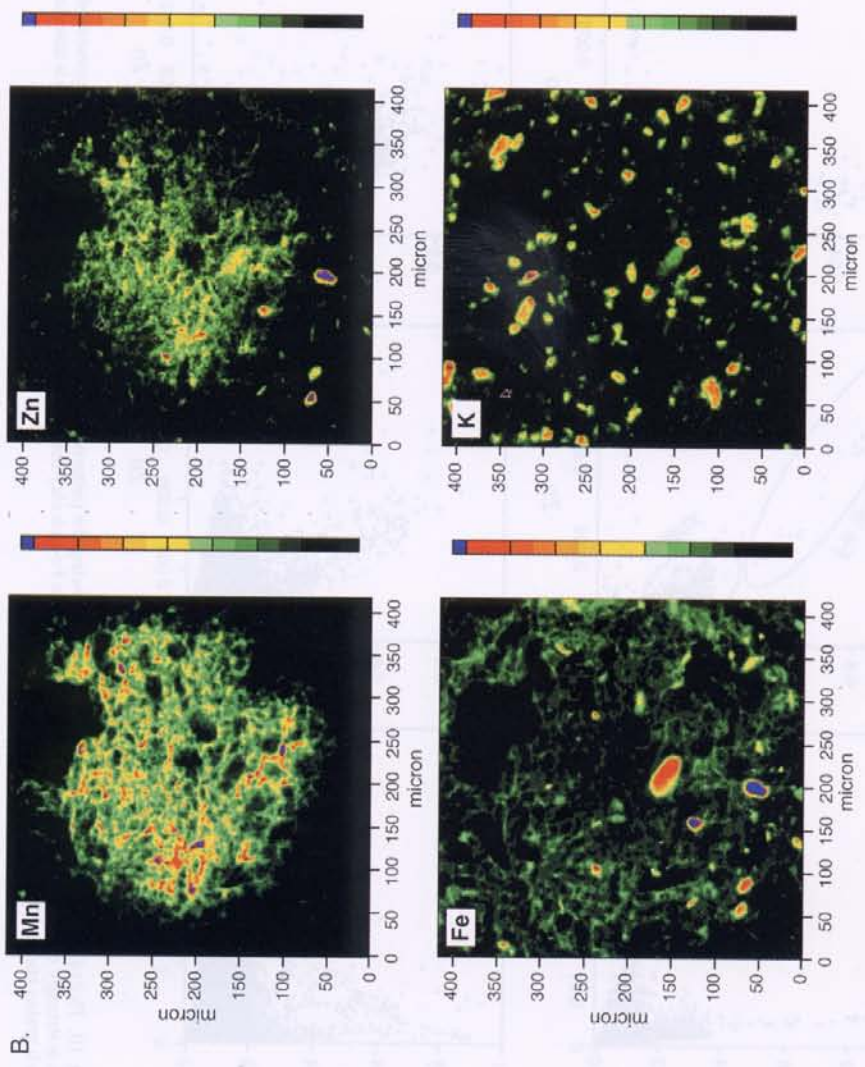

Fig. 18. Synchrotron-based micro-X-ray fluorescence (μSXRF) elemental maps of the clay matrix presented in figure 17A (A) and of the Mn-rich dark brown spherule presented in figure 17B (B). Fe is distributed in Fe-rich grains and in the clay matrix in (A) and in Fe-rich grains and Mn oxides in (B). Owing to the overlap between Mn Kβ and Fe Kα fluorescence peaks, the Fe maps were recorded with the Fe Kβ emission line.

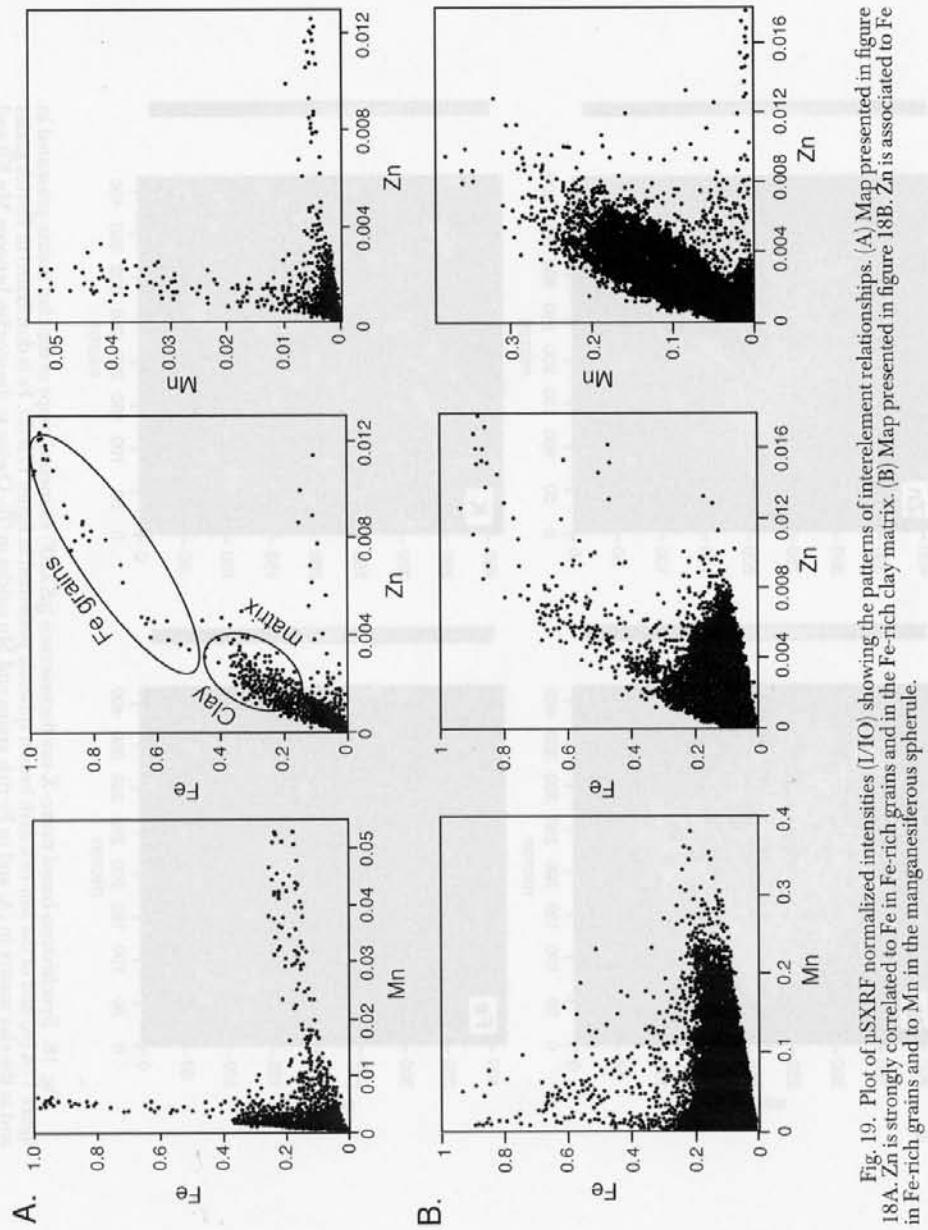

Fig. 19. Plot of μSXRF normalized intensities (I/IO) showing the patterns of interelement relationships. (A) Map presented in figure 18A. Zn is strongly correlated to Fe in Fe-rich grains and in the Fe-rich clay matrix. (B) Map presented in figure 18B. Zn is associated to Fe in Fe-rich grains and to Mn in the manganesiferous spherule.

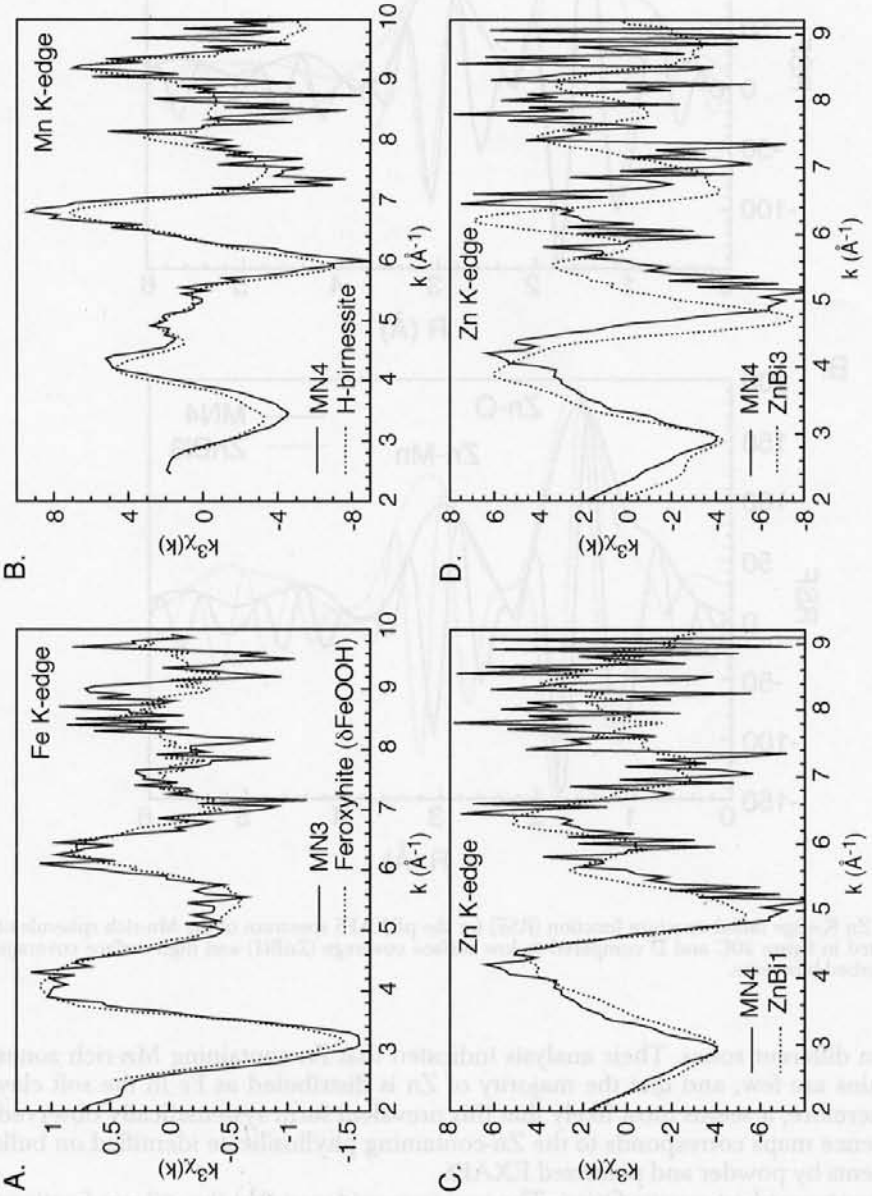

Fig. 20(A) Fe K-edge μEXAFS of a Fe-grain in the map of figure 18A compared to EXAFS spectrum for feroxyhite (δFeOOH). (B) Mn K-edge μEXAFS of the Mn-rich spherule in the map of figure 18B compared to EXAFS spectrum for hexagonal birnessite. (C, D) Zn K-edge μEXAFS recorded in the Zn-richest region of the Mn-rich spherule of MN4 compared to EXAFS spectrum for low surface coverage (ZnBi1) and high surface coverage (ZnBi3) Zn-sorbed birnessite.

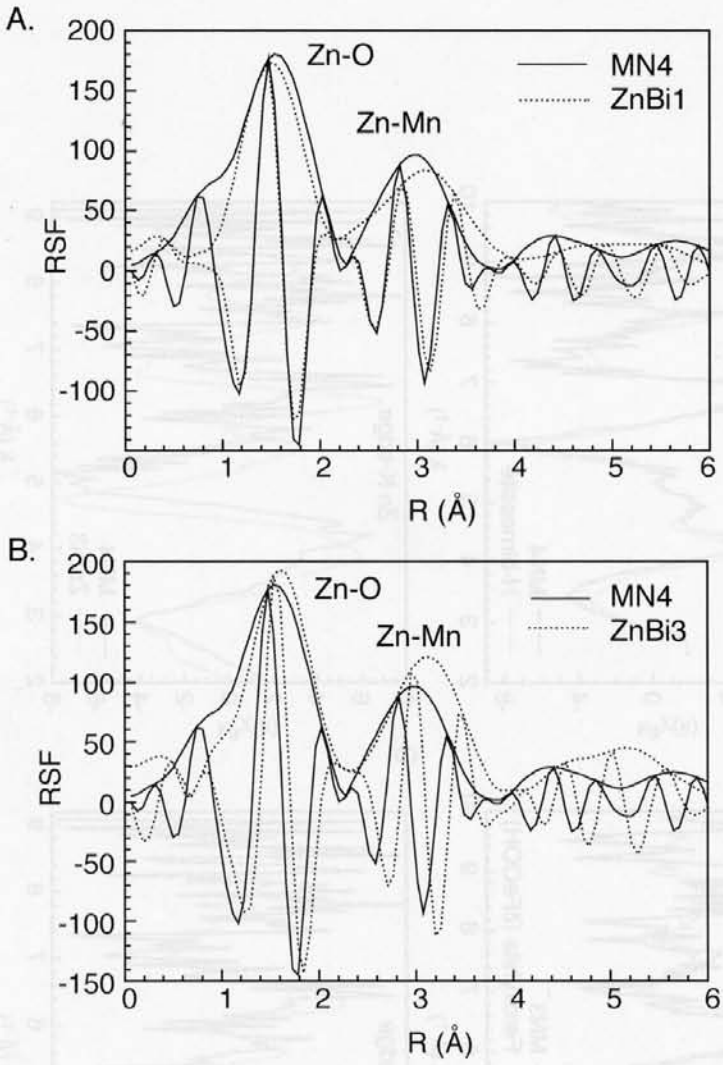

Fig. 21. Zn K-edge radial structure function (RSF) for the μEXAFS spectrum of the Mn-rich spherule of MN4 presented in figure 20C and D compared to low surface coverage (ZnBi1) and high surface coverage (ZnBi3) Zn-sorbed birnessite.

recorded in different zones. Their analysis indicated that Zn-containing Mn-rich zones and Fe-grains are few, and that the majority of Zn is distributed as Fe in the soft clay matrix. Therefore, it seems most likely that this prevalent form systematically observed in fluorescence maps corresponds to the Zn-containing phyllosilicate identified on bulk measurements by powder and polarized EXAFS.

Multicomponent least-squares fitting.–The previous evidence that the <2 μm fractions of soil samples from Mortagne du Nord contain at least three prominent Zn phases justifies the introduction of several components in the least-squares fitting to a linear combination of EXAFS spectra. Including a second component in MN3 < 2 μm improved the fit quality as noted in figure 23A and B (R_p = 63-71) by comparison with fig. 11A and B (R_p = 126-208), but optimal fit between predicted and experimental

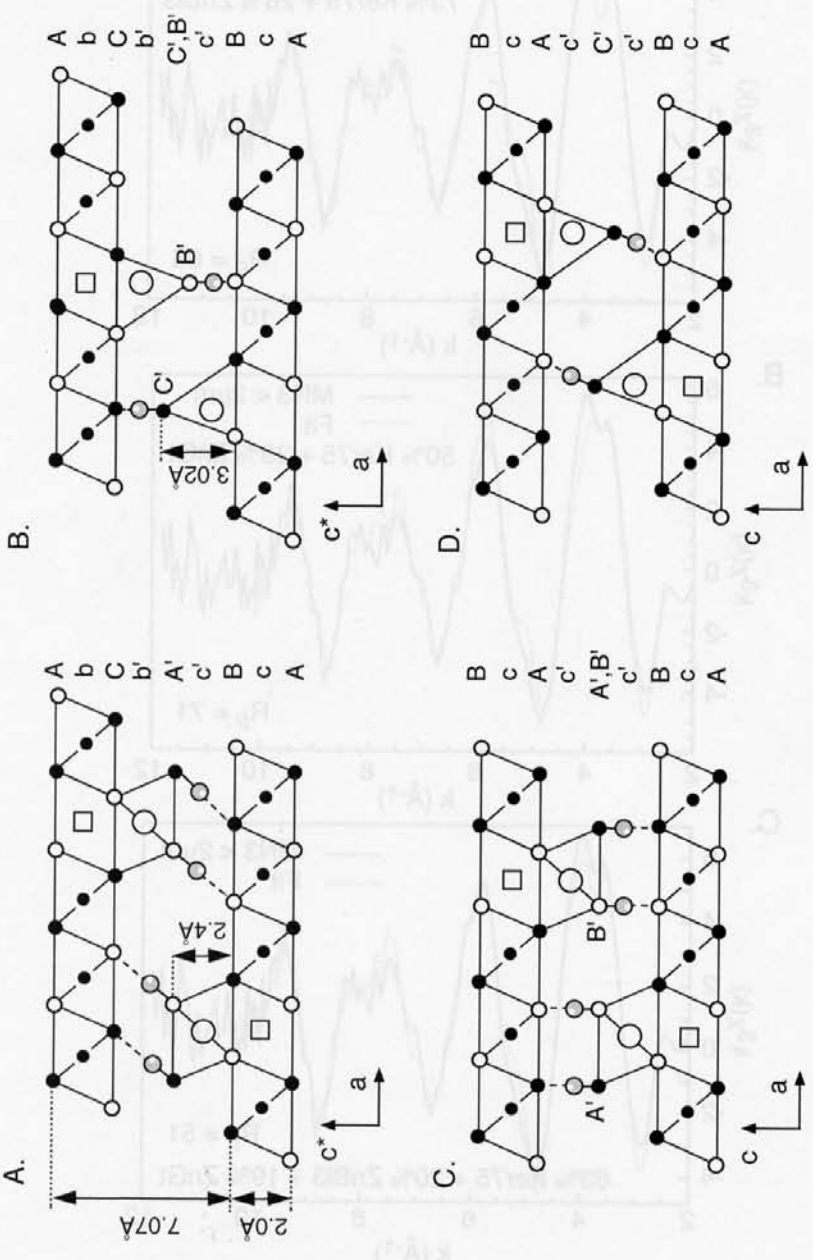

Fig. 22. Theoretical coordinations of interlayer cations in low pH monoclinic or rhombohedral (A, B) and in hexagonal (C, D) birnessite. In (A) and (C) interlayer cations are six-coordinated, and in (B) and (D) they are four-coordinated. Projection of the structures along the b axis. Squares are vacant layer sites. Distances were calculated from data by Lanson and others (2000).

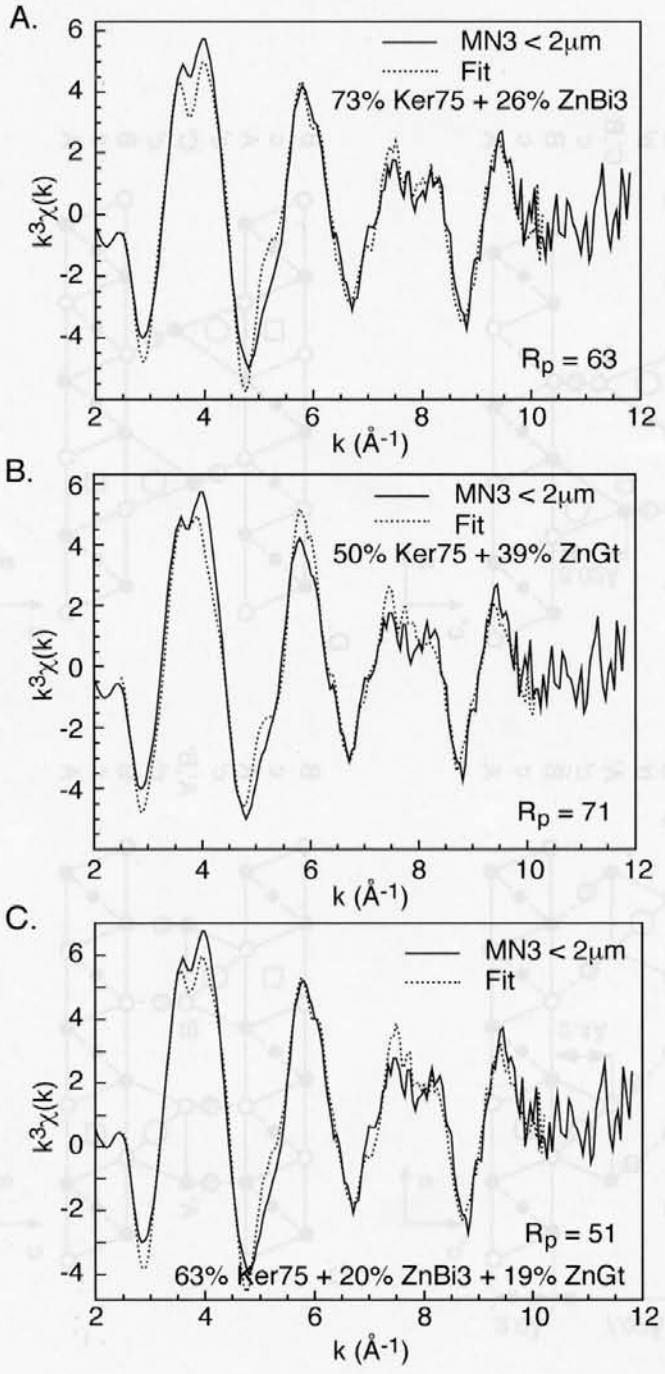

Fig. 23. Two-component model of the EXAFS spectrum for MN3 < 2 μm assuming 73 percent ZnKer75 + 26 percent ZnBi3 (A), and 50 percent ZnKer75 + 39 percent ZnGt (B). (C) Optimal 3-component model of MN3 < 2 μm: 63 percent of ZnKer75 + 20 percent ZnBi3 + 19 percent ZnGt.

spectra ($R_p = 51$) was obtained with the 3-component model: 63 percent phyllosilicate (ZnKer75, $Si_4(Mg_{2.25}Zn_{0.75})O_{10}(OH)_2 \cdot nH_2O$ + 20 percent Zn-sorbed birnessite (ZnBi3) + 19 percent Zn-substituted goethite (ZnGt, $\alpha(Fe_{0.97}Zn_{0.03})OOH$) (fig. 23C). This digital combination provides a good match to the data (fig. 23C), and the introduction of a fourth component would be mathematically unjustified. Surprisingly, the best fit to the experimental spectrum was obtained with ZnBi3 and not ZnBi1, which was detected by μEXAFS. Close examination of least-squares results showed that the hypothesis of a combination of ZnBi1 + ZnKer75 + ZnGt gave a poorer simulation to the data. As expected, including ZnBi1 in a 4-component model slightly improved the fit quality, but the ZnBi1 fraction amounted to only 9 percent of all Zn species, which is below the estimated sensitivity of the method. The assumption of Zn-sorbed goethite instead of Zn-substituted goethite yielded a similar spectral match as the optimal fit, and we believe that comparable fits would have been obtained if other Zn-sorbed Fe (oxyhydr)oxides had been included in the spectral library such as hematite (αFe_2O_3) or feroxyhite ($\delta FeOOH$), which has a defective hematite structure (Drits, Sakharov, and Manceau, 1993). Clearly, the method does not allow differentiation between the various Zn-bearing Fe (oxyhydr)oxide minerals in linear combinations of standard spectra. Therefore, the combination of powder and polarized EXAFS and of μSXRF and μEXAFS results leads to the conclusion that, in MN3 < 2 μm, more than half Zn is present as a phyllosilicate, and the remainder is about equally distributed between birnessite and Fe (oxyhydr)oxide. Given the strong spectral similarity noted previously between MN3 < 2 μm and all the other clay fractions (MN2, MN4, MN6), this conclusion stands for all soil samples from Mortagne du Nord.

Speciation of Zn in the soil from Evin-Malmaison

The Zn concentration of samples E1 ($\phi < 50$ μm) and E2 ($\phi < 2$ μm) amounts to 2318 mg kg^{-1} and 3816 mg kg^{-1}, respectively. Quartz, K- and Ca-feldspars, calcite, goethite, lepidocrocite, kaolinite, illite, and vermiculite were identified by XRD, with quartz being strongly predominant. No Zn-bearing mineral was detected by XRD. Zn K-EXAFS spectra of E1 and E2, on one hand, and of H_2O_2-treated and H_2O_2-untreated samples, on the other hand, are essentially identical (Hargé, 1997) and noticeably resemble the clay fractions from Mortagne du Nord (fig. 24A). Some substantial differences are however observed on the first and third oscillations. The first oscillation is split at 3.5 to 4 $Å^{-1}$ in the two spectra, but the relative intensity of the two maxima is reversed (see arrow). Also, the oscillation at 8 $Å^{-1}$ is asymmetric peaking at 7.5 $Å^{-1}$ in the soil from Evin-Malmaison, whereas it is symmetric in MN3 (see arrow). Figure 24B shows that these two spectral differences can be essentially explained by increasing the proportion of the Zn-containing goethite component in the calculated EXAFS spectrum. A good fit between the predicted and experimental spectra was obtained by assuming 42 percent $\alpha(Fe_{0.97}Zn_{0.03})OOH$ + 68 percent $Si_4(Mg_{2.4}Zn_{0.6})O_{10}(OH)_2 \cdot nH_2O$ (ZnKer60). The quality of the fit was slightly improved with ≥3 components, but each additional component made up less than 10 percent, and, therefore, the presence of these minor phases remains uncertain even though it is beyond doubt that minor Zn species also exist besides the two identified major species.

The existence of a zinciferous phyllosilicate was confirmed by polarization measurements. P-EXAFS spectra of E2 exhibit remarkable differences in the parallel and perpendicular orientation indicating that the average local structure of Zn is anisotropic (fig. 15C). Of particular significance is the change in phase of the second oscillation upon polarization. The observed modification does not correspond to a simple phase shift but, more interestingly, to a displacement in opposite direction of the ascending and descending part of the wave oscillation from $\alpha = 0°$ to 90° (see arrows). The same phenomenon is observed in Zn-sorbed hectorite by canceling the contribution from the octahedral sheet and selecting that from the tetrahedral sheet at $\alpha = 90°$ (fig. 16D). The

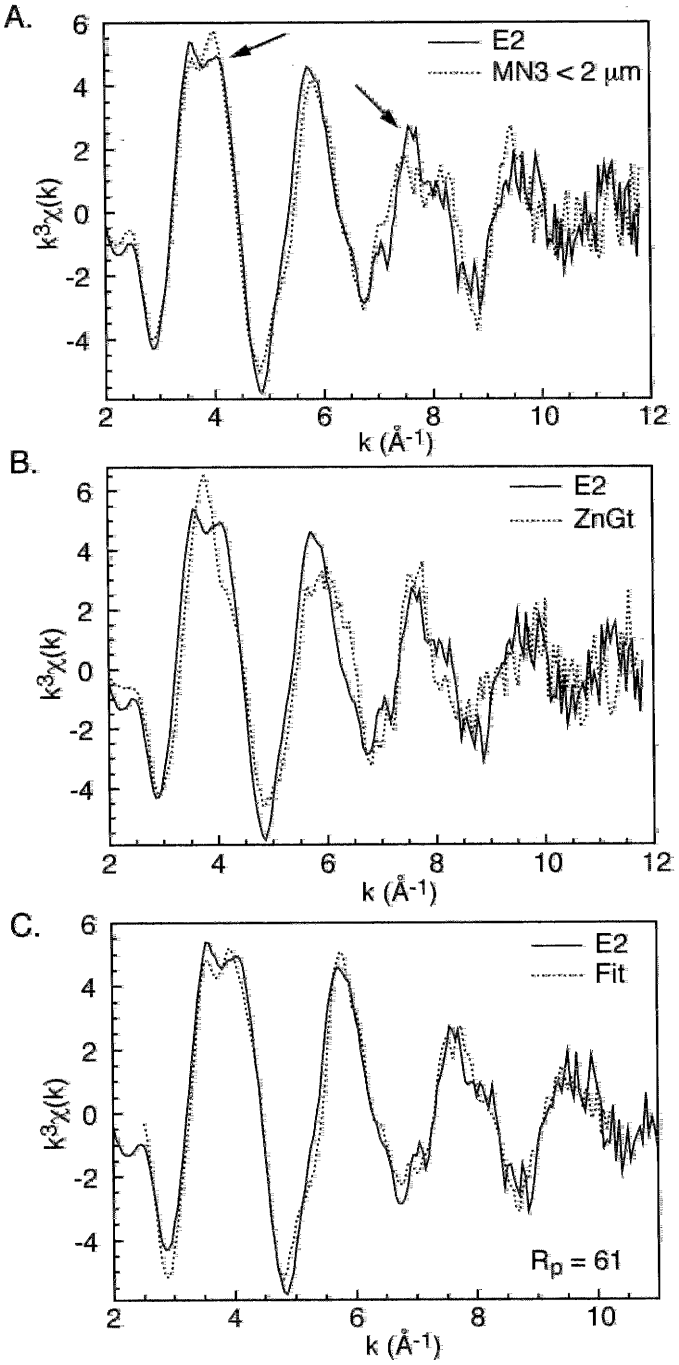

Fig. 24(A) Zn K-edge EXAFS of the clay fraction for the soil from Evin-Malmaison (E2) compared to MN3 < 2 µm (A) and Zn-substituted goethite (ZnGt) (B). (C) Optimal 2-component model of E2: 42 percent ZnGt + 68 percent ZnKer60 ($Si_4(Mg_{2.40}Zn_{0.60})O_{10}(OH)_2 \cdot nH_2O$).

only substantial difference between hectorite and E2 is that the second oscillation of hectorite becomes split whereas the shoulder at ~5.0 $Å^{-1}$ in E2 is solely reinforced at $\alpha = 90°$. This loss of dichroicity results from the admixture of the Fe (oxyhydr)oxide component, which has a featureless and angular independent second oscillation (fig. 24B). This unique angular dependence of the clay fraction from Evin-Malmaison offers strong evidence that Zn is principally bound to phyllosilicates and Fe (oxyhydr)oxides. E2 and MN6 films have essentially the same texture strength (fig. 14B and C) and also contain approximately the same proportion of Zn-phyllosilicate. Therefore, the higher angular dependence for the wave frequency in E2 than in MN6 is unexpected. The fact that E2 contains only two predominant Zn species whereas the sample from Mortagne du Nord has three offers a viable explanation to the observed increase of pleochroicity in E2. Indeed, each metal species bound to an isotropic phase has a peculiar electronic wave function which adds to the anisotropic signal from clay species, and, therefore, the greater the number of isotropic EXAFS contributions, the lower the pleochroicity of the total EXAFS signal.

Speciation of Zn in the soil from Maatheide

The <2 mm fraction (M1) contains 12075 mg kg^{-1} Zn, and the <40 μm fraction (M2) contains 59220 mg kg^{-1} Zn. Chemical treatments and analyses showed that Zn is uniquely present as inorganic species (Hargé, 1997). XRD analysis of M2 indicated the prominent presence of quartz mixed with illite, kaolinite, albite, microcline, jarosite, magnetite, hematite, and two Zn-bearing minerals, hemimorphite ($Zn_4Si_2O_7(OH)_2 \cdot H_2O$) and willemite ($Zn_2SiO_4$) (fig. 6C). EXAFS spectroscopy was employed to detect the possible presence of other Zn phases unrevealed by X-ray diffraction. The comparison of the M2 EXAFS spectrum with MN3 < 2 μm (fig. 25A), hemimorphite, and willemite (fig. 25B) is particularly insightful. The wave phase of M2 is shifted to higher k values relative to MN3 < 2 μm, being displaced in the direction of hemimorphite and willemite. This observation indicates that M2 contains other Zn-bearing species than those detected by XRD, and we can surmise from the intermediate spectral shape of M2 that Zn is partly associated with phyllosilicates as in the soils from Mortagne du Nord and Evin-Malmaison. The best 3-component model fit was obtained assuming 58 percent ZnKer88 + 16 percent hemimorphite +10 percent willemite ($R_p = 41$). Figure 25C shows that this simulation failed to reproduce correctly the shape of the second oscillation (peaking at 6 $Å^{-1}$), and the relative amplitude of the first (4 $Å^{-1}$) and second oscillations. A satisfactory fit of model predictions to experimental data ($R_p = 31$) was obtained by adding a fourth component, the optimal fit being obtained for 47 percent ZnKer73 + 14 percent hemimorphite + 12 percent willemite + 12 percent ZnBi3 (fig. 25D).

DISCUSSION

Structure and formation of Zn-containing phyllosilicates

This study provides direct structural evidence for the uptake of Zn by phyllosilicates in contaminated soils. In the following the questions of the structure and formation mechanism of this major Zn species will be successively addressed. Determining the average chemical composition of Zn phyllosilicates is beyond the possibilities of EXAFS, because it is a local structural probe, and, in addition, it is unable to distinguish Al from Mg and Zn from Fe backscatterers. But the dioctahedral versus trioctahedral nature of the Zn-containing phyllosilicate can be discussed. All M1 and M2 octahedral positions are occupied in trioctahedral phyllosilicates, but only 2/3 in dioctahedral structures (fig. 4). Octahedral cations are surrounded ideally by six divalent cations (6 Oct) in the former group of minerals and three trivalent cations (3 Oct) in the latter, and, conse-

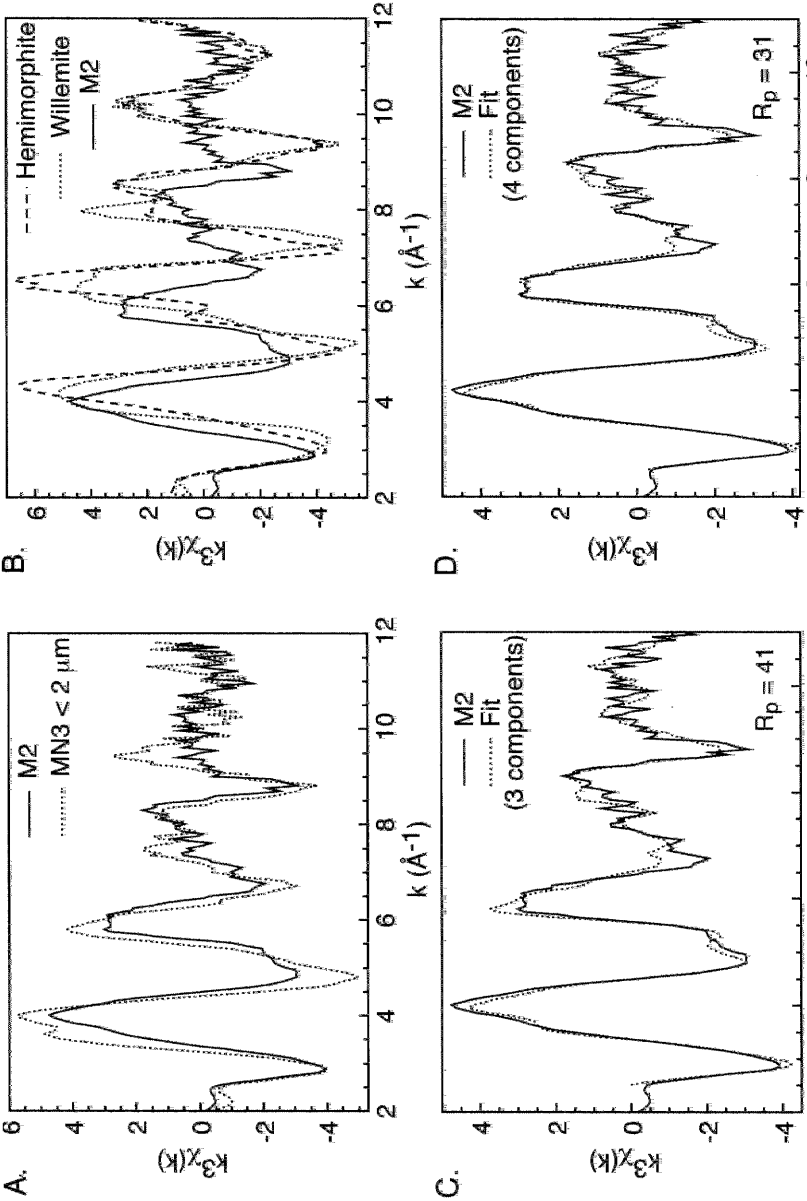

Fig. 25. Zn K-edge EXAFS of the clay fraction from Maatheide (M2) compared to MN3 < 2 μm (A), and willemite and hemimorphite (B). (C) 3-component model of M2 assuming 58 percent ZnKer88 + 16 percent hemimorphite + 10 percent willemite. (D) 4-component model of M2: 47 percent ZnKer73 + 14 percent hemimorphite + 12 percent willemite + 12 percent ZnBi3.

quently, these minerals should have distinctly different second RSF peak magnitudes, allowing their differentiation. In fact, dioctahedral and trioctahedral structures cannot be distinguished by this method because electronic waves backscattered by "light" elements (Mg, Al) and 3d transition elements (Fe, Zn) are shifted out of phase by π (Teo, 1986). Consequently, a 3 (Fe, Zn) dioctahedral environment is equivalent to a 4 (Fe, Zn) + 2 Mg trioctahedral environment because the contribution of the two Mg atoms cancels the contribution of one (Fe, Zn) (Mg has about half as many electrons as Fe/Zn so that its wave amplitude is halved) (Manceau, Schlegel, and others, 1999). Likewise, a 3 (Al, Mg) local environment is equivalent to 5 (Al, Mg) + 1 (Fe, Zn). It happens that similar spectral fits would have been obtained by using a series of dioctahedral Zn-containing smectites instead of kerolites since a dioctahedral phyllosilicate with the generic formula $Si_4[(Al, Mg)_{8/3-x}](Fe, Zn)_{x\cdot 2/3}]ExO_{10}(OH)_2$ would provide ideally the same spectral fit as $(Si_4(Mg_{3-x}Zn_x)O_{10}(OH)_2)$. Therefore, the analysis of the second shell contribution in EXAFS spectra of soil samples cannot be used to determine unambiguously the dioctahedral versus trioctahedral character of Zn phyllosilicates. Another complication comes from ancillary Zn species (Mn oxide and Fe (oxyhydr)oxides) whose 2nd shell contributions overlap that of the phyllosilicate.

This question of the dioctahedral versus trioctahedral nature of Zn phyllosilicates in soils can be sensibly addressed by examining atomic pair correlation in the 4.0 to 4.5 Å distance range (Manceau, Chateigner, and Gates, 1998). Trioctahedral phyllosilicates have a flat and dioctahedral phyllosilicates a corrugated tetrahedral basal surface due to the downward displacement of basal oxygens (O_b) located above vacant octahedral sites (fig. 13E and F) (Lee and Guggenheim, 1981; Kuwahara, 1999). Thus Oct-O_b distances are coherent in trioctahedral structures ($R \approx 4.15$-4.20 Å), and this atomic pair shows up on the RSF at $R + \Delta R \approx 3.8$ Å near the Oct-2nd Si contribution at $R + \Delta R \approx 4.2$ Å (fig. 16 in Manceau, Chateigner, and Gates, 1998). In dioctahedral structures Oct-O_b distances are split causing the disappearance of this contribution. The fact that soil samples, and namely NM3 < 2 µm in figure 12, exhibit a marked third RSF peak (D) at $R + \Delta R \approx 3.8$ Å, and that the imaginary part of this contribution is precisely in phase with the trioctahedral reference kerolite, strongly supports a trioctahedral local environment for Zn. But since EXAFS is a local structural probe, this result does not definitely prove that Zn is actually trapped in (Zn, Mg) trioctahedral clay particles because dioctahedral phyllosilicates can accommodate trioctahedral domains in their structure (Muller and others, 1997).

Another interesting question is the mechanism of Zn immobilization. Following the weathering of primary Zn minerals (franklinite, willemite, hemimorphite) and the subsequent leaching of zinc, does dissolved Zn^{2+} sorb on pre-existing phyllosilicates, or does it precipitate with free silicic acid and other dissolved cationic species to neoform a phyllosilicate? This question can be addressed from structural and thermodynamic points of views. From a structural perspective, Zn sorbed on the edges of hectorite platelets has a similar local environment as if it were substituted for Mg in a phyllosilicate structure (fig. 4). On hectorite borders, sorbed Zn octahedra share ~2 edges with sorbent Mg octahedra, and ~2 corners with sorbent Si tetrahedra. Based on the previous discussion, this local environment is, in fact, quite equivalent from the standpoint of EXAFS to the 1:1 phyllosilicate $Si_2(Mg_{2.35}Zn_{0.65})O_5(OH)_4$ in which diluted Zn species are surrounded by 2 Si from the tetrahedral sheet and 4.7 Mg + 1.3 Zn from the octahedral sheet. Therefore, EXAFS does not provide any clue as to the formation of Zn surface complexes on existing soil phyllosilicates or to the incorporation of Zn into the structure of neoformed phyllosilicates.

From a thermodynamic perspective, the precipitation of Zn-containing phyllosilicate is possible only if Zn is at saturation or oversaturated with a given phyllosilicate

composition. In the case of ZnKer300, the equilibrium between solute Zn and the solid phase can be written:

$$Si_4Zn_3O_{10}(OH)_2 + 6H^+ + 4H_2O \rightarrow 3Zn^{2+} + 4Si(OH)_4$$

To our knowledge the solubility product (K_{ZnKer}) for this reaction has not been determined experimentally. However, K_{ZnKer} can be calculated from the Gibbs free energy of formation of the Zn-phyllosilicate, which in turn can be estimated by the method of Tardy and coworkers (Tardy and Garrels, 1976; Tardy and Garrels, 1977; Tardy and Fritz, 1981; Tardy and Duplay, 1992). According to this method, a linear regression relates the Gibbs free energy of formation of a silicate mineral from its constituent oxides to a parameter designated by $\Delta O^{2-}(Me^{2+})$. For Zn^{2+}:

$$\Delta O^{2-}(Zn^{2+}) = \Delta_f G^o(ZnO_{cryst}) - \Delta_f G^o(Zn^{2+}_{aq})$$

where $\Delta_f G^o(ZnO_{cryst})$ and $\Delta_f G^o(Zn^{2+}_{aq})$ are the Gibbs free energy of formation of crystalline ZnO and aqueous Zn^{2+}, respectively. Decarreau (1985) and Tardy and Duplay (1992) demonstrated that this linear relationship also applies to phyllosilicates. Thus:

$$\Delta_f^{ox}(\text{Me-phyllosilicate}) = A \cdot \Delta O^{2-}(Me^{z+}) + B$$

where Δ_f^{ox}(Me-phyllosilicate) is the Gibbs free energy of formation of an Me-containing phyllosilicate from its constituent oxides. The parameters A and B were calculated from the Gibbs free energy of formation of poorly ordered reference silicates tabulated by Tardy and Duplay (1992) and by using $\Delta O^{2-}(Me^{2+})$ values calculated by Tardy and coworkers (Tardy and Garrels, 1976; Tardy and Garrels, 1977; Tardy and Duplay, 1992). This procedure yielded A = −1.3174, B = −298.5 kJ · mol^{-1}, $\Delta_f^{ox}(ZnKer)$ = −47.2 kJ mol^{-1}. The standard Gibbs free energy of formation of ZnKer calculated from $\Delta_f^{ox}(ZnKer)$ is $\Delta_f G^o(ZnKer)$ = −4682 kJ mol^{-1} (±30 kJ mol^{-1} at the 95.5 percent confidence level). Using classical thermodynamics (Sposito, 1994) and thermochemical values reported elsewhere (Tardy and Duplay, 1992; Manceau, Schlegel, Nagy, and Charlet, 1999), the following solubility product is obtained:

$$\text{Log } (K_{ZnKer}) = 8 \pm 6.$$

The stability of ZnKer300 in soils can now be assessed by determining the solubility (that is, the saturation concentration) of Zn^{2+} with respect to ZnKer300 (fig. 26). The plots presented in figure 26 indicate that the solubility of ZnKer300 decreases with increasing pH up to pH 9 and with increasing concentration of dissolved silica. The next step of this thermodynamic analysis consists in placing results from water analyses of contaminated soils in the $[Zn]_{aq}$ = f(pH) equilibrium diagram of figure 26 in order to evaluate the saturation state of percolating waters with respect to zinciferous phyllosilicates. In the grassland of Mortagne du Nord, the concentration of Zn^{2+}_{aq} and silicic acid averages 10 ppm and 10 to 20 ppm, respectively, and pH values range from 6.5 to 7.5 (Cambier, 1998). Percolating waters of a soil near Evin-Malmaison were analyzed after filtration to <5 μm and ultracentrifugation tc remove colloids (Douay, Semlali, and Denaix, 1997). The concentrations of dissolved Si and Zn varied between 6 to 13 ppm, and 7 to 23 ppm, respectively, and soil pHs between 5.6 in surface and 6.7 in deep soil. It is interesting to note that the concentration of $Si(OH)_4$ in waters determined by Cambier (1998) and by Douay (1997) was quite systematically at saturation with respect to quartz solubility (11 ppm, Rimstidt, 1997) and undersaturated relative to amorphous silica (116 ppm, Rimstidt and Barnes, 1980). These results are consistent with the worldwide homeostasis of the silicic acid concentration in terrestrial waters, which is typically between 10 and 80 ppm (Davies and DeWiest, 1966). Examination of figure 26 shows that all soil solutions are supersaturated or near saturation with respect to a purely trioctahedral Zn phyllosili-

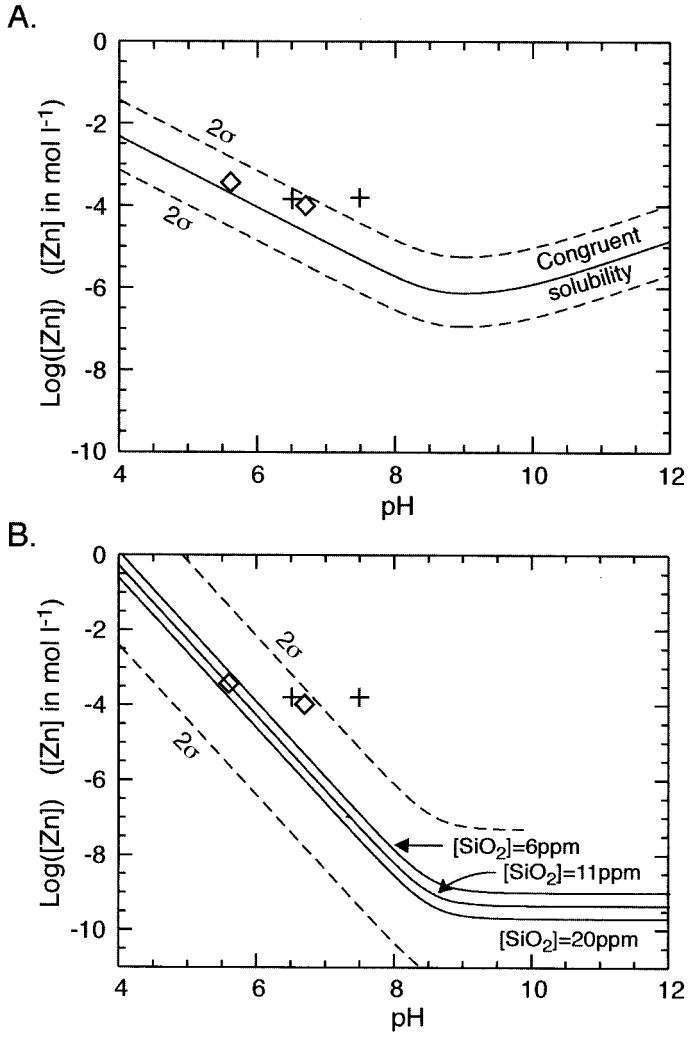

Fig. 26. Saturation concentration of dissolved Zn with respect to Zn-rich kerolite (ZnKer). $[Si(OH)_4]$ controlled by congruent solubility of ZnKer (A) and by quartz/amorphous silica solubility, $[Si(OH)_4]$ = 6, 11, 20 ppm (B). Dashed lines show the uncertainty on the saturation concentration of Zn resulting from the uncertainty on K_{ZnKer} at the 95.5 percent confidence level. Crosses refer to chemical analyses of soil solutions from Mortagne du Nord ([Zn] = 10 ppm, Cambier, 1998) and diamonds to chemical analyses from the soil solutions near Evin-Malmaison analyzed by Douay (1997) (pH = 5.6 and [Zn] = 23 ppm in upper horizon, and pH = 6.7 and [Zn] = 7 ppm in lower horizon). All soil solutions are supersaturated or near saturation with respect to a pure ZnKer phase.

cate. The solubility product of Zn-Mg kerolites is not known, but it is certainly lower than that of the pure Zn endmember (ZnKer300); otherwise the synthesis of mixed Zn-Mg solids would not have been possible, that is, Zn would not have mixed with Mg at the atomic scale. The same line of reasoning can be applied to natural Zn phyllosilicates. Neither their precise chemical composition nor solubility products are known, but any Mg, Al, Mg, Zn phyllosilicate should be less soluble than ZnKer300 and should form in its place. Consequently, the reported solution compositions clearly support the interpretation of Zn-phyllosilicate formation as determined from EXAFS spectroscopy.

The combination of chemical analyses and EXAFS results indicates that Zn is predominantly bound to phyllosilicates in deep soil horizons at Mortagne du Nord. Two processes can be envisaged to explain this strong Zn partitioning: (1) a gravitational migration of Zn particles formed in upper horizons and (2) a migration of dissolved Zn^{2+} and its subsequent precipitation with silic acid or uptake on phyllosilicates in deep soil. Two arguments attest for the existence of a physical transport of fine particles. First, carbon, willemite, and franklinite particles, originally contained in the MN1 slag horizon, have been observed in thin sections of deeper horizons and were also detected in dense fractions by XRD. Second, colloidal phyllosilicate particles have been collected by ultracentrifugation in percolating water at the bottom of a soil profile near Evin-Malmaison (Douay, Semlali, and Denaix, 1997). The dark silty upper horizon (MN1) could act as a source for migrating Zn particles. However, the absence of clay coating on the rims of soil micropores as observed by optical microscopy and the presence of Zn in the clay matrix of deeper horizons suggest that Zn also partly migrates downward as dissolved free ion or small complexes. Consequently, phyllosilicate neoformation in deep soils cannot be discounted, and the two contemplated Zn migration mechanisms probably coexist.

Re-examination of the (Zn, Al) hydrotalcite-like model proposed by Julliot (1999)

Inter-elemental analyses by μSXRF indicated that Zn is partly or totally correlated to Fe and Mn in the ferruginous clayey matrix of soils from Mortagne du Nord, and this tight chemical association observed at the micron scale is consistent with the atomic scale association of Zn to clay minerals (soil phyllosilicates generally have Fe in their structure), Fe (oxyhydr)oxides, and Mn oxides determined by bulk EXAFS, μEXAFS and P-EXAFS. Similar (Zn, Pb)-Fe and (Zn, Pb)-Mn correlations were reported by Juillot (1999) in an independent study realized on a wooded and a tilled soil sampled in the vicinity of the smelter at Evin-Malmaison (fig. 27). The resemblance of the correlation diagrams reported by these authors to those obtained in the present study (fig. 19A and B) is compelling and suggests that Zn and Pb are essentially bound to the same soil minerals. The inorganic fraction of Pb effectively was shown to be taken up by birnessite and goethite, thus accounting for the observed Pb-Fe and Pb-Mn correlation (Juillot, 1999; Morin and others, 1999). However, a different structural interpretation was proposed for the speciation of Zn by Juillot and others (Juillot, 1999). They concluded that almost 100 percent of Zn is speciated as mixed-Zn/Al hydroxides (hydrotalcite-like structure) in the <2 μm fraction of the tilled soil, and as a mixture of 62 percent mixed-Zn/Al hydroxides + 38 percent exchangeable Zn (presumably organically bound) in the <2 μm fraction of the wooded soil. Figure 28A and B compare the EXAFS spectra reported by Juillot (1999) for the clay fractions of the untreated tilled soil and the Ca-exchanged (Zn-organic free) wooded soil to the proposed hydrotalcite-like model. A glance at this figure immediately shows that the proposed double-hydroxide Zn species only crudely mirrors the shape of the two soil spectra. The model and unknown spectra do not have the same wave frequency between 6 and 9 $Å^{-1}$, and their second oscillation maxima are shifted. This simple comparison indicates that Zn is not uniquely, if at all, speciated as hydrotalcite and therefore prompts a re-examination of the proposed structural interpretation. In addition, this interpretation conflicts with the Zn-Mn correlation observed by μSRXF.

To clarify this incongruity and refine the speciation of Zn in these two soil samples, EXAFS spectra obtained by Juillot (1999) were carefully digitized and reanalyzed by the linear fitting procedure to known mixtures of Zn model compounds. The sum of components was scaled to 100 percent due to the poor precision of the y scale in the source spectra. A minimum of three spectral components proved necessary to reproduce both the phase and shape of the two soil spectra. For the tilled soil, three mathematical solutions gave similar results. In all of them a Zn-phyllosilicate ($Si_4(Mg_{1.1}Zn_{1.9})$

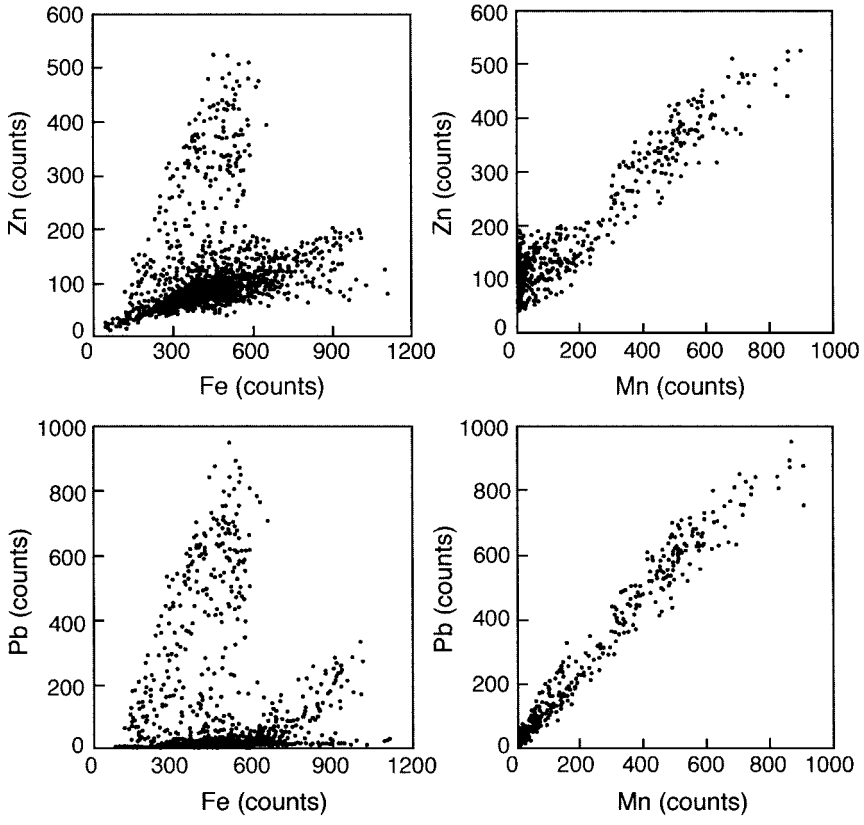

Fig. 27. Zn-Fe, Zn-Mn, Pb-Fe, and Pb-Mn correlations from SXRF maps in the wooded soil from Evin-Malmaison studied by Juillot (1999). Zn and Pb points correlated to Mn correspond to Zn,Pb sorbed on Mn oxides. Zn and Pb points correlated to Fe correspond to Zn,Pb associated to the ferruginous clay matrix.

$O_{10}(OH)_2 \cdot nH_2O$) and the ZnBi3 reference systematically showed up in similar proportions (56-65 percent and 21-26 percent, respectively). The presence of these two major species is therefore very likely (fig. 28C). The assumptions of ZnBi1, ZnGt, or ZnFh22 as the third component could not be statistically distinguished because their contributions were too weak (14-18 percent); therefore the nature of the third Zn component is less conclusive. The fit of the wooded soil was more robust, and all acceptable solutions systematically contained, in decreasing order of prevalence, a Zn-phyllosilicate, a Zn-sorbed birnessite, and a Zn-containing (either sorbed or substituted) Fe (oxyhydro)oxide. The best statistical solution was obtained for 43 percent (Zn, Mg)-kerolite ($Si_4(Mg_{0.6}Zn_{2.4})$ $O_{10}(OH)_2 \cdot nH_2O$) + 37 percent ZnBi3 + 23 percent ZnFh22, but satisfying solutions were also obtained with ZnBi1, ZnGt, and slightly different phyllosilicate compositions (fig. 28D). Zn-containing magnetite ($[Fe, Zn]Fe_2O_4$) and, to a lesser amount ZnS, were identified in the dense ($d > 2.9$) and 50 to 200 µm fractions of the two soils by the complement of XRD and EXAFS (Juillot, 1999). These two high temperature minerals probably originated from atmospheric dust falls, and they likely act as the main source of Zn in contaminated soils around the smelter. While the existence of minor Fe-(oxyhydr)oxide species in the tilled soil remains somewhat tentative, this hypothesis is however consistent with Zn-containing magnetite ($[Fe,Zn]Fe_2O_4$) as a primary source of Zn released during the weathering of the spinel. Also, Juillot (1999) found that the

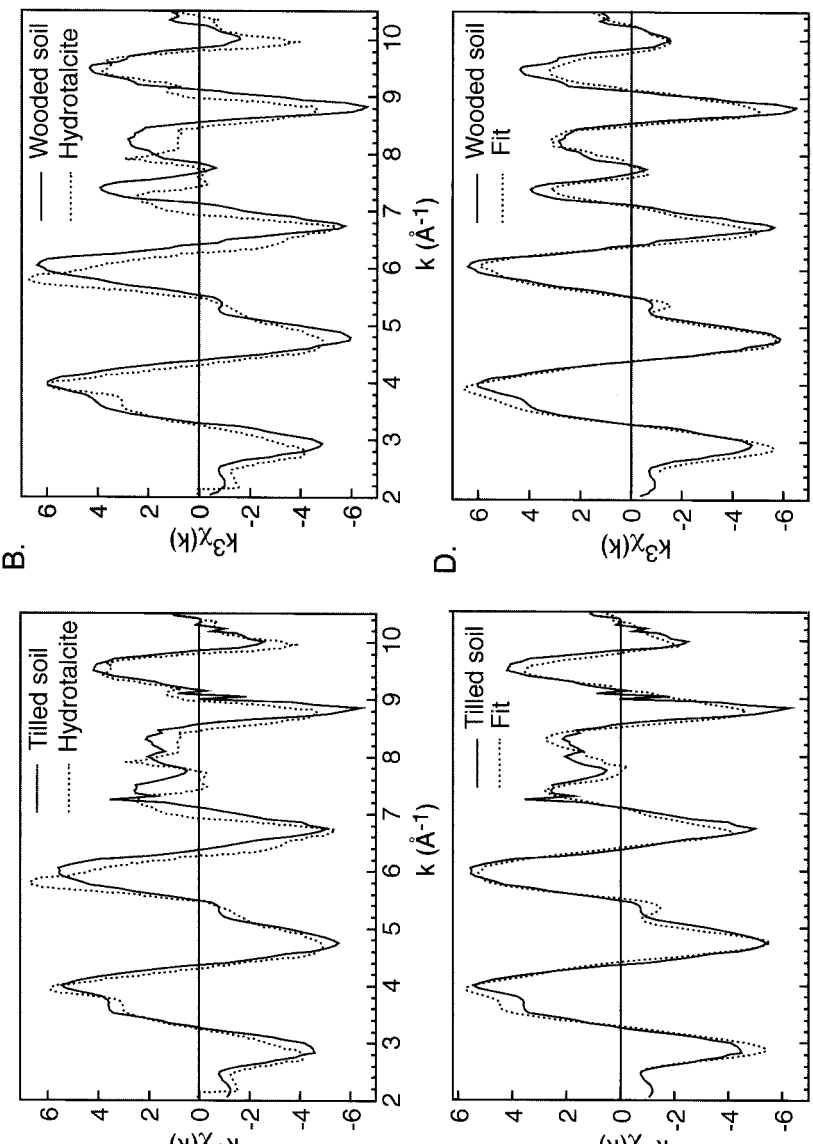

Fig. 28. Zn K-edge EXAFS for the untreated tilled topsoil <2 μm fraction (A) and the $CaCl_2$-treated wooded topsoil <2 μm fraction (B) compared to (Zn, Al)-hydrotalcite. (C) 3-component model: 56–65 percent ZnKer190 + 21–26 percent ZnBi3 + 14–18 percent of ZnBi1/ZnGt/ZnFh22. The third component is weak, and the nature of the inferred phase is thus less conclusive. (D) Optimal 3-component model: 43 percent ZnKer240 + 37 percent ZnBi3 + 23 percent ZnFh22.

wooded soil contained higher amounts of Zn-magnetite, and this finding is again entirely consistent with the higher proportion of Zn-(oxyhydr)oxide secondary products determined in our reanalysis of Juillot's EXAFS spectra.

The main conclusion from this section is that the hydrotalcite-like Zn species, which was suggested as being the unique (tilled soil) or predominant (wooded soil) neoformed Zn species in contaminated soils near Evin-Malmaison, is not supported by EXAFS. EXAFS results are instead consistent with the uptake of zinc by a phyllosilicate, a birnessite-like phyllomanganate, and one or several Fe (oxyhydr)oxides. This new interpretation also demonstrates the great advantage of applying an unprecedented array of standard techniques and novel spectroscopic applications. The close agreement from the techniques applied provides a firm identification of these three Zn species in our soil samples (MN and E) collected in the same geographical area as those studied by Juillot (1999). Lastly, an indirect argument in support of the preferred formation of Zn phyllosilicates over hydrotalcite is that in soils and sediments finely divided quartz is often coated by clay minerals. Hydrotalcite compounds are stable in alkaline conditions and they are extremely rare, if previously identified at all, in oxidizing soil horizons with acidic (5.5 for the wooded soil) to neutral (7.5 for the tilled soil) pH. The neoformation of a non-silicated Zn/Al mixed hydroxide, (1) at acidic to neutral pH, (2) in the presence of high amounts of quartz and phyllosilicates, and (3) in soil solutions saturated with silicic acid, is thermodynamically unrealistic.

CONCLUSIONS

The transport and fate of trace elements in soils are largely controlled by their distribution between aqueous and mineral phases. Knowledge of uptake mechanisms of trace elements by soil constituents is therefore a key issue for evaluating their mobility and bioavailability. Among the wealth of soil inorganic constituents, phyllosilicates, Fe (oxyhydr)oxides, and Mn oxides possess unique sorption properties and are widely recognized as being three of the most important sinks for trace metals in soils. However, determining the molecular-scale uptake mechanisms of metals in unperturbed soils still remains challenging partly due to the intimate mixture of these three constituents since oxide minerals occur as minute discrete particles or as coatings on other mineral surfaces, such as quartz or phyllosilicates. In this study, we showed that these three phases actually act as the three predominant sinks of Zn in a variety of soils contaminated by smelting processes, and the molecular-mechanism of the Zn uptake was identified in several cases. Successful identification of these three Zn species is due to the combination of three factors: (1) the synthesis of appropriate Zn-containing references relevant to soil minerals and that mimicked some of the principal soil sorption processes, (2) the first application of polarized EXAFS and texture goniometry to fine-grained and multiphase soil clay fractions, and (3) the in situ micro-mineralogical investigation of soils by coupled μSXRF and μEXAFS, which allowed us directly to distinguish and identify two of the three major Zn pools. This study heavily relies on recent synchrotron-based capabilities developed on the 3rd generation synchrotron facilities of the ESRF in Grenoble and the ALS in Berkeley, and these advanced light sources clearly open up unprecedented possibilities for understanding the speciation of trace elements in the mineral fraction of soils.

ACKNOWLEDGMENTS

The authors acknowledge the two anonymous reviewers and the anonymous associate editor for their valuable comments. Y. Soldo, J. J. Menthonnex, and O. Ulrich are commended for their assistance in the collection of EXAFS spectra on BM32 at the European Synchrotron Radiation Facility (ESRF), and A. MacDowell, R. Celestre and H. Padmore for the design and continuing development of the microfocusing

beamline 10.3.2 at the Advanced Light Source (ALS). The samples from Maatheide were kindly supplied by J. Vangronsveld. We are grateful to the ESRF at Grenoble and the ALS at the Lawrence Berkeley National Laboratory for the provision of beamtime. This work was supported by the SRAE division of the French Ministry of Environment (MATE), and the Director, Office of Energy Research, Office of Basic Energy Sciences, Materials Sciences Division of the U.S. Department of Energy, under Contract no. DE-AC03-76SF00098.

References

Arcon, I., Mirtic, B., and Kodre, A., 1998, Determination of valence states of chromium in calcium chromates by using X-ray absorption near-edge structure (XANES) spectroscopy: Journal of the American Ceramic Society, v. 81, p. 222–224.

Baes, C. F., and Mesmer, R. E., 1976, The hydrolysis of cations: New York, John Wiley & Sons, 489 p.

Baize, D., 1997, Teneurs totales en éléments traces métalliques dans les sols: Paris, Institut National de la Recherche Agronomique (INRA) Editions, 408 p.

Bajt, S., Sutton, S. R., and Delaney, J. S., 1994, Microanalysis of iron oxidation states in silicates and oxides using X-ray absorption near edge structure (XANES): Geochimica et Cosmochimica Acta, v. 58, p. 5209–5214.

Bermond, A., 1992, Thermodynamics applied to the study of the limits of sequential extraction procedures used for the speciation of trace elements in sediments and soils: Environment and Technology, v. 13, p. 1175–1179.

Bertsch, P. M., Hunter, D. B., Sutton, S. R., Bajt, S. R., and Rivers, M. L., 1994, In situ chemical speciation of uranium in soils and sediments by micro X-ray absorption spectroscopy: Environmental Science and Technology, v. 28, p. 980–984.

Brindley, G. W., and Brown, G., 1980, Crystal structures of clay minerals and their X-ray identification: London, Mineralogical Society, 495 p.

Cambier, P., 1998, Mise au point de méthodes d'évaluation des risques liés à la contamination de terrains par des éléments toxiques: French Ministry of Environment, Service de la Recherche et des Affaires Economiques (SRAE) Report 94-042, 76 p.

Charlatchka, R., and Cambier, P., 1999, Influence of reducing conditions on solubility of trace metals in contaminated soils: Water, Air, and Soil Pollution, v. 113, p. 1–26.

Cornell, R. M., and Schwertmann, U., 1996, The iron oxides: Weinheim, Germany, VCH verlag, 573 p.

Cotter-Howells, J. D., Champness, P. E., Charnock, J. M., and Pattrick, R. A. D., 1994, Identification of pyromorphite in mine-waste contaminated soils by ATEM and EXAFS: European Journal of Soil Science, v. 45, p. 393–402.

Das, A. K., Chakraborty, R., Cervera, M. L., and Delaguardia, M., 1995, Metal speciation in solid matrices: Talanta, v. 42, p. 1007–1030.

Davidson, C. M., Thomas, R. P., Mcvey, S. E., Perala, R., Littlejohn, D., and Ure, A. M., 1994, Evaluation of a sequential extraction procedure for the speciation of heavy metals in sediments: Analytica Chimica Acta, v. 291, p. 277–286.

Davies, S. N., and DeWiest, R. C. M., 1966, Hydrogeology: New York, John Wiley & Sons, 463 p.

Decarreau, A., 1985, Partitioning of divalent transition elements between octahedral sheets of trioctahedral smectites and water: Geochimica et Cosmochimica Acta, v. 49, p. 1537–1544.

Dietrich, K. N., Berger, O. G., Succop, P. A., Hammond, P. B., and Bornscheim, R. L., 1993, The developmental consequences of low to moderate prenatal and postnatal lead exposure-Intellectual attainment in the Cincinnati lead study cohort following school entry: Neurotoxicology Teratology, v. 15, p. 37–44.

Douay, F., Semlali, M. R., and Denaix, L., 1997, Etude d'un secteur pollué par les métaux, Transfert des métaux dans les sols: Conseil Régional Nord-Pas de Calais Report, 39 p.

Douglas, B., McDaniel, D., and Alexander, J., 1994, Concepts and models of inorganic chemistry: New York, John Wiley & Sons, 928 p.

Drits, V. A., Sakharov, B. A., and Manceau, A., 1993, Structure of feroxyhite as determined by simulation of X-ray diffraction curves: Clay Minerals, p. 209–222.

Duff, M. C., Hunter, D. B., Triay, I. R., Bertsch, P. M., Reed, D. T., Sutton, S. R., Shea-McCarthy, G., Kitten, J., Eng, P., Chipera, S. J., and Vaniman, D. T., 1999a, Mineral associations and average oxidation states of sorbed Pu on tuff; Journal of Environmental Science Technology, v. 33, 2163–2169.

Duff, M. C., Newville, M., Hunter, D. B., Bertsch, P. M., Sutton, S. R., Triay, I. R., Vaniman, D. T., Eng, P., and Rivers, M. L., 1999b, Micro-XAS studies with sorbed plutonium on tuff: Journal of Synchrotron Radiation, v. 6, p. 350–352.

Dyar, M. D., Delaney, J. S., Sutton, S. R., and Schaefer, W., 1998, Fe^{3+} distribution in oxidized olivine: A synchrotron micro-XANES study: American Mineralogist, v. 83, p. 1361–1365.

Ernhart, C. B., 1992, A critical review of low-level prenatal lead exposure in the human: 2. effects on the developing child: Reproductive Toxicology, v. 6, p. 21–40.

Fergusson, J. E., 1990, The heavy elements: Chemistry, environmental impact and health effects: Pergamon Press, 614 p.

Förstner, U., 1993, Metalspeciation–general concepts and applications: International Journal of Environmental Analytical Chemistry, v. 51, p. 5–23.

Foster, A. L., Brown, G. E., Parks, G. A., Tingle, T. N., Voigt, D. E., and Brantley, S. L., 1997, XAFS determination of As(V) associated with Fe(III) oxyhydroxides in weathered mine tailings and contaminated soil from California, USA: Journal de Physique IV, v. 7, p. 815–816.

Ghose, S., 1964, The crystal structure of hydrozincite, $Zn_5(OH)_6(CO_3)_2$: Acta Crystallographica, v. 17, p. 1051–1057.

Godin, P., Feinberg, M., and Ducauze, C., 1985, Modelling of soil contamination by airborne lead and cadmium around several emission sources: Environmental Pollution Series, v. B10, p. 97–114.

Hargé, J. C., ms, 1997, Spéciation comparé du zinc, du plomb et du manganèse dans des sols contaminés: Ph.D. thesis, University Joseph Fourier, Grenoble, France.

Heald, S. M., Brewe, D. L., Stern, E. A., Kim, K. H., Brown, F. C., Jiang, D. T., Crozier, E. D., and Gordon, R. A., 1999, XAFS and micro-XAFS at the PNC-CAT beamlines,: Journal of Synchrotron Radiation, 6, 347–349.

Heald, S. M., and Stern, E. A., 1977, Anisotropic x-ray absorption in layered compounds: Physical Review, v. B16, p. 5549–5559.

Hunter, D. B., Bertsch, P. M., Kemner, K. M., and Clark, S. B., 1997, Distribution and chemical speciation of metals and metalloids in biota collected from contaminated environments by spatially resolved XRF, XANES, and EXAFS: Journal de Physique IV, v. 7, p. 767–771.

Juillot, F., ms, 1999, Localisation et spéciation de l'arsenic, du plomb, et du zinc dans des sites et sols contaminés. Comparaison avec un sol développé sur une anomalie géochimique naturelle en plomb: Ph.D. thesis, University of Paris 7.

Kemner, K. M., Hunter, D. B., Gall, E. J., Bertsch, P. M., Kirkland, J. P., and Elam, W. T., 1997, Molecular characterization of Cr phases in contaminated soils by Cr and Fe EXAFS: A tool for evaluating chemical remediation strategies: Journal de Physique IV, v. 7, p. 811–812.

Kemner, K. M., Yun, W., Cai, Z., Lai, B., Lee, H. R., Maser, J., Legnini, D. G., Rodrigues, W., Jastrow, J. D., Miller, R. M., and Pratt, S. T., 1999, Using zone plates for X-ray microimaging and microspectroscopy in environmental science: Journal of Synchrotron Radiation, v. 6, 639–641.

Kim, C. S., Rytuba, J. J., and Brown, G. E., 1999, Utility of EXAFS in characterization and speciation of mercury-bearing mine wastes: Journal of Synchrotron Radiation, v. 6, 648–650.

Krishnamurti, G. S. R., Huang, P. M., Vanrees, K. C. J., Kozak, L. M., and Rostad, H. P. W., 1995, Speciation of particulate-bound cadmium of soils and its bioavailability: Analyst, v. 120, p. 659–665.

Kuwahara, Y., 1999, Muscovite surface structure imaged by fluid contact mode AFM: Physics and Chemistry of Minerals, v. 26, p. 198–205.

Lake, D. L., Kirk, P. W. W., and Lester, J. N., 1984, Fractionation, characterization, and speciation of heavy metals in sewage sludge and sludge-amended soils: a review: Journal of Environmental Quality, v. 13, p. 175–183.

Lanson, B., Drits, V. A., Silvester, E. J., and Manceau, A., 2000, Structure of H-exchanged hexagonal birnessite and its mechanism of formation from Na-rich monoclinic buserite at low pH: New data from X-ray diffraction: American Mineralogist, in press.

Lee, J. H., and Guggenheim, S., 1981, Single crystal X-ray refinement of pyrophyllite-1Tc: American Mineralogist, v. 66, p. 350–357.

Lee, P. A., and Pendry, J. B., 1975, Theory of the extended x-ray absorption fine structure: Physical Review, v. B11, p. 2795–2811.

Liebau, F., 1985, Structural Chemistry of Silicates. Structure, Bonding, and Classification: Berlin, Springer-Verlag, 347 p.

MacDowell, A. A., Celestre, R., Chang, C. H., Franck, K., Howells, M. R., Locklin, S., Padmore, H. A., Patel, J. R., and Sandler, R., 1997, Progress towards sub-micron hard x-ray imaging using elliptically bent mirrors, *in* Takacs, P. Z., and Tonnessen, T.W., editors, Materials, Manufacturing and Measurement for Synchrotron Radiation Mirrors: Society of Photo-Optical Instrumentation Engineers (SPIE), v. 3152, p. 126–135.

MacDowell, A. A., Celestre, R., Chang, C. H., Lamble, G. M., Padmore, H. A., and Patel, J. R., 1998, Progress towards sub-micron hard x-ray imaging using elliptically bent mirrors: *in* McNulty, I., editor, X-ray microfocusing: Applications and Techniques, p. 137–144.

Manceau, A., Boisset, M. C., Sarret, G., Hazemann, J. L., Mench, M., Cambier, P., and Prost, R., 1996, Direct determination of lead speciation in contaminated soils by EXAFS spectroscopy: Environmental Science and Technology, v. 30, p. 1540–1552.

Manceau, A., Bonnin, D., Stone, W. E. E., and Sanz, J., 1990, Distribution of Fe in the octahedral sheet of trioctahedral micas by polarized EXAFS. Comparison with NMR results: Physics and Chemistry of Minerals, v. 17, p. 363–370.

Manceau, A., and Calas, G., 1986, Ni-bearing clay minerals. 2. X-ray absorption study of Ni-Mg distribution: Clay Minerals, v. 21, p. 341–360.

Manceau, A., Chateigner, D., and Gates, W. P., 1998, Polarized EXAFS, distance-valence least squares modeling (DVLS) and quantitative texture analysis approaches to the structural refinement of Garfield nontronite: Physics and Chemistry of Minerals, v. 25, p. 347–365.

Manceau, A., and Combes, J. M., 1988, Structure of Mn and Fe oxides and oxyhydroxides: a topological approach by EXAFS: Physics and Chemistry of Minerals, v. 15, p. 283–295.

Manceau, A., Drits, V. A., Lanson, B., Chateigner, D., Wu, J., Huo, D. F., Gates, W. P., and Stucki, J. W., 2000, Oxidation-reduction mechanism of iron in dioctahedral smectites. 2. Structural chemistry of reduced Garfield nontronite. American Mineralogist, v. 85, p. 153–172.

Manceau, A., Schlegel, M., Nagy, K. L., and Charlet, L., 1999, Evidence for the formation of trioctahedral clay upon sorption of Co^{2+} on quartz, Journal of Colloid and Interface Science, v. 220, p. 181–197.

Manceau, A., Lanson, B., Drits, V. A., Chateigner, D., Gates, W. P., Wu, J., Huo, D. F., and Stucki, J. W., 2000, Oxidation-reduction mechanism of iron in dioctahedral smectites. 1. Structural chemistry of oxidized nontronite references, American Mineralogist, v. 85, p. 133–152.

Manceau, A., Schlegel, M., Chateigner, D., Lanson, B., Bartoli, C., and Gates, W. P., 1999, Application of Polarized EXAFS to Fine-Grained Layered Minerals, in Schulze, D., Bertsch, P., and Stucki, J., editors, Synchrotron X-ray Methods in Clay Science: Clay Mineral Society of America, v. 9, p. 68–114.

McBride, M. B., 1994, Environmental chemistry of soils: New York, Oxford University Press, 406 p.

McGrath, D., 1996, Application of single and sequential extraction procedures to polluted and unpolluted soils: The Science of the Total Environment, v. 178, p. 37–44.

Mench, M., Vangronsveld, J., Didier, V., and Clijsters, H., 1994, Evaluation of metal mobility, plant availability and immobilization by chemical agents in a limed silty soil: Environmental Pollution, v. 86, p. 279–286.

Ministère de l'Environnement, 1996, Recensement 1996 des sites et sols pollués: Paris, Ministère de l'Aménagement du Territoire et de l'Environnement, 429 p.

Morin, G., Ostergren, J. D., Juillot, F., Ildefonse, P., Calas, G., and Brown, G. E., 1999, XAFS determination of the chemical form of lead in smelter-contaminated soils and mine tailings: Importance of adsorption processes: American Mineralogist, v. 84, p. 420–434.

Muller, F., Besson, G., Manceau, A., and Drits, V. A., 1997, Distribution of isomorphous cations within octahedral sheets in montmorillonite from Camp-Bertaux: Physics and Chemistry of Minerals, v. 24, p. 159–166.

Nakai, I., Numako, C., Hayakawa, S., and Tsuchiyama, A., 1998, Chemical speciation of geological samples by micro-XANES techniques: Journal of Trace Microprobe Technology, v. 16, p. 87–98.

Needleman, H. L., and Gatsonis, C. A., 1990, Low-level lead exposure and the IQ of children: a meta-analysis: JAMA, v. 263, p. 673–678.

Newville, M., Sutton, S., Rivers, M., and Eng, P., 1999, Micro-beam X-ray absorption and fluorescence spectroscopies at GSECARS: APS beamline 13ID: Journal of Synchrotron Radiation, 6, 353–355.

O'Day, P. A., Carroll, S. A., and Waychunas, G. A., 1998, Rock-water interactions controlling zinc, cadmium, and lead concentrations in surface waters and sediments, U.S. Tri-State Mining District. I. Molecular identification using X-ray absorption spectroscopy: Environmental Science and Technology, v. 32, p. 943–955.

Ostergren, J. D., Brown, G. E., Parks, G. A., and Tingle, T. N., 1999, Quantitative lead speciation in selected mine tailings from Leadville, CO: Environmental Science and Technology, p. 1627–1636.

Padmore, H. A., Ackerman, G., Celestre, R., Chang, C-H, Howells, M., Hussain, Z., Irick, S., Locklin, S., MacDowell, A. A., Patel, J. R., Rah, S. Y., Renner, T. R., and Franck, K., 1997, Sub-micron white-beam focusing using elliptically bent mirrors: Synchrotron Radiation News, v. 10, p. 18–26.

Pickering, W. F., 1981, Selective chemical extraction of soil components and bound metal species: CRC Critical Reviews in Analytical Chemistry, v. 12, p. 233–266.

Post, J. E., and Appleman, D. E., 1988, Chalcophanite, $ZnMn_3O_7{:}3H_2O$: New crystal-structure determination: American Mineralogist, v. 73, p. 1401–1404.

Quevauviller, P., Rauret, G., Muntau, H., Ure, A. M., Rubio, R., Lopezsanchez, J. F., Fiedler, H. D., and Griepink, B., 1994, Evaluation of a sequential extraction procedure for the determination of extractable trace metal contents in sediments: Fresenius Journal of Analytical Chemistry, v. 349, p. 808–814.

Raksasataya, M., Langdon, A. G., and Kim, N. D., 1996, Assessment of the extent of lead redistribution during sequential extraction by two different methods: Analytica Chimica Acta, v. 332, p. 1–14.

Rehr, J. J., Mustre de Leon, J., Zabinsky, S. I., and Albers, R. C., 1991, Theoretical X-ray Absorption Fine Structure Standards: Journal of the American Chemical Society, v. 113, p. 5135–5145.

Rimstidt, J. D., 1997, Quartz solubility at low temperatures: Geochimica et Cosmochimica Acta, v. 61, p. 2553–2558.

Rimstidt, J. D., and Barnes, H. L., 1980, The kinetics of silica-water reactions: Geochimica et Cosmochimica Acta, v. 44, p. 1683–1699.

Salomons, W., Förstner, U., and Mader, P., 1995, Heavy Metals. Problems and Solutions: Berlin, Springer-Verlag, 412 p.

Sarcia, C., and Talbot, A., 1984, Pollution des sols par les métaux lourds autour des usines Penarroya et de la C.R.A.M.: Orléans, BRGM Report, 30 p.

Schlegel, M., Manceau, A., Chateigner, D., and Charlet, L., 1999, Sorption of metal ions on clay minerals. I. Polarized EXAFS evidence for the adsorption of Co on the edges of hectorite particles: Journal of Colloid and Interface Science, v. 215, p. 140–158.

Sheppard, M. I., and Stephenson, M., 1997, Critical evaluation of selective extraction methods for soils and sediments, in Prost, R., editor, Contaminated soils: Paris, INRA. p. 69–97.

Silvester, E., Manceau, A., and Drits, V. A., 1997, The Structure of Synthetic Monoclinic Narich birnessite and Hexagonal Birnessite. Part 2. Results from Chemical Studies and EXAFS Spectroscopy: American Mineralogist, v. 82, p. 962–978.

Sobanska, S., ms, 1999, Étude de la spéciation du plomb et du zinc dans des poussières industrielles et dans un sol contaminé: Ph.D. thesis, University of Sciences and Technologies of Lille.

Sobanska, S., Ricq, N., Laboudigue, A., Guillermo, R., Brémard, C., Laureyns, J., Merlin, J. C., and Wignacourt, J. P., 1999, Microchemical investigations of dust by a lead smelter: Environmental Science and Technology, v. 33, p. 1334–1339.

Sposito, G., 1994, Chemical equilibria and kinetics in soils: New York, Oxford University Press, 268 p.

Stern, E. A., and Heald, S. M., 1983, Basic principles and applications of EXAFS, *in* Koch, E., editor, Handbook of Synchrotron Radiation: Amsterdam, New York, North-Holland, p. 955–1014.

Tardy, Y., and Duplay, J., 1992, A method of estimating the Gibbs free energy of formation of hydrated and dehydrated clay minerals: Geochimica et Cosmochimica Acta, v. 56, p. 3007–3029.

Tardy, Y., and Fritz, B., 1981, An ideal solid solution model for calculating solubilities of clay minerals: Clay Minerals, v. 16, p. 361–373.

Tardy, Y., and Garrels, R. M., 1976, Prediction of Gibbs energy of formation-I Relationships among gibbs energies of formation of hydroxides, oxides and aqueous ions: Geochimica et Cosmochimica Acta, v. 40, p. 1051–1056.

—— 1977, Prediction of Gibbs energy of formation of compounds from the elements-II. Monovalent and Divalent metal silicates: Geochimica et Cosmochimica Acta, v. 41, p. 87–92.

Teo, B. K., 1986, EXAFS: Basic Principles and Data Analysis: Inorganic Chemistry Concepts 9: Berlin, Springer-Verlag, 349 p.

Tessier, A., and Campbell, P. G. C., 1991, Comment on pitfalls of sequential extraction: Water Research, v. 25, p. 115–117.

Tessier, A., Campbell, P. G. C., and Bisson, L., 1979, Sequential extraction procedure for the speciation of particulate trace metals: Analytical Chemistry, v. 51, p. 844–851.

Thiry, M., and Van Oort, F., 1999, Les phases minérales majeures et mineures d'une friche industrielle de métallurgie des métaux non-ferreux: état d'altération, évolution géochimique et devenir des métaux polluants du site de Mortagne-du-Nord, in Les Cahiers des Clubs CRIN, editor, Spéciation des métaux dans le sol: Paris, Club CRIN, 296 p.

Tokunaga, T. K., Brown, G. E., Pickering, I. J., Sutton, S. R., and Bajt, S., 1997, Selenium redox reactions and transport between ponded waters and sediments: Environmental Science and Technology, v. 31, p. 1419–1425.

Vangronsveld, J., Van Assche, F., and Clijsters, H., 1995, Reclamation of a bare industrial area contaminated by non-ferrous metals: In situ metal immobilization and revegetation: Environmental Pollution, v. 87, p. 51–59.

Wadsley, A. D., 1955, The crystal structure of chalcophanite, $ZnMn_3O_7 \cdot 3H_2O$: Acta Crystallographica, v. 8, p. 1165–172.

Whalley, C., and Grant, A., 1994, Assessment of the phase selectivity of the European Community Bureau of Reference (BCR) sequential extraction procedure for metals in sediment: Analytical Chimica Acta, v. 291, p. 287–295.

Wickham, G. A., 1990, Zinc industry in the 1990's, *in* Mackey, T. S., and Prengaman, R. D., editors, Lead, Zinc'90, Proceeding of the World Symposium on Pb and Zn: Warrendale, TMS-AIME, p. 13–21.

Yun, W., Pratt, S. T., Miller, R. M., Cai, Z., Hunter, D. B., Jarstfer, A. G., Kemner, K. M., Lai, B., Lee, H. R., Legnini, D. G., Rodrigues, W., and Smith, C. I., 1998, X-ray imaging and microspectroscopy of plants and fungi: Journal of Synchrotron Radiation, v. 5, p. 1390–1395.